Ilona Bednarek

Relativistic Mean Field Models of Neutron Stars

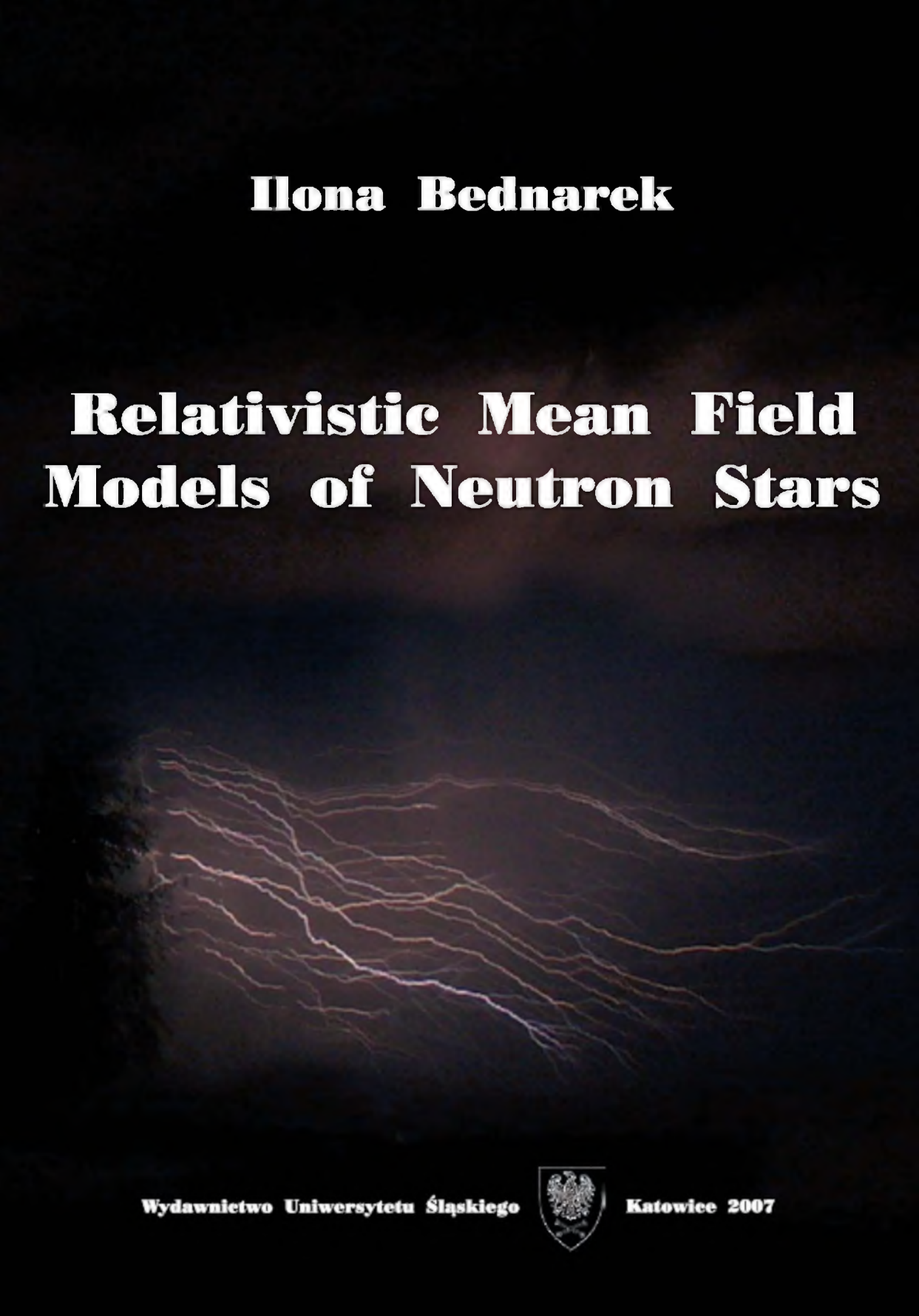

Wydawnictwo Uniwersytetu Śląskiego Katowice 2007

Relativistic Mean Field Models of Neutron Stars

PRACE
NAUKOWE

UNIWERSYTETU
ŚLĄSKIEGO
W KATOWICACH

NR 2538

Ilona Bednarek

Relativistic Mean Field Models of Neutron Stars

Wydawnictwo Uniwersytetu Śląskiego Katowice 2007

Redaktor serii: Fizyka Władysław Borgieł

Recenzenci Paweł Haensel
Krzysztof Pomorski

Publikacja jest dostępna także w wersji internetowej:
Śląska Biblioteka Cyfrowa
www.sbc.org.pl

Redaktor: Grażyna Wojdała

Zdjęcie na okładce ze zbiorów prywatnych
Aleksandry Sekuły

Projektant okładki: Agnieszka Szymala

ISSN 0208-6336
ISBN 978-83-226-1706-9

Wydawca
Wydawnictwo Uniwersytetu Śląskiego
ul. Bankowa 12B, 40-007 Katowice
www.wydawnictwo.us.edu.pl
e-mail: wydawus@us.edu.pl

Wydanie I. Nakład: 70 + 50 egz. Ark. druk. 12,25. Ark. wyd. 11,0. Podpisano do druku w lipcu 2007 r. Papier offset. kl. III, 90 g Cena 17 zł

Druk i oprawa: D&D Sp. z o. o., ul. Moniuszki 6, 44-100 Gliwice

Contents

Chapter 1

Introduction

The physical properties of matter under extreme conditions of temperature and density have received special attention during the past years and this is still one of the most complex problems of theoretical and experimental physics [1, 2, 3, 4, 5]. The state of matter under a given set of physical conditions can be described by a constitutive relation known as an equation of state (EOS). It provides a mathematical relation between state functions associated with matter and is a key factor in many essential aspects of stellar physics such as the ionization and excitation states, the onset of electron degeneracy or the temperature gradient [6, 7, 8].

The EOS together with nuclear reaction rates and the opacity determines the structure and evolution of a star. The longest phase of stellar evolution described by models of stars in thermal and hydrostatic equilibrium with central hydrogen burning are characterized by the EOS of a classical perfect gas. As a star evolves and its density increases, electrons which initially form a perfect, classical gas start to form a dense, degenerate quantum gas. The EOS of such a degenerate gas is an increasing function of density. The form of this function changes when the electron gas is considered in a non-relativistic or ultra-relativistic regime. In the case of a white dwarf, this is the pressure of a degenerate electron gas that supports the star [9].

Having obtained the EOS of degenerate electron gas and scaling it trivially with particle masses and statistical weight, the EOS adequate for the degenerate perfect gas of arbitrary fermions can be obtained. This is of special relevance for neutrons as they are the main component of a neutron star. In general, neutron star models are constructed at different levels of complexity starting with the most elementary, this

assumes that neutrons are the only component of neutron star matter. Realistic calculations of the properties of neutron stars are based upon the relativistic equation for hydrostatic equilibrium and an EOS for neutron star matter. Its computation is the main problem in the construction of a reliable model of a neutron star.

The aim of this dissertation is to analyze the properties of neutron star matter in high density and neutron-rich regimes and to study neutron star parameters, namely the masses and radii which are the most sensitive for the form of the EOS.

The description of a neutron star interior is modelled on the basis of the EOS of a dense nuclear system in a neutron-rich environment [9, 10]. Despite the fact that neutron star matter is directly affected by the nature of strong interactions, it is not possible to give its description on the basis of quantum chromodynamics (QCD) even though it is the fundamental theory of strong interactions. At the hadronic energy scale where the experimentally observed degrees of freedom are hadrons, the direct description of nuclei in terms of QCD becomes inadequate. Another alternative approach had to be formulated. In general the description of nuclear matter is based on different models which can be grouped into phenomenological and microscopic. Additionally each one of them can be either relativistic or non-relativistic.

In a microscopic approach the construction of the realistic model of nucleon-nucleon (NN) interaction can be inspired by the meson exchange theory of nuclear forces. The parameters within the model have to be adjusted to reproduce the experimental data for the deuteron properties and NN scattering phase shifts [11]. Defining the nuclear Hamiltonian is a starting point in the description of the nuclear matter. The next step requires solution of the many-body problem.

The basic approaches to this are of variational-type [12], [13] and of Brueckner-type. The solution of the nuclear many-body problem performed with the use of variational calculations for realistic NN interactions (for example for the Argonne v14 or Urbana v14 potentials) saturate at the density $\sim 2 \times \rho_0$, where ρ_0 denotes the saturation density [12], [13]. In order to obtain the correct description of nuclear matter properties, namely the saturation density, binding energy and compression modulus at the empirical values, a phenomenological three-nucleon interaction has to be introduced. Two-body forces, together with implemented three-body forces, help providing the correct saturation point of symmetric nuclear matter [14, 15]. The nuclear

matter EOS calculated with the use of the Brueckner–Hartree–Fock [16, 17] approximation with the employed realistic two-nucleon interactions (the Bonn and Paris potentials) also does not correctly reproduce nuclear matter properties. Thus there are attempts to consider the nuclear interaction problem in a relativistic formalism. The relativistic version of the Brueckner–Hartree–Fock approximation – the Dirac–Brueckner–Hartree–Fock approach [18, 19, 20, 21] is also based on realistic NN interactions. A qualitative description of the strong short-range NN force with large repulsive components compensated by attractive ones can be provided within the meson exchange model for the NN interaction. In its simplest version the meson exchange model involves only two types of mesons – the vector meson ω and the scalar meson σ. The nucleon self-energy involved in the Dirac equation is calculated with the use of the meson exchange model within a Hartree approximation.

The phenomenological model of the EOS can be calculated on the basis of the density dependent effective NN interactions. Calculations performed in Hartree–Fock [22] and Thomas–Fermi [23] approximations for the most popular phenomenological NN forces – the Skyrme forces, which contain parameters that have been established by adjusting nuclear matter and finite nuclei properties, yields very good results. Another phenomenological approach for the nuclear many-body problem is based on relativistic field theory. This relativistic approach to nuclear matter at the hadronic energy scale was developed by Walecka. The formulated theory known as quantum hadrodynamics (QHD) [24, 25, 26, 27, 28, 29, 30] gives a quantitative description of the nuclear many-body problem [25, 31]. In this model the force between nucleons is thought of as being mediated by the exchange of mesons. The original model (QHD-I) contains nucleons interacting through the exchange of simulating medium range attraction σ mesons and ω mesons responsible for the short range repulsion. The extension of this model (QHD-II) [32, 33, 34, 35] also includes the isovector meson ρ. Nonlinear terms of the scalar and vector fields were added in order to get the correct value of the compressibility of nuclear matter and the proper density dependence in vector self-energy.

Furnstahl, Serot and Tang [36, 37], using Lorentz-covariant effective quantum field theory and density functional theory (DFT) for hadrons, have constructed an effective Lagrangian consistent with the underlying symmetries of QCD. This Lagrangian includes nucleons, pions and

non-Goldstone bosons which provide the description of the medium and short range of the NN interaction and the nonvanishing expectation values of bilinear nucleon operators of the nucleon fields: $\bar{N}N$, $\bar{N}\gamma^{\mu}N$. Due to the nonlinear realization of the chiral symmetry, there is the possibility of introducing a light scalar, isoscalar, chiral singlet field with the Yukawa coupling to nucleons. This scalar field simulates the effect of pion exchange and describes the attractive NN interaction. Applying Georgi and Manohar's naive dimensional analysis and naturalness [38, 39, 40] the nonlinear chiral Lagrangian can be expanded in powers of the fields and their derivatives. The assignment of an index ν to each term which appears in the effective Lagrangian makes it possible to truncate this Lagrangian to terms with $\nu \leq 4$. Owing to a very high density of matter in neutron star interiors, extrapolation of nuclear models for such dense systems is required for its description. Contrary to satisfactory results obtained for finite nuclei at saturation density the predictions made by nuclear models for much more dense matter differ considerably from each other. Calculations performed on the basis of Dirac–Brueckner–Hartree–Fock model lead to a rather soft EOS. Moreover, recent experimental data has suggested a similar conclusion. However, the standard nonlinear models of quantum hydrodynamics give EOS which is too stiff for increasing density.

The TM1 parameter set constructed by Sugahara and Toki [31] includes the quartic vector self-interaction term gives satisfactory results for finite nuclei, neutron star matter and supernova models. It improves the results of the NL1 [28] and NL3 [41] nonlinear models. The parameter set G2 which stems from effective field theory is the original parameter set of Furnstahl, Serot and Tang. It gives the EOS where high density behavior resembles the DBHF result [42, 43]. Del Estal et al. [44, 45] have constructed a parameter set which at saturation gives the same nuclear matter properties as the TM1 parameter set. However, the behavior of the EOS calculated for these parameters, due to the presence of additional nonlinear couplings, at densities above the saturation density is similar to the one calculated for the G2 parameter set. Usage of the TM1* and G2 parameter sets for the description of asymmetric neutron star matter is intended to make this description more detailed and complete. For comparison similar calculations have been done for neutron star matter with TM1 parameterization supplemented by the inclusion of nonlinear couplings [46, 47]. The analysis has been carried out by adding the nonlinear mixed isoscalar-isovector

meson interaction terms to the TM1 parameter set. This enlargement, due to the coupling to the isovector meson field influences the density dependence of the symmetry energy and affects the chemical composition of neutron stars changing the proton and lepton profiles in the case of a cold neutron star and additionally the cooling rate and neutrino flux of a proto-neutron star.

As stated above the description of a neutron star requires taking into consideration not only its interior region but also its remaining parts, namely the inner and outer crust and surface layers. The composite EOS, which allows us to calculate neutron star structure for the entire density span, can be constructed by adding the Baym–Pethick–Sutherland [48] EOS, for very low densities $n < 0.001\,\mathrm{fm}^{-3}$, and for the Machleidt–Holinde–Elster and Bonn [49] and Negele–Vautherin [50] forms of the EOS densities within the range of $0.001\,\mathrm{fm}^{-3} < n < 0.08\,\mathrm{fm}^{-3}$.

Normal nuclei bound by strong forces are in states, which can be defined as the equilibrium state of isospin symmetric nuclear matter with minimum energy per nucleon. The condition of an equal number of protons and neutrons is fulfilled in the case of infinite symmetric nuclear matter. In heavy nuclei the overall neutron excess defined as $I = (N - Z)/(N + Z)$ takes the value up to about 0.24 [51]. This limit can be exceeded in rare-isotope accelerator experiments. Neutron star matter realizes the condition of extreme asymmetry which can approach the value of 0.95. It is gravity that binds neutron stars in this case. Highly asymmetric neutron star matter is not bound by the strong interaction.

The high asymmetry of neutron star matter implies the presence of leptons. The indispensable conditions of charge neutrality and chemical equilibrium constrain the neutron star matter EOS determining the main differences between the neutron star matter EOS and the one relevant to infinite symmetric nuclear matter.

In the interior of neutron stars the density of matter could exceed normal nuclear matter density by a factor of few. In such high density regimes nucleon Fermi energies exceed the value of hyperon masses and thus new hadronic degrees of freedom are expected to emerge. The higher the density the more various hadronic species are expected to populate. The presence of hyperons adds another very important aspect to the problem of the nuclear EOS. The strange nuclear matter created during the heavy ion collision experiments can be observed over

such a short period of time that the weak decays of strange baryons can be neglected and the system is characterized by zero net strangeness. In contrast, strangeness is not conserved in neutron star matter. This has very important consequences for its EOS and also has a direct effect on neutron star parameters. The onset of hyperon formation depends on the hyperon-nucleon and hyperon-hyperon interactions. Hyperons can be formed both in leptonic and baryonic processes. Several relevant strong interaction processes proceed and establish the hadron population in neutron star matter.

In this dissertation all calculations have been done with the use of relativistic mean-field approximation. A very important aspect of neutron star observations is connected with the fact that measurements of neutron star parameters can provide constraints on the form of the EOS and thereby improves our understanding of matter at extreme pressure and density.

This dissertation is organized in the following way: it starts from the chapters which present the stellar structure equations and thermodynamic properties of stellar matter. In chapter 4 the ground-state nuclear matter properties are described. This has been done on the basis of a nuclear matter EOS which is specified by the following parameters: the binding energy, density at saturation, incompressibility, symmetry energy coefficient, the slope and curvature of the symmetry energy. In chapter 6 the relativistic mean field models, which are based on quantum hadrodynamics and which have been successfully applied to the description of nuclear matter properties are presented. Chapter 7 describes in outline the main findings of the Furnstahlm, Serot and Tang model known as effective relativistic mean field theory which includes new, general couplings. In this chapter the extension of the considered models has been examined by including strangeness. The nuclear matter properties have been calculated for the chosen parameter sets, namely TM1, G2 and TM1*. In the case when the additional nonlinear couplings and δ meson were taken into account the parameters in the isovector channel have been determined. Special efforts have been made to produce an optimal set of parameters for the strange sector of each model. Chapter 8 presents the results of the numerical analysis of nuclear matter properties for the selected parameter sets. Subsequent sections of this chapter give the results for infinite symmetric nuclear matter, symmetric nuclear matter with nonzero strangeness, asymmetric nuclear matter and asymmetric strangeness-rich matter.

Special attention has been devoted to neutron star matter which exemplifies infinite, asymmetric nuclear matter in β-equilibrium. After discussing the equilibrium conditions for neutron star matter in chapter 9, the EOS has been constructed for the selected parameterizations. On obtaining the EOS the composition and structure of a neutron star have been analyzed. The obtained mass-radius relations are also constructed for neutron star matter with hyperons and compared with the mass-radius relation for non-strange matter. This has been done in chapter 10. The analysis has been performed for the ordinary TM1 parameter set enlarged by the additional nonlinear meson interaction terms and for the parameter sets of the models which have been constructed on the basis of the relativistic effective field theory. The TM1 parameter set gives larger neutron star masses than the TM1* and G2. However, the key difference between the TM1 and TM1* and G2 mass-radius diagrams lies in the results obtained for the strong hyperon-hyperon interaction. In this case for TM1* and G2 parameter sets besides the ordinary stable neutron star branch there exists the additional stable branch of solutions which are characterized by a similar value of masses but with significantly reduced radii. Chapter 11 presents the astrophysical constraints on the EOS. In chapter 12 proto-neutron star models calculated on the basis of the presented parameter sets have been analyzed. Finally the findings of all performed calculations and analysis have been summarized.

Chapter 2

Stellar structure equations

The fundamental equations of stellar structure constitute a coupled system of differential equations. These equations are based on the assumptions of spherical symmetry and hydrostatic equilibrium under Newtonian gravity and they are given by [6], [7], [8], [52]

$$\frac{dP}{dr} = -\rho\frac{Gm}{r^2}, \tag{2.1}$$

$$\frac{dm}{dr} = 4\pi r^2\rho, \tag{2.2}$$

$$\frac{dL}{dr} = 4\pi\rho, r^2\left(\varepsilon_n - \varepsilon_\nu - \frac{\partial u}{\partial t} + \frac{P}{\rho^2}\frac{\partial\rho}{\partial t}\right), \tag{2.3}$$

$$L = L_{rad} = -\frac{16\pi acT^3r^2}{3\kappa\rho}\frac{dT}{dr}, \tag{2.4}$$

$$\nabla_{rad} < \nabla_a + \nabla_\mu, \tag{2.5}$$

$$\frac{dT}{dr} = \left(\frac{\partial T}{\partial P}\right)_{S,\mu}\frac{dP}{dr}, \tag{2.6}$$

$$L = 4\pi r^2F_{conv} + L_{rad}, \tag{2.7}$$

$$\frac{dT}{dr} = \left(\frac{\partial T}{\partial P}\right)_{S,\mu}\frac{dP}{dr}. \tag{2.8}$$

Equation (2.1) is the hydrostatic equilibrium equation and (2.2) is the conservation of mass, with m being the mass inside radius r, P is the pressure and ρ denotes the matter density. Equation (2.3) represents the energy equation where L is the power generated within a sphere of radius r, whereas ε_n and ε_ν are the rates of nuclear energy

release and neutrino losses, respectively. The last two terms in this equation containing the time derivatives represent the gravitational energy source, u is the specific energy. The case of static stellar structure can be recovered by setting the time derivatives in equation (2.3) equal zero.

The remaining equations describe the energy transport in stellar matter. Assuming that radiative diffusion is the dominant heat transfer mechanism the total outward power flow is given by equation (2.4), where $L \equiv L(r)$ is the rate at which energy flows outwards through a spherical surface of radius r within the star, κ denotes the opacity of stellar material, a is the radiation energy density constant and c is the velocity of light. The inequality (2.5) represents the Ledoux criterion for convective stability, ∇_{rad} denotes the temperature gradient for the case that the energy is transported by radiation, ∇_μ represents the change of the molecular weight μ_{mol} due to the change of chemical composition. In the case of homogenous medium setting $\nabla_\mu = 0$ a special case of the condition (2.5) can be obtained which is known as the Schwarzschild criterion.

When the dynamical stability criterion is not satisfied the radiative diffusion is not the dominant mechanism for the heat transfer and the convection has to be included. The critical temperature gradient for the onset of convection is giving by equation (2.6). The convection heat transfer equation can be written as (2.7) where F_{conv} represents the convective flux for a mixture of a perfect classical, totally ionized gas with radiation. The logarithmic gradients in inequality (2.5) are given by [6], [7], [8], [52]

$$\nabla_a = \left(\frac{\partial \ln T}{\partial \ln P}\right)_S = \frac{2(4-3\beta_g)}{32-24\beta_g-3\beta_g^2}, \tag{2.9}$$

$$\nabla_\mu = \left(\frac{\partial \ln T}{\partial \ln \mu_{mol}}\right)_{P,S} \frac{d\ln \mu_{mol}}{d\ln P} = \frac{\beta_g}{1-3\beta_g}\frac{d\ln \mu_{mol}}{d\ln P}, \tag{2.10}$$

$$\nabla_{rad} = \frac{d\ln T}{d\ln P} = \frac{\kappa L_r}{16\pi cGm(1-\beta_g)}. \tag{2.11}$$

In these equations $\beta_g = P_g/P$ is the ratio of the gas pressure to the total pressure and the equation (2.10) includes changes in the molecular weight μ_{mol}.

Numerical solutions of the stellar structure equations are indispensable for obtaining a model of each type of star and for constructing

Table 2.1: The proton-proton chains, Q (MeV) denotes the energy released by the reaction

ppI		**ppII**	
Reaction	Q	Reaction	Q
$^1\mathrm{H} + {}^1\mathrm{H} \rightarrow {}^2\mathrm{H} + \mathrm{e}^+ + \nu$	1.442	$^3\mathrm{He} + {}^4\mathrm{He} \rightarrow {}^7\mathrm{Be} + \gamma$	1.586
$^2\mathrm{H} + {}^1\mathrm{H} \rightarrow {}^3\mathrm{He} + \gamma$	5.493	$^7\mathrm{Be} + \mathrm{e}^- \rightarrow {}^7\mathrm{Li} + \nu$	0.861
$^3\mathrm{He} + {}^3\mathrm{He} \rightarrow {}^4\mathrm{He} + 2\,{}^1\mathrm{H}$	12.859	$^7\mathrm{Li} + {}^1\mathrm{H} \rightarrow {}^4\mathrm{He} + {}^4\mathrm{He}$	17.347
ppIII			
Reaction	Q	Reaction	Q
$^7\mathrm{Be} + {}^1\mathrm{H} \rightarrow {}^8\mathrm{B} + \gamma$	0.135	$^8\mathrm{B} \rightarrow 2\,{}^4\mathrm{He} + \mathrm{e}^+ + \nu$	18.074

evolutionary tracks on the Hertzsprung–Russel diagram for different stellar types. There are several, distinctive stellar evolutionary stages. The longest phase in the star's existence is the state where hydrogen converts into helium, and the giant and supergiant phases corresponding to evolved stars with hot, dense helium or carbon core surrounded by extended, hydrogen rich envelope. White dwarfs and neutron stars are stars with completed evolution and cooling due to radiation.

Stars being in thermal and hydrostatic equilibrium with central hydrogen burning represent the longest phase of stellar evolution. On the Hertzsprung–Russel diagram they are located on a particular broad band known as the main sequence. Models of stars of homogenous composition in which hydrogen burning is initiated define the very beginning of this phase and represent the zero-age main sequence (ZAMS). Hydrogen burning can proceed by two distinct types of reactions. Main sequence stars with masses comparable with the solar mass fuse hydrogen to helium via the proton-proton (pp) chains [6] which are shown in Table 2.1.

The pp chains account for hydrogen burning in main sequence stars with masses of the order of 1 $\mathrm{M}_\odot$. For more massive main sequence stars hydrogen burning predominantly proceeds via the carbon-nitrogen cycle. For sufficiently high temperature, in the presence of $^{12}\mathrm{C}$ and heavier elements hydrogen burning takes place through vari-

ous chains of reactions in which the heavy elements serve as catalysts. The lowest temperature cycle CN proceeds in the following form [6, 7]:

$$\begin{aligned} {}^{12}\mathrm{C} + \mathrm{p} &\rightarrow {}^{13}\mathrm{N} + \gamma, \\ {}^{13}\mathrm{N} &\rightarrow {}^{13}\mathrm{C} + \mathrm{e}^{+} + \nu, \\ {}^{13}\mathrm{C} + \mathrm{p} &\rightarrow {}^{14}\mathrm{N} + \gamma, \\ {}^{14}\mathrm{C} + \mathrm{p} &\rightarrow {}^{15}\mathrm{O} + \gamma, \\ {}^{15}\mathrm{O} &\rightarrow {}^{15}\mathrm{N} + \mathrm{e}^{+} + \nu, \\ {}^{15}\mathrm{N} + \mathrm{p} &\rightarrow {}^{12}\mathrm{C} + {}^{4}\mathrm{He}. \end{aligned} \tag{2.12}$$

The high Coulomb barriers involved in these reactions imply the energy production rate which increases very rapidly with temperature. The pp chains dominate at low temperatures $\mathrm{T} < 15 \times 10^{6}$ K.

Following hydrogen depletion in the core of a star, the star contracts and its temperature increases. The star develops isothermal helium core surrounded by a hydrogen-rich envelope. Depending on the stellar masses their post-main sequence evolution proceeds in a qualitatively different way. For a given temperature a limiting value of mass have been estimated. For stars more massive then $2.25\,\mathrm{M}_{\odot}$ [53] central helium burning sets in directly after hydrogen depletion. Stars with sufficiently small masses have isothermal helium cores partially supported by degeneracy pressure with masses less than the ignition mass for helium burning. In this case hydrogen burning starts in the surrounding shell. More massive stars proceed directly to a stage of core helium burning and shell hydrogen burning. The contraction of the core is accompanied by an expansion of the hydrogen-rich envelope outside the shell source. The star is in the red-giant region of the Hertzsprung–Russel diagram.

Table 2.2 presents in outline main thermonuclear burning stages in stars. Stages after helium burning are dominated by neutrino cooling, not by the photon diffusion [6].

The helium burning phase consists of two competing processes namely the carbon producing triple-alpha process:

$$\begin{aligned} {}^{4}\mathrm{He} + {}^{4}\mathrm{He} &\rightarrow {}^{8}\mathrm{Be}, \\ {}^{4}\mathrm{He} + {}^{8}\mathrm{Be} &\rightarrow {}^{12}\mathrm{C}^{*}, \\ {}^{12}\mathrm{C}^{*} &\rightarrow {}^{12}\mathrm{C} + (2\gamma \text{ or } (\mathrm{e}^{+} + \mathrm{e}^{-})), \end{aligned} \tag{2.13}$$

and the carbon-consuming oxygen production process

$$ {}^{4}\mathrm{He} + {}^{12}\mathrm{C} \rightarrow {}^{16}\mathrm{O} + \gamma. \tag{2.14}$$

Table 2.2: Thermonuclear burning stages, q is the energy released upon consumption of a unit mass of fuel by the process in question (Taken from [6])

Fuel	T/10^9 (K)	Ashes	q(erg/g)	Cooling
^{1}H	0.02	^{4}He,^{14}N	$(5 \sim 8)\times10^{18}$	photons
^{4}He	0.2	^{12}C,^{16}O,^{22}Ne	7×10^{17}	photons
^{12}C	0.8	^{20}Ne,^{24}Mg,^{16}O ^{23}Na, ^{25,26}Mg	5×10^{17}	neutrinos neutrinos
^{20}Ne	1.5	^{16}O,^{24}Mg,^{28}Si	1.1×10^{17}	neutrinos
^{16}O	2	^{28}Si, ^{32}S, ...	5×10^{17}	neutrinos
^{28}Si	3.5	^{56}Ni, A $\approx$ 56nuclei	$(0 \sim 3) \times 10^{17}$	neutrinos
^{56}Ni	$6 \sim 10$	n,^{4}He, ^{1}H	-8×10^{18}	neutrinos
A $\approx$ 56 nuclei	depends on ρ	photodisintegration and neutronization		

The net effect of sequence (2.13) is:

$$^4\mathrm{He} + {}^4\mathrm{He} + {}^4\mathrm{He} \rightarrow {}^{12}\mathrm{C}\ (Q_{3\alpha} = +7.274\,\mathrm{MeV}). \tag{2.15}$$

The reaction $^{12}\mathrm{C}\,(\alpha,\gamma)^{16}\mathrm{O}$ is considered as very important reaction in nuclear astrophysics [54]. This process determines the abundance of ^{12}C and ^{16}O in stars and through this has profound consequences for the stellar evolution from the helium burning phase to the late explosive phases. In the case of massive stars the $^{12}\mathrm{C}\,(\alpha,\gamma)^{16}\mathrm{O}$ reaction affects the production of heavier elements (up to the iron group). It also influences the composition of CO white dwarfs [55] whose progenitors are intermediate and low mass stars. The $^{12}\mathrm{C}/^{16}\mathrm{O}$ ratio is determined by two factors, the triple-alpha rate which for temperature T $\sim 10^8$ K is known with a precision of about 10% and α capture on ^{12}C [6]. However, there is a lack of adequate precision in the determination of the $^{12}\mathrm{C}\,(\alpha,\gamma)^{16}\mathrm{O}$ rate for construction of reliable stellar models. The experimental efforts carried out for the determination of the $^{12}\mathrm{C}\,(\alpha,\gamma)^{16}\mathrm{O}$ rate still require improvements. Kunz et al. in their

paper [56] presented a new astrophysical reaction rate of this process for temperatures of T$=$ $(0.04 - 10) \times 10^9$ K.

Further stellar evolution depends on the mass of the star. In the more massive stars there is a sequence of nuclear burning stages as the temperature and density at the center of the star progressively increase. The advance burning stages involving heavy nuclei proceed through the following processes [7, 8]:

- At the temperature T$\sim (5 - 10) \times 10^8$ K the reactions of carbon burning set in

$$^{12}\mathrm{C} + {}^{12}\mathrm{C} \rightarrow {}^{20}\mathrm{Ne} + {}^{4}\mathrm{He}, \tag{2.16}$$

$$^{12}\mathrm{C} + {}^{12}\mathrm{C} \rightarrow {}^{23}\mathrm{Na} + \mathrm{p}, \tag{2.17}$$

$$^{12}\mathrm{C} + {}^{12}\mathrm{C} \rightarrow {}^{23}\mathrm{Mg} + \mathrm{n}. \tag{2.18}$$

  The end products are mainly neon, sodium and magnesium.

- For the temperature T $\sim 10^9$ K the process of neon photodisintegration occurs

$$\gamma + {}^{20}\mathrm{Ne} \rightarrow {}^{16}\mathrm{O} + {}^{4}\mathrm{He}. \tag{2.19}$$

  The ^{4}He nuclei react with the ^{20}Ne nuclei and form ^{24}Mg

$$^{4}\mathrm{He} + {}^{20}\mathrm{Ne} \rightarrow {}^{24}\mathrm{Mg} + \gamma. \tag{2.20}$$

- Oxygen burning occurs when the temperature approaches $2 \sim 10^9$ K

$$^{16}\mathrm{O} + {}^{16}\mathrm{O} \rightarrow {}^{28}\mathrm{Si} + {}^{4}\mathrm{He}. \tag{2.21}$$

  The reactions of photodisintegration are very important in oxygen burning and later phases of stellar evolution. The released α particles in the photodisintegration of ^{28}Si

$$\gamma + {}^{28}\mathrm{Si} \rightarrow {}^{24}\mathrm{Mg} + {}^{4}\mathrm{He} \tag{2.22}$$

  lead to a sequence of reactions which produces sulphur, argon, calcium, etc.

- When the oxygen burning ceases at temperature T$> 3 \times 10^9$ K silicon burning occurs through a series of reactions that produce nuclei near the iron peak.

The transition from one evolutionary stellar model to another is connected with the change in the chemical composition of the star. This fact makes it necessary to have differential equations which have to be added to equations (2.1 – 2.8). For example equations describing the processes which take place during the phases of hydrogen, helium and carbon burning have the form [7, 8]

$$\frac{\partial X_H}{\partial t} = -4m_p \left(\frac{\epsilon_{CNO}}{Q_{CNO}} + \frac{\epsilon_{pp}}{Q_{pp}} \right), \tag{2.23}$$

$$\frac{\partial X_\alpha}{\partial t} = 4m_p \left(\frac{\epsilon_{CNO}}{Q_{CNO}} + \frac{\epsilon_{pp}}{Q_{pp}} \right) - \frac{3m_\alpha \epsilon_{3\alpha}}{Q_{3\alpha}} - \frac{m_\alpha \epsilon_{^{12}C\alpha}}{Q_{^{12}C\alpha}}, \tag{2.24}$$

$$\frac{\partial X_{^{12}C}}{\partial t} = \frac{3m_\alpha \epsilon_{3\alpha}}{Q_{3\alpha}} - \frac{m_{^{12}C} \epsilon_{^{12}C\alpha}}{Q_{^{12}C\alpha}}, \tag{2.25}$$

$$\epsilon_n = \epsilon_{pp} + \epsilon_{3\alpha} + \epsilon_{^{12}C\alpha}. \tag{2.26}$$

In the above equations X_i, where i = H, α, ^{12}C, denotes the mass fraction of the element with atomic number i, $\epsilon_{pp}, \epsilon_{3\alpha}, \epsilon_{CNO}$ and $\epsilon_{^{12}C}$ are the rates of energy release and $Q_{pp}, Q_{3\alpha}, Q_{CNO}$ and $Q_{^{12}C}$ are the released energies per reaction.

The determination of the static structure of a star can be obtained if the above set of differential equations is supplemented by the EOS, the function that describes the opacity of stellar material and the energy generation rate. The calculations also require the specification of boundary conditions.

The strong gravitational field of a neutron star is described by the Einstein field equations [2], [9]

$$R_{\mu\nu} - \frac{1}{2} g_{\mu\nu} R = \frac{8\pi G}{c^4} T_{\mu\nu}, \tag{2.27}$$

where $R_{\mu\nu}$ is the Ricci tensor, $g_{\mu\nu}$ is the metric tensor, R is the Ricci scalar, $T_{\mu\nu}$ is the energy momentum tensor given by

$$T_{\mu\nu} = -P g_{\mu\nu} + (P + \rho) u_\mu u_\nu, \tag{2.28}$$

where ρ denotes the matter density and P – pressure, u_μ is the local fluid four-velocity, which in the case of a static star yields

$$u_\mu = 0 \text{ for } \mu \neq 0, \; u_0 = \frac{1}{\sqrt{g_{00}}}. \tag{2.29}$$

For a static mass distribution $T_0^0 = \rho c^2$, and $T_1^1, T_2^2, T_3^3 = -P$. The gravitational field outside a spherically symmetric mass distribution has a spherical symmetry, for such fields the components of the metric tensor are functions of the radial coordinate r and time t. The solution of the field equations (2.27) needs the specification of the line element ds which in spherical coordinates has the form

$$ds^2 = g_{\mu\nu}dx^\mu dx^\nu = e^\nu c^2 dt^2 - e^\lambda dr^2 - r^2(d\vartheta^2 + sin^2\vartheta d\varphi^2). \quad (2.30)$$

Under the assumption of spherical symmetry and in the static limit equations (2.27) can be written as

$$e^{-\lambda}\left(\frac{\lambda'}{r} - \frac{1}{r^2}\right) + \frac{1}{r^2} = \frac{8\pi G}{c^2}\rho, \quad (2.31)$$

$$e^{-\lambda}\left(\frac{\nu'}{r} + \frac{1}{r^2}\right) - \frac{1}{r^2} = \frac{8\pi G}{c^4}P, \quad (2.32)$$

$$\frac{1}{2}e^{-\lambda}\left(\nu'' + \frac{\nu'^2}{2} + \frac{\nu' - \lambda'}{r} - \frac{\nu'\lambda'}{2}\right) - \frac{1}{r^2} = \frac{8\pi G}{c^4}P, \quad (2.33)$$

where primes denote radial derivatives.

Having obtained the energy-momentum tensor, which specifies the EOS, the differential equations for the structure of a static, spherically symmetric, relativistic star are given by

$$m(r) = \int_0^r 4\pi r^2 \rho(r) dr, \quad (2.34)$$

$$\frac{dP}{dr} = -\frac{Gm}{r^2}\rho\left(1 + \frac{P}{\rho c^2}\right)\left(1 + \frac{4\pi r^3 P}{mc^2}\right)\left(1 - \frac{2Gm}{rc^2}\right)^{-1}. \quad (2.35)$$

The first equation (2.34) is the mass equation whereas the second (2.35) is the Tolman–Oppenheimer–Volkoff equation [52], [57], [58].

Chapter 3

Thermodynamic properties of stellar matter

The macroscopic thermodynamic properties of gas can be specified by its temperature T, its pressure P and its chemical potential μ. When thermodynamic equilibrium is established these parameters (T, P and μ), which are related by the EOS, determine the equilibrium distribution of particles in the quantum state. The particle number density, internal energy density and pressure can be calculated by integrating over the momentum space [8], [59], [60]:

$$n = g_s \frac{4\pi}{h^3} \int_0^\infty f(p) p^2 dp, \tag{3.1}$$

$$u = g_s \frac{4\pi}{h^3} \int_0^\infty f(p) \varepsilon(p) p^2 dp, \tag{3.2}$$

$$P = g_s \frac{4\pi}{h^3} \int_0^\infty \left(\frac{1}{3} v(p) p \right) f(p) p^2 dp, \tag{3.3}$$

with

$$v(p) = \frac{pc^2}{\sqrt{p^2c^2 + m^2c^4}}. \tag{3.4}$$

In these integrals h is Planck constant, g_s is the statistical weight of a particle whereas $\varepsilon(p) = \sqrt{p^2c^2 + m^2c^4}$ is its total energy. The distribution function $f(p)$ has the form

$$f(p) = \frac{1}{1 \pm e^{(\varepsilon(p) - \mu)/k_B T}}. \tag{3.5}$$

The upper sign is for Fermi–Dirac and the lower for Bose–Einstein

statistics. The factor $v(p)p/3$ in the pressure integral is the net momentum flux through a plane for a perfect gas. The entropy can be calculated from the expression

$$S = \frac{V}{T}\int_0^\infty \left(\epsilon(p) - u + \frac{v(p)p}{3}\right)\frac{dn}{dp}dp. \tag{3.6}$$

3.1 Photon gas

Photons also provide a source of pressure in stellar interiors. In this case a gas of zero mass bosons is considered. The number of photons is not conserved (the chemical potential equals zero). Taking these assumptions into account ($m = 0$, $\mu = 0$ and $\varepsilon = pc$), using the dimensionless integration variable $x = pc/k_BT$ and taking $g_s = 2$ (there are two linearly independent states of polarization for electromagnetic waves), the integrals (3.1), (3.2), (3.3) and (3.6), for Bose–Einstein statistics, can be expressed in the following form

$$n = 8\pi\left(\frac{k_BT}{hc}\right)^3\int_0^\infty \frac{x^2dx}{e^x - 1}, \tag{3.7}$$

$$P = \frac{u}{3} = \frac{ST}{4V} = \frac{8\pi}{3}\left(\frac{k_BT}{hc}\right)^3 k_BT\int_0^\infty \frac{x^3dx}{e^x - 1}. \tag{3.8}$$

The calculations give the results for the pressure, energy density and entropy:

$$P = a\frac{T^4}{3}, \tag{3.9}$$

$$u = aT^4, \tag{3.10}$$

$$S = 4aV\frac{T^3}{3}, \tag{3.11}$$

where $a = 8\pi^5k_B^4/15(hc)^3$ is the radiation energy density constant.

3.2 Fermion gas

The definitions of particle number density, internal energy density and pressure of fermion gas show that these quantities are functions of k_BT, μ and mc^2 energies. Thus there are four limiting regimes for the functions which have to be considered. The relativistic limit occurs if the

conditions $k_BT/mc^2 \gg 1$ and $\mu/mc^2 \gg 1$ are satisfied. Whereas the limit of large mc^2 ($k_BT/mc^2 \ll 1$ and $\mu/mc^2 \ll 1$) corresponds to the non-relativistic case [6]. Quantum effects (degenerate gas) dominate for high density and low temperature and the non-degenerate limit occurs if $\exp\left((\varepsilon(p) - \mu)/k_BT\right) \gg 1$. Introducing dimensionless variables (subscript f denotes fermions):

$$x = \frac{pc}{k_BT}, \qquad \alpha = \frac{m_f c^2}{k_BT}, \qquad \beta = \frac{\mu_f}{k_BT}, \tag{3.12}$$

equations (3.1), (3.2), (3.3) and (3.6) can be written as follows [8]:

$$n_f = 4\pi g_s \left(\frac{k_BT}{ch}\right)^3 I_{n^-}, \tag{3.13}$$

$$u_f = 4\pi g_s \left(\frac{k_BT}{ch}\right)^3 k_BT I_{E^-}, \tag{3.14}$$

$$P_f = \frac{4\pi g_s}{3} \left(\frac{k_BT}{ch}\right)^3 k_BT I_{P^-}, \tag{3.15}$$

$$S_f = 4\pi g_s k_B \left(\frac{k_BT}{ch}\right)^3 (I_{E^-} - \beta I_{n^-} + \frac{1}{3} I_{P^-}), \tag{3.16}$$

where

$$I_{n^-} = \int_0^\infty \frac{x^2 dx}{1 + exp(\sqrt{x^2 + \alpha^2} - \beta)}, \tag{3.17}$$

$$I_{E^-} = \int_0^\infty \frac{\sqrt{x^2 + \alpha^2} x^2 dx}{1 + exp(\sqrt{x^2 + \alpha^2} - \beta)}, \tag{3.18}$$

$$I_{P^-} = \int_0^\infty \frac{x^4 dx}{\sqrt{x^2 + \alpha^2}[1 + exp(\sqrt{x^2 + \alpha^2} - \beta)]}. \tag{3.19}$$

In thermodynamic equilibrium, for sufficiently high temperatures antiparticles also must be included. This condition is satisfied if $k_BT \geq 0.1\, m_f c^2$. Thermodynamic functions for antiparticles can be calculated with the aid of equations (3.13), (3.14), (3.15) and (3.16) but in the integrals (3.17), (3.18) and (3.19) β should be substituted with $-\beta$.

3.2.1 Completely degenerate fermion gas

In order to calculate the number density, energy density and pressure of sufficiently dense fermion gas quantum effects have to be included. In the case of a cold fermion gas, fermions are in a quantum state with the lowest possible energy. Their total number density is related to the maximum momentum (the Fermi momentum p_F) by the relation

$$n_f = g_s \frac{4\pi}{3h^3} p_F^3. \tag{3.20}$$

The energy of the most energetic fermions in a cold degenerate gas is called the Fermi energy. Using the zero temperature limit of the distribution function $f(p)$ for which $f(p) = 1$ for $p \leq p_F$ and $f(p) = 0$ for $p > p_F$ the pressure and internal energy density integrals are given by

$$P_f = g_s \frac{4\pi}{3h^3} \int_0^{p_F} \frac{p^4 dp}{\sqrt{p^2c^2 + m_f^2 c^4}} = g_s \frac{m_f^4 c^5 \pi}{3h^3} f(\tilde{y}), \tag{3.21}$$

$$u_f = g_s \frac{4\pi}{h^3} \int_0^{p_F} \sqrt{p^2c^2 + m_f^2 c^4} p^2 dp = g_s \frac{m_f^4 c^5 \pi}{6h^3} g(\tilde{y}), \tag{3.22}$$

where the functions $f(\tilde{y})$ and $g(\tilde{y})$ are defined for the new variable $\tilde{y} = p_F/m_f c$ which measures the importance of relativistic effects for fermions with the highest momentum:

$$f(\tilde{y}) = \tilde{y}(2\tilde{y}^2 - 3)\sqrt{\tilde{y}^2 + 1} + 3\sinh^{-1}\tilde{y}, \tag{3.23}$$

$$g(\tilde{y}) = 3\tilde{y}(2\tilde{y}^2 + 1)\sqrt{\tilde{y}^2 + 1} - 3\sinh^{-1}\tilde{y}, \tag{3.24}$$

and

$$g(\tilde{y}) + f(\tilde{y}) = 8\tilde{y}^3\sqrt{\tilde{y}^2 + 1}. \tag{3.25}$$

The small $\tilde{y}$ limit ($\tilde{y} \ll 1$) corresponds to non-relativistic fermions, whereas $\tilde{y} \gg 1$ to the relativistic particles. The asymptotic behavior of the functions $f(\tilde{y})$ and $g(\tilde{y})$ are given by the relations:

$$\tilde{y} \ll 1 : \; f(\tilde{y}) \to \frac{8}{5}\tilde{y}^5\left(1 - \frac{5}{14}\tilde{y}^2\right), \; g(\tilde{y}) \to 8\tilde{y}^3 + \frac{12}{5}\tilde{y}^5\left(1 - \frac{5}{28}\tilde{y}^2\right). \tag{3.26}$$

Using (3.26) the energy density and pressure in the non-relativistic limit can be obtained

$$u_f = n_f m_f c^2 + g_s \frac{4\pi m_f^4 c^5}{10h^3} \tilde{y}^5\left(1 - \frac{5}{28}\tilde{y}^2\right), \tag{3.27}$$

$$P_f = g_s \frac{4\pi m_f^4 c^5}{15h^3} \tilde{y}^5 \left(1 - \frac{5}{14}\tilde{y}^2\right). \tag{3.28}$$

Retaining only the lowest order terms in the approximate forms of the function $f(\tilde{y})$ the pressure of the completely degenerate, non-relativistic fermion gas can be obtained from the relation

$$P_f = \frac{h^2}{5m_f} \left(\frac{3}{8\pi}\right)^{2/3} n_f^{5/3}. \tag{3.29}$$

The internal energy density of non-relativistic fermions and pressure are related by

$$P_f = \frac{2}{3} u_f. \tag{3.30}$$

The extreme relativistic limit $\tilde{y} \gg 1$ of the functions $f(\tilde{y})$ and $g(\tilde{y})$ is given by the equation

$$\tilde{y} \gg 1 : \; f(\tilde{y}) \approx 2\tilde{y}^4 \left(1 - \frac{1}{\tilde{y}^2}\right), \; g(\tilde{y}) \approx 6\tilde{y}^4 \left(1 + \frac{1}{\tilde{y}^2}\right). \tag{3.31}$$

The energy density and pressure obtained from this approximate form of the functions $f(\tilde{y})$ and $g(\tilde{y})$ (3.31) are given by

$$u_f = g_s \frac{m_f^4 c^5 \pi}{h} \tilde{y}^4 \left(1 + \frac{1}{\tilde{y}^2}\right), \tag{3.32}$$

$$P_f = g_s \frac{m_f^4 c^5 \pi}{3h} \tilde{y}^4 \left(1 - \frac{1}{\tilde{y}^2}\right). \tag{3.33}$$

The EOS can be written in the polytropic form

$$P_f = K_f n^\Gamma, \tag{3.34}$$

where Γ is the adiabatic exponent of the gas defined as

$$\Gamma = \left(\frac{\partial \ln P}{\partial \ln \rho}\right)_S \tag{3.35}$$

and K_f is a constant, the index $f = e, n$ denotes electrons or neutrons, n is the particle number density.

The two limiting cases (non-relativistic and ultra-relativistic) can be written as follows:

- non-relativistic electrons

$$\Gamma = \frac{5}{3},\ K_e = \frac{1}{20}\left(\frac{3}{\pi}\right)^{2/3}\frac{h^2}{m_e}, \tag{3.36}$$

- non-relativistic neutrons

$$\Gamma = \frac{5}{3},\ K_n = \frac{1}{20}\left(\frac{3}{\pi}\right)^{2/3}\frac{h^2}{m_n}, \tag{3.37}$$

- ultra-relativistic electrons

$$\Gamma = \frac{4}{3},\ K_e = \left(\frac{3}{\pi}\right)^{1/3}\frac{hc}{8}, \tag{3.38}$$

- ultra-relativistic neutrons

$$\Gamma = \frac{4}{3},\ K_n = \left(\frac{3}{\pi}\right)^{1/3}\frac{hc}{8}. \tag{3.39}$$

3.2.2 Partially degenerate fermion gas

In the non-relativistic case the both parameters α and $\beta \gg 1$ [8]. The pressure, internal energy density, particle number density and entropy defined previously by equations (3.13), (3.14), (3.15) and (3.16) take the following forms:

$$n_f = g_s\frac{2\pi}{h^3}(2m_f k_B T)^{3/2}F_{1/2}(\beta-\alpha), \tag{3.40}$$

$$u_f = g_s\frac{2\pi}{h^3}(2m_f k_B T)^{3/2}[k_B T F_{3/2}(\beta-\alpha) + m_f c^2 F_{1/2}(\beta-\alpha)], \tag{3.41}$$

$$P_f = g_s\frac{4\pi}{3h^3}(2m_f k_B T)^{3/2}k_B T F_{3/2}(\beta-\alpha), \tag{3.42}$$

$$S_e = g_s\frac{2\pi}{h^3}(2m_f k_B T)^{3/2}k_B\left[\frac{5}{3}F_{3/2}(\beta-\alpha) - (\beta-\alpha)F_{1/2}(\beta-\alpha)\right]. \tag{3.43}$$

These expressions are given in terms of Fermi–Dirac integrals $F_\nu(\xi)$ which are defined by [8], [61]

$$F_\nu(\xi) = \int_0^\infty \frac{y^\nu dy}{1 + exp(y-\xi)}, \tag{3.44}$$

where

$$y = \frac{x^2}{2\alpha} = \frac{p^2}{2m_f k_B T},\ \xi = \beta - \alpha. \tag{3.45}$$

If $\beta - \alpha \ll 1$, $f(p) \ll 1$, the degeneracy is negligible and the equations (3.41), (3.42), (3.43) take the form:

$$u_f = n_f m_f c^2 + \frac{3}{2} k_B T n_f \left(1 + \frac{\alpha^{3/2} y^3}{12\sqrt{\pi}}\right), \tag{3.46}$$

$$P_f = \frac{3}{2} k_B T n_f \left(1 + \frac{\alpha^{3/2} y^3}{12\sqrt{\pi}}\right), \tag{3.47}$$

$$S_f = k_B n_f \left[\frac{5}{2} \ln\left(\sqrt{\frac{2}{\pi}} \frac{\alpha^{3/2} y^3}{3}\right) + \frac{\alpha^{3/2} y^3}{24\sqrt{\pi}}\right]. \tag{3.48}$$

In the limit of strong degeneracy $\beta - \alpha \gg 1$. Fermi integrals in this approximation have the form

$$F_{1/2}(\beta - \alpha) = \frac{2}{3}(\beta - \alpha)^{3/2} + \frac{\pi^2}{12\sqrt{\beta - \alpha}}, \tag{3.49}$$

$$F_{3/2}(\beta - \alpha) = \frac{2}{5}(\beta - \alpha)^{5/2} + \frac{\pi^2}{4}(\beta - \alpha)^{1/2}. \tag{3.50}$$

Using equations (3.40), (3.41), (3.42) and (3.43) and the relation

$$\beta - \alpha = \frac{\alpha y^2}{2}\left(1 - \frac{\pi^2}{3\alpha^2 y^4}\right), \tag{3.51}$$

the fermion number density, energy density, pressure and entropy can be calculated.

The same analysis can be performed for the limit of ultra-relativistic particles. Neglecting the parameter α in the integrals (3.13), (3.14), (3.15) and (3.16) they reduce to the form:

$$I_{n^\pm} = F_2(\pm\beta), \qquad I_{P^\pm} = I_{E^\pm} = F_3(\pm\beta). \tag{3.52}$$

Using the properties of Fermi integrals with an integer subscript

$$\frac{F_\nu(x)}{dx} = \nu F_{\nu-1}(x), \quad F_0(x) = \int_0^\infty \frac{dy}{1 + exp(y - x)} = \ln(1 + e^x),$$

$$F_0(x) - F_0(-x) = x, \tag{3.53}$$

and employing the relation

$$F_\nu(0) = \int_0^\infty \frac{x^{\nu-1}dx}{1+e^x} = (1-2^{1-\nu})\Gamma(\nu)\zeta(\nu), \;\; \nu > 0 \tag{3.54}$$

the thermodynamic functions can be written as:

$$n_f = \frac{g_s 4\pi}{3}\left(\frac{k_B T}{hc}\right)^3 (\beta^3 + \pi^2\beta), \tag{3.55}$$

$$u_{f^-} + u_{f^+} = g_s\pi\left(\frac{k_B T}{hc}\right)^3 (\beta^4 + 2\pi^2\beta^2 + \frac{7\pi^4}{15})k_B T, \tag{3.56}$$

$$P_{f^-} + P_{f^+} = \frac{g_s\pi}{3}\left(\frac{k_B T}{hc}\right)^3 (\beta^4 + 2\pi^2\beta^2 + \frac{7\pi^4}{15})k_B T, \tag{3.57}$$

$$S_{f^-} + S_{f^+} = \frac{g_s\pi}{6}\left(\frac{k_B T}{hc}\right)^3 (\pi^2\beta^2 + \frac{7\pi^4}{15})k_B. \tag{3.58}$$

In the case of strong degeneracy $\beta \gg \alpha$ and $\beta \gg 1$, and the parameter β takes the form

$$\beta = \alpha y\left(1 - \frac{\pi^2}{3\alpha^2 y^2}\right). \tag{3.59}$$

Using equation (3.59) and neglecting the contributions of antiparticles the energy density, pressure and entropy can be calculated from equations (3.56), (3.57) and (3.58).

When the density of the ultra-relativistic fermion gas is very low the limiting form of β

$$\beta = \frac{y^3\alpha^3}{\pi^2}\left(1 - \frac{y^6\alpha^6}{\pi^6}\right), \tag{3.60}$$

allows one to calculate the thermodynamic functions from equations (3.56), (3.57) and (3.58).

3.2.3 Neutrino gas

Assuming the rest mass of the neutrino is zero ($m_\nu = 0$), the thermodynamical properties of the neutrino gas, namely the neutrino number

density n_ν, neutrino energy density u_ν and neutrino pressure P_ν are given by the following equations:

$$n_\nu = 4\pi g_s \left(\frac{k_B T}{ch}\right)^3 (F_2(\beta) - F_2(-\beta)) = g_s \frac{4\pi}{3} \left(\frac{k_B T}{ch}\right)^3 (\beta^3 + \pi^2 \beta),$$

$$\begin{aligned} u_\nu = 3P_\nu &= 4\pi g_s \left(\frac{k_B T}{ch}\right)^3 (F_3(\beta) + F_3(-\beta)) \\ &= 8\pi g_s \left(\frac{k_B T}{ch}\right)^3 \left(\beta^4 + 2\pi^2 \beta^2 + \frac{7}{15}\pi^4\right) k_B T, \end{aligned} \tag{3.61}$$

for neutrino $g_s = 1$.

The asymptotic behavior of the neutrino gas pressure concerns the case of extreme degeneracy when $\beta \gg 1$, then the neutrino pressure reduces to the following form

$$P_\nu = \frac{hc}{4} \left(\frac{3}{4\pi}\right)^{1/3} n_\nu^{4/3}, \tag{3.62}$$

where neutrino number density is given by the relation

$$n_\nu = 4\pi \left(\frac{k_B T}{hc}\right)^3 F_2(\beta). \tag{3.63}$$

In the case of weak degeneracy the neutrino gas pressure is given by

$$P_\nu = \frac{n_\nu k_B T}{3} \left[1 + \frac{n_\nu}{128\pi} \left(\frac{hc}{k_B T}\right)^3\right]. \tag{3.64}$$

If the neutrino chemical potential equals zero ($\beta = 0$) the neutrino energy density and pressure can be simplified to give

$$u_\nu = 3P_\nu = \tilde{a} T^4, \tag{3.65}$$

where

$$\tilde{a} = \frac{7\pi^5 k_B^4}{30 h^3 c^3}. \tag{3.66}$$

The obtained result (3.65) is the neutrino analogue of the Stefan–Boltzmann (3.10) law. Comparing equations (3.10) and (3.65) one can see that the difference between photon and neutrino statistics is reflected in the factor 7/16.

Chapter 4

Equation of state of stellar matter

The analysis of theoretical models which describe the different stages of stellar evolution, commences with the phase of a contracting protostar through the exhaustion of subsequent nuclear fuel, to final extinction and can be conducted by means of the EOS which changes gradually with the temperature and density.

4.1 The ideal classical gas

The longest phase in the life of a star is a state in which stellar matter can be characterized by a high temperature and a relatively low density and can be modelled based on a non-relativistic, non-degenerate perfect gas approximation with the EOS having the following form [6], [8]

$$P = nk_BT = \frac{\Re}{\mu_{mol}}\rho T, \tag{4.1}$$

where n is the number of particles per unit volume, μ_{mol} is the molecular weight, the density of matter equals $\rho = n\mu_{mol}m_u$, k_B is the Boltzmann constant, m_u – the atomic mass unit and $\Re = k_B/m_u$ – the universal gas constant.

In the central regions of stars all atoms are almost fully ionized and deep inside a star there is a mixture of two gases: the free electron gas and the gas of nuclei. The chemical composition can be specified by

the weight fractions of nuclei of type i and characterized by the molecular weight μ_{mol_i} and the charge number Z_i. The number of nuclei per unit volume n_i equals

$$n_i = \frac{\rho X_i}{m\mu_{mol_i}}. \tag{4.2}$$

The gas pressure P is the sum of partial pressures

$$P_{gas} = P_e + \sum_i P_i = \sum_i (1 + Z_i) n_i k_B T \tag{4.3}$$

and can be written as

$$P = \Re \sum_i \frac{X_i(1 + Z_i)}{\mu_{mol_i}} \rho T \equiv \frac{\Re}{\mu_{mol}} \rho T, \tag{4.4}$$

with the mean molecular weight

$$\mu_{mol} = \left(\sum_i \frac{X_i(1 + Z_i)}{\mu_{mol_i}} \right)^{-1}, \tag{4.5}$$

which allows one to consider a mixture of ideal gases as a uniform ideal gas.

The equation (4.5) is valid for a gas of fully ionized atoms. For the case of a neutral gas it takes the form

$$\mu_{mol} = \left(\sum_i \frac{X_i}{\mu_{mol_i}} \right)^{-1}. \tag{4.6}$$

In general, a star consists of matter and radiation in thermodynamic equilibrium and the total pressure is the sum of the gas pressure and the radiation pressure

$$P = P_{gas} + P_{rad} = \frac{\Re}{\mu_{mol}} \rho T + \frac{a}{3} T^4. \tag{4.7}$$

The radiation pressure although very small for low massive stars, cannot be neglected in stars more massive than the Sun. For densities lower than the limiting density ρ_{ph} given by

$$\rho_{ph} = 3.0 \times 10^{-23} \mu_{mol} T^3 \mathrm{gcm}^{-3}, \tag{4.8}$$

where μ_{mol} denotes the mean molecular weight, the pressure of photon gas dominates the pressure of the classical perfect gas.

4.2 The degenerate gas

The mass of a star is a key factor in determining the stellar evolution. Low-mass stars developing a degenerate core can evolve to the white dwarf stage whereas evolutionary models of massive stars, with the main sequence mass exceeding $8\,M_\odot$, show that their evolution proceeds through sequences of consecutive stages of nuclear burning until the iron core is formed. The interior composition of a massive star in a very advanced stage of evolution prior to core collapse reveals a shell structure. Each shell has a different chemical composition of gradually heavier elements. The formation of ^{56}Fe nuclei, with the maximum binding energy per nucleus, indicates the beginning of the end of a massive star as a normal star [6].

As a star contracts and its density increases, electrons which initially form a dilute, classical gas become more relativistic and they start to form dense, degenerate quantum gas. During the later stages of stellar evolution or in supernova explosion, the calculation of thermodynamic functions requires the full relativistic expression for the electron energy and momentum. It becomes necessary to take into account the Pauli exclusion principle. Electron degeneracy occurs in the advanced phases of stellar evolution, under particular circumstances. In this case the pressure in the stellar interior is provided by the classical perfect ion gas and degenerate electron gas. The stronger the degeneracy of the electron gas, the smaller the contribution of the ion gas to the total pressure. In many cases the partially degenerate electron gas is approximated by a completely degenerate gas. Numerical calculations show that the pressure of completely degenerate electron gas exceeds the non-degenerate electron gas pressure for densities higher than the critical density ρ_{crit}, given by [7]

$$\rho_{crit} = 2.4 \times 10^{-8} T^{3/2} \mu_{mol_e} \mathrm{gcm}^{-3}, \tag{4.9}$$

where μ_{mol_e} is the mean molecular weight per electron, for higher densities the electron gas is completely degenerate.

For almost all classes of stars degeneracy in the electron gas sets in at a sufficiently low temperature so that electrons are mostly non-relativistic. Densities must be higher than $10^6\,\mathrm{gcm}^{-3}$ for a degenerate gas to be relativistic. In most stars relativistic degeneracy becomes important only for such high densities that the degeneracy of the electron gas is complete. The pressure of the degenerate electron gas does not

depend on temperature. This has considerable consequences for stellar structure at certain stages of stellar evolution. When the temperature in the stellar interior exceeds 10^9 K electron gas is relativistic and only partially degenerate.

4.2.1 White dwarfs

In the case of a white dwarf the electrons are fully degenerate [9]. They dominate the pressure of the star while non-relativistic classical ions provide its mass. Depending on the degree of relativity the EOS takes different forms.

For non-relativistic and degenerate electron gas the EOS can be written as follows (3.36)

$$P = \frac{h^2}{20m_e}\left(\frac{3}{\pi}\right)^{2/3} n_e^{5/3}. \tag{4.10}$$

When the electrons are predominantly ultra-relativistic the EOS has the form (3.38)

$$P = \frac{hc^2}{8}\left(\frac{3}{\pi}\right)^{1/3} n_e^{4/3}. \tag{4.11}$$

Equations (4.10) and (4.11) are for ideal, degenerate electron gas. More realistic model of a white dwarf requires taking into consideration corrections. The corrections to be applied are mainly due to electrostatic interactions. For very high densities the effects of weak interaction (inverse β decay) and the possibility of pycnonuclear reactions also have to be included [9].

4.2.2 Proto-neutron stars

After the nuclear fuel is exhausted in a star, nuclear fusion in the central part of the star can no longer supply enough energy to sustain a high thermal pressure. The obtained theoretical models of the evolved massive stars indicate that they develop central iron cores of mass $\sim 1.5\,\mathrm{M}_\odot$. Both the ideal non-degenerate electron gas pressure and the pressure of degenerate electrons attempt to support the core and determine the following EOS of the innermost region of the star [9], [62]

$$\frac{P}{\rho} \simeq \frac{Y_e k_B T}{m_B} + K_\Gamma Y_e^\Gamma \rho^{\Gamma-1}. \tag{4.12}$$

In this equation $Y_e = n_e/n_b$ is the relative electron concentration, ρ is the matter density, n_b is the baryon number density and Γ is the adiabatic exponent of the gas given by equation (3.35). When Γ is close to the critical value 4/3 the core becomes dynamically unstable.

The collapse of the core is accelerated by the combination of two mechanisms [62]: reactions of electron capture and, when the temperature exceeds 5×10^9 K, photodisintegration of iron-peak nuclei into α particles. For densities $Y_e\rho \gg 10^6\,\mathrm{gcm}^{-3}$ electrons are relativistic and their Fermi energy is given by

$$\mu_e \approx 11.0\,\mathrm{MeV}(Y_e\rho_{10})^{1/3}, \tag{4.13}$$

where $Y_e = (n_{e^-} - n_{e^+})/n_b$ is the electron fraction per baryon and $\rho_{10} = \rho/10^{10}\mathrm{gcm}^{-3}$.

For such high energy electron capture is favorable even though it produces nuclei that are unstable to β decay in the laboratory. For nuclei in the iron-peak the threshold Q for electron capture is roughly [6] $Q \approx 190\,\mathrm{MeV}(0.45 - Y_e)$.

Electron capture will occur until the threshold rises to $Q = \mu_e$. Diminishing of the electron concentration leads to a deficit in the pressure and in consequence to the contraction of the core. In the case of extremely relativistic electrons the pressure is given by the relation

$$P_e = \frac{hc}{4}\left(\frac{3}{8\pi}\right)^{1/3} Y_e^{4/3}\left(\frac{\rho}{m_B}\right)^{4/3}. \tag{4.14}$$

Considering the adiabatic exponent Γ [9], [62]

$$\Gamma = \left.\frac{\partial \ln P}{\partial \ln \rho}\right|_{S,Y_e} = \left.\frac{\partial \ln Y_e}{\partial \ln \rho}\right|_S \left.\frac{\partial \ln P}{\partial \ln Y_e}\right|_S = \frac{4}{3}\left(1 + \left.\frac{\partial \ln Y_e}{\partial \ln \rho}\right|_S\right) \tag{4.15}$$

one can see that as the electron capture proceeds the value of the derivative $(\partial \ln Y_e/\partial \ln \rho)_S$ become negative and Γ reduces below 4/3.

The photodissociation of nuclei also brings the adiabatic index of the stellar matter below the value 4/3 and triggers the collapse. At sufficiently high temperature and density the endothermic process

$$\gamma + {}^{56}_{26}\mathrm{Fe} \rightarrow 13\alpha + 4\mathrm{n} \tag{4.16}$$

which requires 124.4 MeV occurs.

The energy needed for this process comes from the kinetic energy of

nuclei and electrons. The resulting thermal pressure deficit is compensated by a further contraction of the core. However, the pressure does not increase to the value which is indispensable to stop the collapse.

Dynamical conditions in the central region of the star split the core into two separate parts: the homologously collapsing inner core and the free falling outer one. In the first region the sound velocity exceeds the infall velocity and the motion is subsonic. Matter contained inside the inner core collapsing as a whole retains its density profile and the infall velocity is proportional to the radius $v(r,t) = a(t)r$. Matter in the outer core is accelerated inward by the change in the pressure gradient, and the velocity is nearly that of free-fall $v \sim 1/\sqrt{r}$.

Theoretically the dual nature of the core has been confirmed by Goldreich and Weber [63] and Yahil and Lattimer [64, 65]. They presented the model of adiabatic collapse of cores with a constant adiabatic exponent. The solution of the problem of the dynamical stability of stars requires analysis of radial perturbations. Stars with $\Gamma < 4/3$ are unstable to radial perturbations and the fastest growing eigen mode is the fundamental mode with a velocity profile given by the equation $v(r,t) = a(t)r$. Additionally it has been shown that for stars with $\Gamma = 4/3$ at the edge of the homologous core the pressure vanishes. Electron captures during the collapse decrease μ_e and reduce the value of the Chandrasekhar mass M_{Ch}. The collapse of the homologous core progresses until the nuclear densities are reached, then nuclear forces are expected to resist compression and stop the further collapse. The innermost shell of matter is expected to rebound and set up a pressure wave out through the homologous core. Due to the fact that the sound speed is in excess of the infall speed this wave travels faster than the infalling matter. The innermost shell is followed by the subsequent layers of matter. The resulting pressure waves collect at the boundary between the inner core and the supersonically falling outer core [62]. When this point reaches the nuclear density and comes to rest, pressure waves which originate from the center become a shock wave and start to propagate through the outer core. The bounced inner core settles into a hydrostatic configuration in the dynamical time scale of milliseconds. The adiabatic exponent of the matter becomes greater than the critical value 4/3.

The outgoing shock wave which travels into the outer core through the material that is falling towards the center dissociates the iron nuclei into protons and neutrons. The shocked region attains high tem-

perature at relatively low densities. Under these conditions electron degeneracy is not high and relativistic positrons are created thermally. The thermal energy is carried out by neutrinos which are produced in the following reactions $e^+ + e^- \rightarrow \nu + \bar{\nu}$, $e^+ + n \rightarrow \bar{\nu} + p$ [9]. Electron neutrinos produced via $e^- + p \rightarrow \nu_e + n$ carry out electron-type lepton number. Deleptonization in the outer envelope proceeds faster than that in the inner core. After stellar collapse the electron neutrinos are trapped inside the matter. This leads to large ν_e chemical potential.

4.2.3 Neutron stars

Properties of neutron star matter must be calculated within a very broad density span ranging from $10^4\,\mathrm{gcm}^{-3}$ at the outer crust to $\sim 10^{15}\,\mathrm{gcm}^{-3}$ in the inner core. The very outer part of a neutron star is an atmosphere of non-degenerate matter composed mostly of hydrogen, helium and other light elements. The composition of the atmosphere determines the surface photon luminosity of a neutron star. Neutron stars in binary systems can accrete matter from their companions. In the case of newly accreted matter neutron star crust is supplemented with hydrogen and helium rich matter. The subsequent stages of the crust evolution include the explosive burning of the helium layer and formation of ^{51}Ni nuclei which transform into ^{56}Fe [66]. Detailed analysis of the crust evolution [66, 67, 68] predicts that the growing layer of the accreted matter replaces the original outer crust in $\sim 10^5$ yr.

The more general case of the crust structure can be considered under the assumption that the crust is built of cold catalyzed matter. Below the surface there is a solid crust which contains mainly Fe nuclei. These nuclei form a lattice. The crust splits into two parts: the outer and the inner crust. The outer crust ranges up to the density $\rho_{drip} \simeq 4.3 \times 10^{11}\,\mathrm{gcm}^{-3}$ and includes only iron nuclei and a degenerate electron gas. The increasing density leads to increasing neutronization by electron captures and at the density ρ_{drip} the neutron rich nuclei begin to release free neutrons. At the onset of the neutron drip the pressure of degenerate electron gas dominates [9]. Thus the matter of the inner crust consists of nuclei, still arranged in a lattice, free electrons and free neutrons. Nuclei in the inner crust are neutron rich isotopes of Zr and Sn. In this region the matter consists of neutrons, electrons and nuclei. The properties of matter in the inner crust have

been described with the use of the Baym–Bethe–Pethick EOS [69]. This EOS has been constructed basing on the compressible liquid drop model of the nuclei [9] and is given by the relation

$$\varepsilon(A, Z, n_N, n_n, V_N) = n_N(W_N + W_L) + (1 - V_N n_N)\varepsilon_N(n_n) + \varepsilon_e(n_e), \tag{4.17}$$

where n_N, n_n and n_e denote the number densities of nuclei, neutrons and electrons, $1 - V_N n_N$ is the fraction of the volume occupied by neutron gas, W_L is the lattice energy per nucleus and W_N is the energy of nucleus.

The energy of nucleus being a sum of the surface energy W_s, the Coulomb energy W_c and the energy per nucleon of the bulk nuclear matter $W(k, x)$

$$W_N = [(1 - x)m_n c^2 + x m_p c^2 + W(k, x)]A + W_s + W_C. \tag{4.18}$$

In equation (4.18) m_n and m_p are neutron and proton masses, x denotes the fractional concentration of protons. The bulk nuclear energy $W(k, x)$ includes the effects of NN interactions but does not include the surface effects and Coulomb interactions. The consistent description of the inner crust matter requires the following form of the neutron gas energy density [9]

$$\varepsilon_n = n_n \left[W(k_n, 0) + m_n c^2 \right]. \tag{4.19}$$

In equation (4.19) the function $W(k_n, 0)$ is given for the proton fraction $x = 0$ and for the neutron number density defined as $n_n = 2k_n^3/3\pi^2$. The parameters in the function $W(k, x)$ are determined by fitting to nuclear data. The density of the lower boundary of the inner crust estimated by Baym et al. [69] is close to the normal nuclear density $\rho_{nucl} = 2.4 \times 10^{14}\,\mathrm{gcm}^{-3}$. However, recent calculations of the density at the inner edge of the crust give much lower inner crust-core transition density $\rho \simeq 1.5 \times 10^{14}\,\mathrm{gcm}^{-3}$. This value has been obtained with the use of Skyrme SLy effective NN interactions [68]. The results obtained with the use of the SLy EOS indicate that the crust core transition takes place as a weak first order phase transition [68], [70]. The EOS of Pandharipande and Ravenhall [71] leads to the crust-core transition through a sequence of phase transitions with the changes of nuclear shapes [70], [72]. Contrary to this situation in the model calculated with the SLy EOS spherical nuclei persist to the crust bottom [70]. For

higher densities nuclei merge and dissolve forming a degenerate gas of neutrons with a small admixture of protons and electrons. As the neutron concentration increases the neutron pressure dominates and the neutron gas considered as ideal degenerate can be a rough approximation to the true EOS. Like the electron gas, the degenerate neutron gas occurs in the non-relativistic and relativistic limit. The requirements of charge neutrality and β-equilibrium demands the presence of electrons and muons. They form a relativistic, completely degenerate gas. The changing values of density and temperature in the stellar matter entails the consequential alteration of the form of the EOS. The approximate boundary lines which divide the ρT plane into the separated regions are given by the equations [7]:

- The pressure due to a ideal non-degenerate gas equals the pressure due to radiation when

$$\frac{N_0 k_B}{\mu_{mol}} \rho T = \frac{1}{3} a T^4, \tag{4.20}$$

  μ_{mol} denotes the mean molecular weight of all free particles in the stellar matter. The pressure is dominated by the photon gas when the following condition is satisfied $\rho < 3.0 \times 10^{-23} \mu T^3$.

- The condition that the pressure of the non-degenerate gas (4.1) equals that of the completely degenerate electron gas, in terms of the density ρ and the mean molecular weight per electron μ_{mol_e}, is given by [7]

$$\frac{N_0 k_B}{\mu_{mol_e}} \rho T = \frac{h^2}{20 m_e} \left(\frac{3}{\pi}\right)^{2/3} \left(\frac{N_0 \rho}{\mu_{mol_e}}\right)^{5/3}. \tag{4.21}$$

  Thus if the inequality $\rho/\mu_{mol_e} > 2.4 \times 10^{-8}\, T^{3/2}$ is satisfied the completely degenerate electron pressure exceeds the non-degenerate electron pressure. These conditions prevail in white dwarf interiors.

- The increasing electron density leads to the condition when electrons have to be considered as relativistic particles. In terms of the density ρ and the mean molecular weight per electron μ_{mol_e} the density has to exceed the value $\rho/\mu_{mol_e} = 7.3 \times 10^6\, \mathrm{gcm}^{-3}$ for a degenerate gas to be relativistic.

Chapter 5

The nuclear equation of state

Nuclear matter can be defined as an infinite system of nucleons with a fixed ratio of neutron to proton numbers and no Coulomb interaction. Our understanding of the form of the equation of state of asymmetric nuclear matter is still inadequate to correctly solve essential problems in both nuclear physics and astrophysics. In general the nuclear matter equation of state, that is the energy per particle, of asymmetric infinite nuclear matter $\epsilon(n_b, f_a)$ [73, 74, 75]

$$\epsilon(n_b, f_a) = \frac{\mathcal{E}}{n_b} \tag{5.1}$$

is a function of baryon number density n_b and the relative neutron excess f_a defined as

$$f_a = \frac{n_n - n_p}{n_n + n_p}, \tag{5.2}$$

where n_n and n_p denote the neutron and proton number densities respectively, the sum $n_n + n_p = n_b$ stands for the total baryon number density. Neutron and proton number densities $n_B, B = n, p$ are related to their Fermi momentum k_F by the relation

$$n_B = \frac{1}{3\pi^2} k_F^3. \tag{5.3}$$

$\mathcal{E}$ in equation (5.1) denotes the total energy of the nuclear system.

The properties of asymmetric nuclear matter can be studied with the use of the empirical parabolic approximation which allows one to expand the energy per particle of asymmetric nuclear matter in a Taylor series in f_a [12], [13], [69], [76], [77], [78]

$$\epsilon(n_b, f_a) = \epsilon(n_b, 0) + S_2(n_b) f_a^2 + S_4(n_b) f_a^4 + \dots \tag{5.4}$$

The factor f_a makes the quartic $S_4(n_b)$ term contribution negligible. Also the analysis performed with the use of realistic interactions indicates the dominant role of the $S_2(n_b)$ term not only in the vicinity of the saturation point but even at higher densities [12], [16], [79].

The expansion given in equation (5.4) enables the analysis of the function $\epsilon(n_b, f_a)$ in terms of the energy of symmetric nuclear matter $\epsilon(n_b, 0)$ and the symmetry energy $S_2(n_b)$. Subsequently expanding the function $\epsilon(n_b, f_a)$ around the equilibrium density n_0 in a Taylor series in n_b, the following expressions for the two successive terms $\epsilon(n_b, 0)$ and $S_2(n_b)$ can be obtained:

$$\varepsilon(n_b, 0) = \varepsilon(n_0) + \frac{1}{2}(n_b - n_0)^2 \frac{\partial^2 \varepsilon}{\partial n_b^2} + \dots \tag{5.5}$$

$$S_2(n_b) = S_2(n_0) + (n_b - n_0)\frac{\partial S_2}{\partial n_b} + \frac{1}{2}(n_b - n_0)^2 \frac{\partial^2 S_2}{\partial n_b^2} + \dots \tag{5.6}$$

with all derivatives evaluated at the point $(n_0, 0)$.

This very point denotes the position of the state defined as the equilibrium state of symmetric nuclear matter $\varepsilon(n_0, 0)$ with minimum energy per nucleon and is characterized by the condition $\partial\varepsilon(n_b, 0)/\partial n_b = P(n_0, 0) = 0$. Thus, the linear term in the Taylor expansion (5.5) vanishes.

Gathering altogether the terms of the expansion in n_b and in f_a the approximated form of the EOS can be written as [73], [75]

$$\varepsilon(n_b, f_a) = \varepsilon(n_0) + \frac{1}{18}(K_0 + K_s f_a^2)\left(\frac{n_b - n_0}{n_0}\right)^2 + \left[J + \frac{L}{3}\left(\frac{n_b - n_0}{n_0}\right)\right] f_a^2. \tag{5.7}$$

The above formula is parameterized by the following coefficients: n_0, $\varepsilon(n_0)$, K_0, J, K_s, L which determine the density dependence of the equation of state $\varepsilon(n_b, f_a)$. Thus, having obtained the equation of state, each individual term that enters the formula (5.7) can be calculated. Comparison of equations (5.5), (5.6) and (5.7) gives the definition of the above stated coefficients.

5.1 Compressibility of nuclear matter

The definition of the compressibility χ is given by [80]

$$\chi = -\frac{1}{V}\frac{\partial V}{\partial P} = \frac{1}{n}\left(\frac{dP}{dn}\right)^{-1}, \tag{5.8}$$

where n is the particle number density. The pressure P is related to the energy per baryon $\mathcal{E}(n_b, f_a)/n_b$ by:

$$P(n_b, f_a) = -\frac{\partial(\mathcal{E}(n_b, f_a)/n_b)}{\partial(1/n_b)} = n_b^2\frac{\partial\epsilon(n_b, f_a)}{\partial n_b}. \tag{5.9}$$

In nuclear physics the incompressibility factor is defined

$$K(n_b, f_a) = 9\frac{\partial P}{\partial n_b}, \tag{5.10}$$

which is equivalent to

$$K(n_b, f_a) = 9\left[n_b^2\frac{\partial^2\epsilon(n_b, f_a)}{\partial n_b^2} + 2n_b\frac{\partial\epsilon(n_b, f_a)}{\partial n_b}\right]. \tag{5.11}$$

At the saturation density n_0 the condition $P(n_0, 0) = 0$ prevails and one can specify the compression modulus K_0

$$K_0 = 9n_0^2\left.\frac{\partial^2\epsilon(n_b, 0)}{\partial n_b^2}\right|_{n_0} \tag{5.12}$$

which is defined only at the saturation density n_0. The importance of determining the compression modulus stems from its impact on both nuclear structure and supernova explosion and on the physics of neutron stars [81]. In order to obtain information on the value of the incompressibility the phenomenology of the compressional modes in finite nuclei has to be used . The discovery of Isoscalar Giant Monopole Resonance (ISGMR) in nuclei (the nuclear breathing-mode) is considered to be the most accurate source of information on nuclear matter incompressibility [82, 83]. The first experimental data came from the 1970s. These data have been significantly improved especially by the (α, α') inelastic scattering experiments [84]. In light nuclei this resonance is rather fragmented, while in medium-heavy nuclei it corresponds to a single peak of energy $E_{ISGMR} \sim 80A^{-1/3}$ MeV [85].

Table 5.1: ISGMR centroid energy (Taken from [87])

Nucleus	Exp	Nucleus	Exp
^{90}Zr	17.89 ± 0.2	^{116}Sn	16.07 ± 0.12
^{144}Sm	15.39 ± 0.28	^{208}Pb	14.17 ± 0.28

The data derived from the measurements of ^{90}Zr, ^{116}Sn, ^{144}Sm and ^{208}Pb [86] increased the knowledge of the ISGMR properties. The obtained results which indicate the position of the giant monopole resonance in the above mentioned nuclei are given in Table 5.1 [87].

Theoretical calculations indicate that there exists a discrepancy between relativistic and non-relativistic models in the prediction of the compression modulus of nuclear matter. In the paper by Blaizot [88] the expression which shows the connection between the finite nucleus incompressibility K_A and the energy E_{ISGMR} measured in the laboratory has been formulated

$$E_{ISGMR} = \sqrt{\frac{\hbar^2}{m} \frac{K_A}{< r^2 >}}, \tag{5.13}$$

where m denotes the nucleon mass and $< r^2 >$ the ground state mean square radius.

Non-relativistic calculations that reproduce the distribution of isoscalar monopole strength using Hartree–Fock plus random-phase approximation (RPA) approaches with the Skyrme and Gogny interactions give the estimated value of the compression modulus in the range of $K = 210 - 220$ MeV [88], whereas relativistic models which successfully reproduce the excitation energy of the ISGMR indicate a larger value of $K \simeq 275$ MeV [41] [89]. Piekarewicz in his paper [90] and Agrawal et al. [87] suggest that these differences can partly result in the still incomplete knowledge of the density dependence of the symmetry energy in the considered models.

The compression modulus K_0 of symmetric nuclear matter is an essential characteristic of the EOS. It specifies the curvature of the EOS around the saturation density n_0. However, the second term in equation (5.11) gives sizeable contributions to $K(n_b, f_a)$ at densities $n \gg n_0$ and the information about the incompressibility of nuclear matter will

be imprinted in the high density behavior of the EOS, namely in the property known as the stiffness of the equation of state which characterizes its behavior with increasing asymmetry and baryon number density. The incompressibility of asymmetric nuclear matter can be approximated by the following expression

$$K(n_b, f_a) = K_0(n_b) + K_{asym}(n_b) f_a^2, \tag{5.14}$$

where $K_{asym}(n_b)$ is given by

$$K_{asym}(n_b) = K_{sym}(n_b) + 6L(n_b). \tag{5.15}$$

The parameters L and K_{sym} are related to the curvature and slope in the density dependence of the symmetry energy and are defined as follows

$$L = \frac{3}{2}\left(n_b \frac{\partial^3 \epsilon(n_b, f_a)}{\partial n_b \partial f_a^2}\right)_{n_b=n_0, f_a=0} \tag{5.16}$$

and

$$K_s = \frac{9}{2} n_b^2 \left.\frac{\partial^4 \epsilon(n_b, f_a)}{\partial n_b^2 \partial f_a^2}\right|_{n_b=n_0, f_a=0} = -6L + \frac{1}{2}\left.\frac{\partial^2 K}{\partial f_a^2}\right|_{n_b=n_0, f_a=0}. \tag{5.17}$$

Baron, Cooperstein and Kahana [91] have found that the explanation of the prompt type II supernova model demands a softening of the EOS for asymmetric nuclear matter at high density. The analysis of nuclear matter incompressibility has been made within the non-relativistic Hartree–Fock approach for the density dependant versions of the Reid and Paris potentials [92]. The obtained results show that with the increasing value of the neutron-proton asymmetry the incompressibility at saturation K_0 becomes smaller. The density dependence of the incompressibility of asymmetric nuclear matter studied for different values of the asymmetry parameter f_a shows that the more asymmetric matter leads to a stiffer EOS for the model which gives a K_0 value smaller than 200 MeV. This result is consistent with the one obtained within the relativistic Brueckner–Hartree–Fock model.

When the value of K_0 is larger than 200 MeV the more asymmetric matter is stiffer than the symmetric one for densities up to $1.5\, n_0$. For higher densities the more asymmetric matter becomes softer than the corresponding symmetric nuclear matter. Kolehmeinen et al. [93] in their paper perform an analysis of the isospin dependence of the nuclear

incompressibility and density at saturation using the Skyrme-type interaction in the extended Thomas–Fermi approach. They found that the isospin dependence can be parameterized as a quadratic function of the asymmetry parameter f_a

$$K_0(f_a) = K_0(0)(1 - af_a^2), \tag{5.18}$$

where a is a parameter.

The form of the functional dependence of the compression modulus on the asymmetry parameter has been confirmed by the calculations performed for other nuclear models. For example, Bombaci and Lombardo obtained similar results for the non-relativistic Brueckner–Bethe–Goldstone model with the Paris interaction [16] or Wiringa et al. [13] using the variational many body approach with the Argonne and Urbana two-body potential av14 and uv14 supplemented with the Urbana three-body potential UVII. In the case of relativistic models, the tendency of decreasing compression modulus with increasing isospin asymmetry has also been found. This was of special importance for the construction of supernova explosion models for which the assumption about the softening of the EOS for more asymmetric matter nuclear matter has been essential in order to generate a successful prompt explosion. However, those earlier models of supernova failed to predict the expected prompt explosion.

5.2 Nuclear symmetry energy

The correct form of the EOS for asymmetric nuclear matter is of primary importance not only for understanding the structure of radioactive nuclei but also would have important consequences for the properties and structure of neutron stars, especially for their cooling history [76], [96], [97]. Theoretical calculations of the symmetry energy and its density dependence, like the analysis of other properties of nuclear systems, are based on different approaches which can be grouped into two main categories: microscopic and phenomenological.

Each of them can be subdivided into relativistic and non-relativistic. The first category incorporates methods which use the various realistic models of the NN interaction which are adjusted to describe NN scattering phase shifts. These methods fall into two main groups: in the first calculations have been performed in the framework of the variational approach and in the second Brueckner-type approximation has

been employed [16], [17]. The version of the Argonne potential av14 or Urbana uv14 used in the variational calculations did not reproduce satisfactory saturation properties of nuclear matter. The phenomenological three-nucleon interaction with parameters well adjusted to obtain, together with the two-nucleon interaction, the correct value of the nuclear matter saturation properties, has to be introduced. Calculations performed with the use of variational chain summation method and the Argonne av18 [98] potential give satisfactory fit to the NN scattering data. This method has been incorporated to investigate properties of nuclear matter and the structure of neutron stars. The non-relativistic case of the Brueckner-type calculations, the Brueckner–Hartree–Fock (BHF) [16] method which incorporates the realistic two-nucleon potentials (for example the Bonn or Paris potential) does not saturate at empirical density. The relativistic Dirac–Brueckner–Hartree–Fock (DBHF) approach provides a better description of the nuclear saturation properties of symmetric nuclear matter [18], [20], [94]. In the phenomenological approach the non-relativistic Hartree–Fock and Fermi calculations which employed the Skyrme-type effective NN interactions satisfactorily reproduce various properties of nuclei [23, 95].

According to the approximation presented by equation (5.4) the analysis of the density dependence of the symmetry energy can be performed with the use of the empirical parabolic law

$$\epsilon(n_b, f_a) = \epsilon(n_b, 0) + S_2(n_b) f_a^2, \tag{5.19}$$

where $\epsilon(n_b, 0)$ is the energy per particle of symmetric nuclear matter and $S_2(n_b) \equiv E_{sym}(n_b)$ given by

$$E_{sym}(n_b) = \frac{1}{2} \frac{\partial^2 \epsilon(n_b, f_a)}{\partial f_a^2}\bigg|_{f_a=0} \tag{5.20}$$

is the bulk symmetry energy. Both relativistic and non-relativistic calculations confirm the validity of this empirical parabolic law for the equation of state of asymmetric nuclear matter not only for small isospin asymmetries but also when $f_a \sim 1$ [16], [79]. This has been presented in Fig. 5.1 where the binding energy as a function of the asymmetry parameter f_a^2 for the chosen values of densities has been plotted. Calculations have been done for the TM1 parameter set supplemented with the δ meson.

Relation (5.19) allows one to calculate the symmetry energy as a difference between the energy per particle for two extreme cases, pure

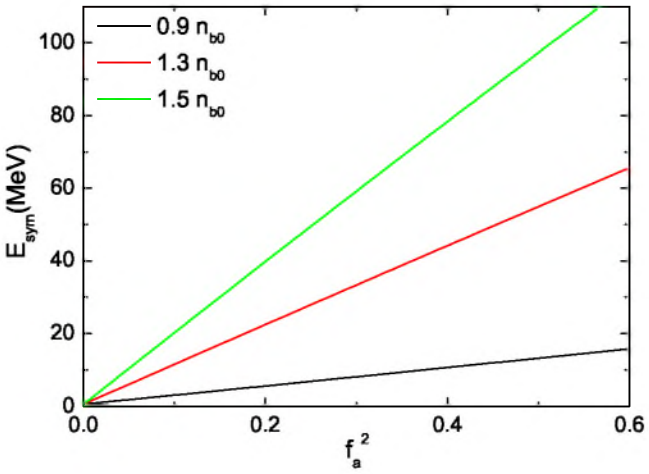

Figure 5.1: The binding energy per nucleon as a function of f_a^2 calculated for the chosen value of the nucleon density

neutron matter with $f_a = 1$ and symmetric nuclear matter with $f_a = 0$

$$E_{sym}(n_b) = \epsilon(n_b, 1) - \epsilon(n_b, 0). \tag{5.21}$$

The density dependence of the symmetry energy has been analyzed with the use of different models and approaches. All the obtained results give the value of the symmetry energy around the saturation density, known as the symmetry energy coefficient $E_{sym}(n_0) \equiv J$, in the range of 27–38 MeV which is in reasonable agreement with the empirical values in the range of 30 ± 4 MeV [22], [23], [95]. However, the high density predictions for the symmetry energy which are relevant to both radioactive nuclei and neutron stars are different. In the relativistic mean field approach there is a linear density dependence of the symmetry energy [99], [100], [102], [103], [104] whereas the Bethe–Goldstone theory predicts a $n_b^{1/3}$ dependence.

Calculations based on variational many-body theory performed by Wiringa et al. [13] with the use of the Argonne two body potential av14 or Urbana uv14 supplemented with the three-body potential UVII or TNI lead to the form of the symmetry energy which initially increases with density and after reaching a maximum decreases with density. Moreover the addition of the three-body interactions causes

the symmetry energy to vanish at high density. In all calculations the kinetic contribution to the symmetry energy is almost the same. So the reason for the discrepancy between different model predictions is the isospin-dependent potential term in the symmetry energy. In the relativistic mean field theory this potential term is always repulsive and increases linearly with density. When the isovector sector includes only the ρ meson the symmetry energy coefficient $E_{sym}(n_0)$ is given by the relation

$$E_{sym}(n_0) = \left(\frac{g_{\rho N}}{m_\rho}\right)^2 \frac{k_0^3}{12\pi^2} + \frac{k_0^2}{6(k_0^2 + m_0^2)^{1/2}}, \tag{5.22}$$

where k_0 denotes the Fermi energy at saturation of symmetric nuclear matter $k_0 = (3\pi^2 n_0/2)^{1/3}$.

For comparison, the density dependence of the symmetry energy calculated with the variational many-body approach for the uv14 potential supplemented by TNI interaction shows that the isospin-dependent potential which is repulsive for lower densities becomes attractive when the density increases.

Engvik et al. [105] have made an attempt to find the explanation for the differences in the density dependence of the symmetry energy. These differences may be caused either by the method used to solve the many body problem or by the employed particular form of the nucleon-nucleon potentials. However, in order to eliminate the influence of the different solutions of the many body problem all calculations have been done within the non-relativistic Brueckner–Hartree–Fock approach. The earlier predictions for the high density behavior of the symmetry energy based on calculations done for various realistic models of the NN potentials that have been fitted to describe the NN scattering phase shifts lead to different results, which can be summarized as follows: the Argonne av14 potential [106] gives the symmetry energy nearly constant for densities over twice that of nuclear saturation density n_0, the Reid potential [107] gives at high densities an even lower value of the symmetry energy, whereas the symmetry energy calculated with the use of the Paris potential [108] almost linearly increases with density.

All used potentials were adjusted to describe NN scattering phase shifts but they do not predict exactly the same NN phase and they do not agree accurately with the modern phase shift analysis. New potentials like the CD-Bonn [109], Argonne av18 [110] or the new Nijmegen

[111] have been constructed. They fit with high precision the data for pp and np scattering below 350 MeV and they predict the same NN phases. All these new potentials have been used to analyze the density dependence of the symmetry energy. The obtained results show that there is no saturation of the symmetry energy for any of the considered models and the differences between the individual cases are much smaller than those between the older versions of the NN potential. The differences in the density dependence of the symmetry energy lead to variations in the proton fraction. The condition of β-equilibrium in terms of the symmetry energy can be given by the following relation

$$\mu_{asym} \equiv \mu_e = \mu_n - \mu_p = -\frac{\partial \epsilon(n_b, f_a)}{\partial Y_p} = 4E_{sym}(n_b)(1 - Y_p), \quad (5.23)$$

where μ_{asym} denotes the difference between nucleon chemical potentials.

Chapter 6

Relativistic mean field model

6.1 Walecka model and its extensions

The relativistic quantum field theory of interacting many-body systems based on hadronic degrees of freedom is known as the quantum hadrodynamic (QHD) [24], [27], [28], [29], [30]. This model is very successful in describing the bulk and single particle properties of nuclear matter and finite nuclei [25, 31].

The original renormalizable model (QHD-I) contains nucleons interacting through the exchange of isoscalar, Lorentz scalar σ and vector ω mesons [112]. This model leads to a very large, unrealistic value of the compression modulus $K_0 = 545$ MeV. In order to improve the incompressibility and finite nuclei results the QHD-I model has been supplemented with additional cubic and quartic scalar self-interaction terms (the non-linear $\sigma - \omega$ model). As a result a reduced value of the compression modulus, consistent with the isoscalar giant monopole resonance in ^{208}Pb has been obtained [30]. The ω meson quartic self-interaction term has been considered by Bodmer [34] to obtain the positive value of the quartic scalar self-interaction coefficient as its negative value may mean that the energy spectrum has no lower bound. The inclusion of this vector meson quartic self-interaction term leads to a softening of the EOS at high density and has profound consequences for neutron star masses. Models that take into account this term give the maximum mass of a neutron star as 1.8 $M_\odot$, while the maximum mass of a neutron star predicted by models that exclude the non-linear vector meson term is in the order of 2.8 $M_\odot$. This very high value of neutron star mass has been obtained even if the considered

models give good descriptions of the giant monopole resonance. The reason for this discrepancy can be explained by the fact that the giant monopole resonance in nuclei providing direct information on the compressibility of nuclear matter at and in the vicinity of the saturation density leaves its high-density behavior undetermined. Gmuca [113] used the quartic ω meson self-interaction term in a non-linear $\sigma - \omega$ model for parameterizing Dirac–Brueckner–Hartree–Fock calculations of nuclear matter and Toki et al [100] applied it to study finite nuclei and neutron stars.

The Lagrangian of nuclear matter constructed on the basis of the original Walecka model and extended by the inclusion of nonlinear scalar and vector self-interaction terms can be presented in the following form [2], [112]

$$\begin{aligned} \mathcal{L} = \bar{\psi}_N(i\gamma^\mu D_\mu - (m_N - g_{\sigma N}\sigma))\psi_N &+ \frac{1}{2}\partial_\mu\sigma\partial^\mu\sigma - \\ -\frac{1}{4}\Omega_{\mu\nu}\Omega^{\mu\nu} - \frac{1}{4}R^a_{\mu\nu}R^{a\mu\nu} + \frac{1}{2}m^2_\omega\omega_\mu\omega^\mu &+ \frac{1}{2}m_\rho\rho^a_\mu\rho^{a\mu} - \\ -U(\sigma) + \frac{1}{4!}c_3(\omega_\mu\omega^\mu)^2 &+ \frac{1}{6}\zeta(\rho^a_\mu\rho^{a\mu})^2, \end{aligned} \tag{6.1}$$

where

$$\psi_N = \begin{pmatrix} \psi_p \\ \psi_n \end{pmatrix}$$

is the spinor of nucleon field, D_μ denotes the covariant derivative defined as

$$D_\mu = \partial_\mu + ig_{\omega N}\omega_\mu + ig_{\rho N}I_{3N}\tau^a\rho^a_\mu, \tag{6.2}$$

and the scalar potential function $U(\sigma)$ possesses a well-known polynomial form

$$U(\sigma) = \frac{1}{2}m^2_\sigma\sigma^2 + \frac{1}{3}g_3\sigma^3 + \frac{1}{4}g_4\sigma^4. \tag{6.3}$$

The nucleon mass is denoted by m_N $(N = n, p)$ whereas m_i $(i = \sigma, \omega, \rho)$ are masses assigned to the meson fields. The field tensors $R^a_{\mu\nu}$ and $\Omega_{\mu\nu}$ have the following forms

$$R^a_{\mu\nu} = \partial_\mu\rho^a_\nu - \partial_\nu\rho^a_\mu + g_{\rho N}\varepsilon_{abc}\rho^b_\mu\rho^c_\nu, \tag{6.4}$$

$$\Omega_{\mu\nu} = \partial_\mu\omega_\nu - \partial_\nu\omega_\mu. \tag{6.5}$$

The parameters that enter the Lagrangian function (6.1), which includes besides the Lagrangian of free nucleons and mesons the Lagrangian describing the interaction between nucleons and the meson

fields, are determined by fitting to the bulk properties of nuclear matter [2].

The Euler–Lagrange equations in the presence of the interactions can be written as

$$(\partial_\mu \partial^\mu + m_\sigma^2)\sigma(x) + g_3\sigma^2(x) + g_4\sigma^3(x) = g_{\sigma N}\bar{\psi}_N(x)\psi_N(x), \tag{6.6}$$

$$\partial_\nu \Omega_{\mu\nu}(x) + m_\omega^2\omega_\mu(x) + \frac{1}{6}c_3(\omega_\mu(x)\omega_\mu(x))\omega^\nu(x) = g_{\omega N}\bar{\psi}_N(x)\gamma^\mu\psi_N(x), \tag{6.7}$$

$$\partial_\nu R^a_{\mu\nu}(x) + m_\rho^2\rho^a_\mu(x) = \frac{1}{2}g_{\rho N}\bar{\psi}_N(x)\gamma^\mu\tau^a\psi_N(x), \tag{6.8}$$

$$\left[\gamma^\mu(i\partial_\mu - g_{\omega N}\omega_\mu(x) - \frac{1}{2}g_{\rho N}\gamma^\mu\tau^a\rho^a_\mu(x)) - (m_N - g_{\sigma N}\sigma(x)\right]\psi_N(x) = 0. \tag{6.9}$$

The equation (6.6) is the Klein–Gordon equation with a scalar source term and nonlinear self-interactions. The second equation (6.7) is the equation for the massive vector field with the conserved baryon current $J^\mu_b = \bar{\psi}_N\gamma^\mu\psi_N \equiv (n_b, J^a_b)$, $(\partial_\mu J^\mu_b = 0)$, its time component $J^0_b \equiv n_b = \bar{\psi}_N\gamma^0\psi_N$ is the baryon density. The equation of motion of the ρ meson field (6.8) is similar to equation (6.7). The difference is connected with the isovector character of the ρ meson field. The conserved isospin current for nucleons has the form $J^{\mu a} = 1/2\bar{\psi}_N\gamma^\mu\tau^a\psi_N$. Its 3-component can be written as $J^{\mu 3} = 1/2\bar{\psi}_N\gamma^\mu\tau^3\psi_N$ and for the τ_3 representation

$$\tau_3 = \begin{pmatrix} 1 & 0 \\ 0 & -1 \end{pmatrix}$$

the isospin density has the following form $J^0_3 = 1/2(\psi^\dagger_p\psi_p - \psi^\dagger_n\psi_n)$.

Solutions of the equations of motion can be found in the relativistic mean field approximation for which meson fields are separated into classical mean field values and quantum fluctuations which are not included in the ground state

$$\sigma(x) = \bar{\sigma}(x) + s_0 \quad \omega_\mu(x) = \bar{\omega}_\mu(x) + < w_\mu >$$
$$\rho^a_\mu(x) = \bar{\rho}^a_\mu(x) + < r_\mu > \delta^{3a}.$$

In the relativistic mean field approach the equations of motion now have the following form

$$m_\sigma^2 s_0 + g_3 s_0^2 + g_4 s_0^3 = g_{\sigma N} < \bar{\psi}_N\psi_N >, \tag{6.10}$$

$$m_\omega^2 < w_0 > + c_3 < w_0 >^3 = g_{\omega N} < \bar{\psi}_N \gamma^0 \psi_N >, \tag{6.11}$$

$$m_\omega^2 < w_k > + c_3 < w_k >^3 = g_{\omega N} < \bar{\psi}_N \gamma^k \psi_N >, \tag{6.12}$$

$$m_\rho^2 < r_0 > = \frac{1}{2} g_{\rho N} < \bar{\psi}_N \gamma^0 \tau_3 \psi_N >, \tag{6.13}$$

$$m_\rho^2 < r_k > = \frac{1}{2} g_{\rho N} < \bar{\psi}_N \gamma^k \tau_3 \psi_N > . \tag{6.14}$$

In the momentum space the Dirac equation has the following form

$$\left[\gamma^\mu (k_\mu - g_{\omega N} < w_\mu > - \frac{1}{2} g_{\rho N} \tau_3 < r_\mu >) - (m_N - g_{\sigma N} s_0) \right] \psi_N(k) = 0. \tag{6.15}$$

The system which is considered, is assumed to be the isotropic, infinite matter in its ground state. For infinite isotropic matter the space components of $< \omega_\mu >$ and $< \rho_\mu >$ vanish ($< \omega_\mu >=< \rho_\mu >= 0$ for $\mu \neq 0$). The classical mean field values can be written as $< \omega_\mu >= w_0 \delta_{\mu 0} = 0$ and $< \rho_\mu >= r_0 \delta_{\mu 0}$.

The resulting field equations for this approximation have a reduced, simpler form

$$m_\sigma^2 s_0 + g_3 s_0^2 + g_4 s_0^3 = g_{\sigma N} < \bar{\psi}_N \psi_N > \tag{6.16}$$

$$m_\omega^2 w_0 + c_3 w_0^3 = g_{\omega N} < \bar{\psi}_N \gamma^0 \psi_N > \tag{6.17}$$

$$m_\rho^2 r_0 = \frac{1}{2} g_{\rho N} < \bar{\psi}_N \gamma^0 \tau_3 \psi_N > . \tag{6.18}$$

For infinite, isotropic matter the energy eigenvalues are given by the following relation

$$e_\pm(k) = (g_{\omega N} w_0 + \frac{1}{2} g_{\rho N} r_0) \pm (k^2 + (m_N - g_{\sigma N} s_0)^2)^{1/2}, \tag{6.19}$$

where the effective nucleon mass $m_{eff,N}$ is defined as

$$m_{eff,N} = m_N - g_{\sigma N} s_0. \tag{6.20}$$

The ground state expectation values of the baryon density $< \bar{\psi}_N \gamma^0 \psi_N >$, scalar density $< \bar{\psi}_N \psi_N >$ and isospin density $< \bar{\psi}_N \gamma^0 \tau_3 \psi_N >$ are given by the following relations

$$\rho_s \equiv < \bar{\psi}_N \psi_N > = \sum_{N=n,p} \frac{1}{\pi^2} \int_0^{k_{F_N}} \frac{m_N - g_{\sigma N} s_0}{\sqrt{k^2 + (m_N - g_{\sigma N} s_0)^2}} k^2 dk, \tag{6.21}$$

$$n_b \equiv < \bar{\psi}_N \gamma^0 \psi_N > = \sum_{N=n,p} \frac{1}{\pi^2} \int_0^{k_{F_N}} k^2 dk = \sum_{N=n,p} \frac{k_{F_N}^3}{3\pi^2}, \tag{6.22}$$

$$\rho_3 \equiv < \bar{\psi}_N \gamma^0 \tau_3 \psi_N > = \frac{k_{F_p}^3}{3\pi^2} - \frac{k_{F_n}^3}{3\pi^2}, \tag{6.23}$$

where k_F – the upper limit in the momentum integrals is the Fermi momentum.

The nucleon Fermi energy $\mu_N = e(k)$ and thus the effective nucleon chemical potential can be defined as

$$\nu_N = \mu_N - g_{\omega N} w_0 + I_{3N} g_{\rho N} r_0. \tag{6.24}$$

In order to calculate the energy density and pressure of the nuclear matter the energy-momentum tensor $T_{\mu\nu}$ which is given by the relation

$$T_{\mu\nu} \equiv \frac{\partial \mathcal{L}}{\partial(\partial \mu \phi_i)} \partial^\nu \phi_i - \eta_{\mu\nu} \mathcal{L} \tag{6.25}$$

have to be used. In equation (6.25) ϕ_i denotes boson and fermion fields.

The energy density ϵ equals $< T_{00} >$ whereas the pressure P is related to the statistical average of the trace of the spatial component T_{ij} of the energy-momentum tensor. Calculations done for the considered model lead to the following explicit formula for the energy density and pressure:

$$\epsilon = \frac{1}{2} m_\omega^2 w_0^2 + \frac{3}{4} c_3 w_0^4 + \frac{1}{2} m_\rho^2 r_0^2 + U(s_0) + \epsilon_N \tag{6.26}$$

with ϵ_N given by

$$\epsilon_N = \sum_{N=n,p} \frac{2}{\pi^2} \int_0^{k_{F,N}} k^2 dk \sqrt{k^2 + (m_N - g_{\sigma N} s_0)^2}, \tag{6.27}$$

$$P = \frac{1}{2} m_\rho r_0^2 + \frac{1}{2} m_\omega w_0^2 + \frac{1}{4} c_3 w_0^4 - U(s_0) + P_N, \tag{6.28}$$

$$P_N = \sum_{N=n,p} \frac{1}{3\pi^2} \int_0^{k_{F,N}} \frac{k^4 dk}{\sqrt{(k^2 + m_N - g_{\sigma N} s_0)^2}}. \tag{6.29}$$

The obtained form of the EOS [47], [101] determines the physical state and composition of matter at high densities. In order to construct the neutron star model through the entire density span it is necessary

to add the EOS, characteristic for the inner and outer core, relevant to lower densities. Thus, a more complete and more realistic description of a neutron star requires taking into consideration not only the interior region of a neutron star, but also its remaining layers. In these calculations the composite EOS for the entire neutron star density span was constructed by joining together the equation of state of the neutron rich matter region, the Negele–Vautherin EOS [50] and Bonn [49] for the relevant density range between 10^{14} and $5 \times 10^{10}\,\mathrm{gcm}^{-3}$ and the Haensel–Pichon EOS [114] for the density region $9.6 \times 10^{10}\,\mathrm{gcm}^{-3}$ to $3.3 \times 10^{7}\,\mathrm{gcm}^{-3}$. Since the density drops steeply near the surface of a neutron star, these layers do not contribute significantly to the total mass of a neutron star. The inner neutron rich region up to density $\rho \sim 10^{13}\,\mathrm{gcm}^{-3}$ influences decisively the neutron star structure and evolution.

6.2 Model with nonlinear isoscalar-isovector interaction terms

Neutron star structure is determined by the EOS of highly asymmetric matter in β-equilibrium. This EOS contains the symmetry energy term, whose density dependence is still poorly known. The inclusion of the mixed nonlinear isoscalar-isovector couplings Λ_4, Λ_V [46], [47], [115], [116] provides the additional possibility of modifying the high density components of the symmetry energy. The presence of the $\Lambda_4\sigma^2\rho^2$ and $\Lambda_V\omega^2\rho^2$ terms in the Lagrangian function (6.1) requires the adjustment of the $g_{\rho N}$ coupling constant to keep the same value of the symmetry energy at saturation. The remaining ground state properties are left unchanged. With these two additional terms the field equations (6.16), (6.17) and (6.18) have been modified and take the following forms [47], [119]

$$m_\sigma^2 s_0 + g_3 s_0^2 + g_4 s_0^3 + 2\Lambda_4 (g_{\sigma N} g_{\rho N})^2 s_0 r_0^2 = g_{\sigma N} < \bar{\psi}_N \psi_N >, \qquad (6.30)$$

$$m_\omega^2 w_0 + c_3 w_0^3 + 2\Lambda_V (g_{\omega N} g_{\rho N})^2 w_0 r_0^2 = g_{\omega N} < \bar{\psi}_N \gamma^0 \psi_N >, \qquad (6.31)$$

$$m_\rho^2 r_0 + 2(\Lambda_4 (g_{\sigma N} g_{\rho N})^2 s_0^2 + \Lambda_V (g_{\omega N} g_{\rho N})^2 w_0^2) r_0 = \frac{1}{2} g_{\rho N} < \bar{\psi}_N \gamma^0 \tau_3 \psi_N > . \qquad (6.32)$$

The expression for the symmetry energy coefficient $E_{sym}(n_0)$ is now given by the equation

$$E_{sym}(n_0) = \frac{1}{8}\frac{n_0}{m_\rho^2/g_{\rho N}^2 + 2(\Lambda_V(g_{\rho N}g_{\omega N})^2 w_0^2 + \Lambda_4(g_{\sigma N}g_{\rho N})^2 s_0^2)} + \frac{k_F^2}{6\sqrt{k_F^2+m_0^2}}, \quad (6.33)$$

where where k_0 and m_0 are the Fermi momentum and nucleon effective mass of symmetric nuclear matter at saturation. The first term in this equation coming from the explicit coupling between the nucleon isospin and the ρ meson whereas the second quantity is the relativistic kinetic energy contribution. The influence of the nonlinear couplings can also be considered in terms of effective ω and ρ meson masses [117] which can be defined by the following relation

$$m_{eff,\omega}^2 = m_\omega^2 + 2\Lambda_V(g_{\rho N}g_{\omega N})^2 r_0^2, \quad (6.34)$$

$$m_{eff,\rho}^2 = m_\rho^2 + 2\left(\Lambda_V(g_{\rho N}g_{\omega N})^2 w_0^2 + \Lambda_4(g_{\sigma N}g_{\rho N})^2 s_0^2\right). \quad (6.35)$$

In this interpretation this is the ρ meson mass modification that influences the density dependence of the symmetry energy. The presence of the nonlinear couplings Λ_V and Λ_4 between the isoscalar and isovector mesons also adds extra terms to the total pressure of the system.

6.3 Model with δ meson

Further extension of the isovector channel has been done by the inclusion of the isovector-scalar meson δ [118], [119]. The contributions coming from the presence of the δ meson field should be significant in the case of dense matter with high asymmetry.

This meson field has been included in a minimal type and the Lagrangian function has the following form

$$\mathcal{L}_\delta = \frac{1}{2}(\partial_\mu\delta^a\partial^\mu\delta^a - m_\delta^2\delta^a\delta^a) + I_{3N}g_{\delta N}\delta^a\tau^a\bar{\psi}_N\psi_N. \quad (6.36)$$

The nonvanishing component of the δ meson field is δ^3 ($\delta^a = \bar{\delta}^a + d_0\delta^{3a}$) and the equation of motion has the following form

$$m_\delta^2 d_0 = \frac{1}{\pi^2}\sum_{N=n,p} g_{\delta N}I_{3N}\int_0^{k_{F_N}} \frac{m_{effN}}{\sqrt{k^2+m_{effN}^2}}k^2dk. \quad (6.37)$$

A very important aspect of the inclusion of δ meson is the nucleon mass splitting. The effective neutron and proton mass is given by the relation

$$m_{effN} = m_N - g_{\sigma N} s_0 - I_{3N} g_{\delta N} d_0. \tag{6.38}$$

The δ meson contributes to the energy density and pressure of the considered model by adding the following terms to the energy density of the uniform nuclear matter

$$\epsilon_\delta = \frac{1}{2} m_\delta^2 d_0^2. \tag{6.39}$$

The isovector sector now includes ρ and δ meson fields. The presence of the δ meson and its contribution to the symmetry energy E_{sym} imposes the constrains on $g_{\rho N}$ and $g_{\delta N}$ coupling constants. The explicit expression for the symmetry energy $E_{sym}(n_0)$ can be expressed by [118], [120]

$$E_{sym}(n_0) = \frac{1}{6}\frac{k_0^2}{\sqrt{k_0^2+m_0^2}} + \frac{1}{8} g_{\rho N}^2 \frac{n_0}{m_\rho^2} - g_{\delta N}^2 \frac{n_0 m_0^2}{2\sqrt{k_0^2+m_0^2}(m_\delta^2 + g_{\delta N}^2 A)}, \tag{6.40}$$

where A is specified by

$$A = \frac{6}{\pi^2 \sqrt{k_0^2+m_0^2}} \left[m_0^2 (k_0^2 - ln\left(\frac{k_0 + \sqrt{k_0^2+m_0^2}}{m_0}\right)) + \frac{k_0^3}{3} \right]. \tag{6.41}$$

The parameters $g_{\rho N}$ and $g_{\delta N}$ in the equation (6.40) are adjusted to get the experimental value of the symmetry energy $E_{sym}(n_0)$ coefficient which is equal 32 ± 4 MeV. The parameters $g_{\rho N}$ and $g_{\delta N}$ are correlated. Kubis and Kutschera in the paper [120] considered a range of values of the parameter $g_{\delta N}$ corresponding to the Bonn potentials A, B and C [20]. For the analysis performed in this paper the parameter $g_{\delta N} = 8.0$ which corresponds to the Bonn potential C has been chosen.

6.4 Model with nonzero temperature

The generalization of the theory to the finite temperature case requires the definition of a thermodynamic potential Ω and the grand partition function Z. The thermodynamic potential of a system at specified chemical potential μ, volume V and temperature T is given by [112]

$$\Omega(\mu, V, T) = -k_B T \ln Z, \tag{6.42}$$

where Z is the grand partition function Z which in the limit of relativistic mean field approach is given by the relation ($\hbar = c = 1$)

$$\begin{aligned} lnZ &= \frac{1}{k_B T} V(\frac{1}{2} m_\sigma^2 s_0^2 + \frac{1}{3} s_0^3 + \frac{1}{4} s_0^4 + \frac{1}{2} m_\delta^2 d_0^2 \\ &- \frac{1}{2} m_\omega^2 w_0^2 - \frac{1}{4} c_3 w_0^4 - \frac{1}{2} m_\rho^2 r_0^2 - \Lambda_4 (g_\sigma g_\rho)^2 s_0^2 r_0^2 - \Lambda_V (g_\omega g_\rho)^2 w_0^2 r_0^2) \\ &+ V \sum_N \left(\int_0^\infty \frac{d^3 k}{(2\pi)^3} ln \left(1 + e^{-(E_N - \nu_N)/k_B T} \right) + \right. \\ &+ \left. \int_0^\infty \frac{d^3 k}{(2\pi)^3} ln \left(1 + e^{-(E_N + \nu_N)/k_B T} \right) \right), \end{aligned} \tag{6.43}$$

where $E_N = \sqrt{k^2 + m_{eff,N}^2}$ is the nucleon energy and ν_N denotes the nucleon effective chemical potential given by equation (6.24). Contributions from thermal excitation of real mesons can be neglected. Having obtained the partition function Z and using the standard thermodynamic relations the pressure, baryon number density, isospin density, energy density and the entropy density can be calculated. The thermodynamic functions are obtained by integrating over the momentum space taking the statistical weight $g_s = 2$.

The pressure equals $P = k_B T / V \ln Z$ and the energy density is given by

$$\begin{aligned} \varepsilon &= \frac{1}{2} m_\sigma s_0^2 + \frac{1}{3} s_0^3 + \frac{1}{4} s_0^4 + \frac{1}{2} m_\delta^2 d_0^2 \\ &+ \frac{1}{2} m_\omega^2 w_0^2 + \frac{1}{4} c_3 w_0^4 + \frac{1}{2} m_\rho^2 r_0^2 + \Lambda_s (g_\sigma g_\rho)^2 s_0^2 r_0^2 + \Lambda_V (g_\omega g_\rho)^2 w_0^2 r_0^2 \\ &+ \sum_N \left\{ \int \frac{d^3 k}{(2\pi)^3} \ln \left(1 + e^{(-E_N - \nu_N)/k_B T} \right) + \ln \left(1 + e^{(-E_N + \nu_N)/k_B T} \right) \right\}. \end{aligned} \tag{6.44}$$

The entropy density equals $s = (\varepsilon + P - \sum_N \mu_N n_N)/k_B T$. The meson fields can be obtained by minimization of the thermodynamic potential, which leads to the equations [121]

$$\begin{aligned} & m_\sigma^2 s_0 + g_3 s_0^2 + g_4 s_0^3 + 2\Lambda_4 (g_{\sigma N} g_{\rho N})^2 s_0 r_0^2 = \\ & = \sum_{N=n,p} \left(\int_0^\infty \frac{d^3 k}{(2\pi)^3} \frac{m_{eff,N}}{E_N} \frac{1}{(1 + e^{-(E_N - \nu_N)/k_B T})} + \right. \\ & + \left. \int_0^\infty \frac{d^3 k}{(2\pi)^3} \frac{m_{eff,N}}{E_N} \frac{1}{(1 + e^{-(E_N + \nu_N)/k_B T})} \right), \end{aligned} \tag{6.45}$$

$$m_\omega^2 w_0 + c_3 w_0^3 + 2\Lambda_V (g_{\omega N} g_{\rho N})^2 w_0 r_0^2 = \sum_{N=n,p} g_{\omega N} n_{B_N}, \tag{6.46}$$

$$m_\rho^2 r_0 + 2(\Lambda_4 (g_{\sigma N} g_{\rho N})^2 s_0^2 + \Lambda_V (g_{\omega N} g_{\rho N})^2 w_0^2) r_0 = \sum_{N=n,p} g_{\rho N} I_{3N} n_{B_N}, \tag{6.47}$$

where

$$n_{B_N} = \frac{2J_N + 1}{2\pi^2} \int_0^\infty k^2 dk (f(\epsilon_N) - \bar{f}(\epsilon_N)), \tag{6.48}$$

J_N and I_{3N} are the spin and isospin projection of nucleons. The functions $f(\epsilon_N)$ and $\bar{f}(\epsilon_N)$ are the Fermi–Dirac distribution functions for particles and anti-particles, respectively. They are given by

$$f(\epsilon_N) = \frac{1}{1 + \exp{(\epsilon_N - \nu_N)/k_B T}}, \tag{6.49}$$

$$\bar{f}(\epsilon_N) = \frac{1}{1 + \exp{(\epsilon_N + \nu_N)/k_B T}}. \tag{6.50}$$

6.5 Leptons

Neutron star matter is constrained by the charge neutrality and β-equilibrium. Thus realistic neutron star models describe electrically neutral high density matter being in β-equilibrium. These two conditions imply the presence of electrons. After electron chemical potential μ_e reaches the value equal to the muon mass, muons start to appear. Equilibrium with respect to the reaction

$$e^- \leftrightarrow \mu^- + \nu_e + \bar{\nu}_\mu \tag{6.51}$$

is assured when

$$\mu_\mu = \mu_e + \mu_{\nu_e} + \mu_{\bar{\nu}_\mu}. \tag{6.52}$$

The appearance of muons in neutron star matter reduces number of electrons and affects also the proton fraction. Neutrinos have to be considered due to their very important role during the supernova explosion and in the very early stage of proto-neutron star evolution. In these cases the assumption that the matter is opaque to neutrinos can be made, neutrinos are trapped and the lepton fraction is kept constant. Neutron star matter is transparent to neutrinos, thus setting $\mu_{\nu_e} = \mu_{\nu_\mu} = 0$ the condition (6.52) reduces to

$$\mu_\mu = \mu_e. \tag{6.53}$$

The presence of leptons can be expressed by adding the Lagrangian of free leptons $\mathcal{L}_L$ to the Lagrangian function (6.1)

$$\mathcal{L}_L = \sum_{f=e,\mu} \bar{\psi}_{Lf} i\gamma^\mu \partial_\mu \psi_{Lf} + \sum_{f=e,\mu} \bar{\psi}_{Rf} i\gamma^\mu \partial_\mu \psi_{Rf} - \sum_{f=e,\mu} g_{Hf} \bar{\psi}_{Lf} H \psi_{Rf}, \tag{6.54}$$

where

$$H = \frac{1}{\sqrt{2}} \begin{pmatrix} 0 \\ v \end{pmatrix}$$

and for the Higgs vacuum expectation value v the following condition is satisfied $v^2 = 1/\sqrt{2}\, G_F \simeq (250\,\mathrm{GeV})^2$. In the case of neutron star matter only two lepton families have been considered. The set of doublets and singlets is given by

$$\psi_{Lf} =: \left\{ \begin{pmatrix} \nu_e \\ e^- \end{pmatrix}_L, \begin{pmatrix} \nu_\mu \\ \mu^- \end{pmatrix}_L \right\}, \; \psi_{Rf} =: \left\{ e_R^-, \mu_R^- \right\}. \tag{6.55}$$

Introducing the fields $e = e_L + e_R$ and $\mu = \mu_L + \mu_R$ the Lagrangian (6.54) takes the form

$$\begin{aligned} \mathcal{L}_L = \bar{e}(i\gamma^\mu)\partial_\mu e \;\; &- \;\; m_e \bar{e} e + \bar{\mu}(i\gamma^\mu)\partial_\mu \mu - m_\mu \bar{\mu}\mu + \\ &+ \;\; \bar{\nu}_{eL}(i\gamma^\mu)\partial_\mu \nu_{eL} + \bar{\nu}_{\mu L}(i\gamma^\mu)\partial_\mu \nu_{\mu L}, \end{aligned} \tag{6.56}$$

where the fermion masses (electrons and muons) are given by $m_f = g_{Hf} v/\sqrt{2}$, neutrinos are considered to be massless ($m_\nu = 0$).

The characteristic of a neutrino gas has to be given for two limiting cases and for both of them neutrinos are consider to be massless particles ($m_\nu = 0$). The first one takes into account neutrinos trapped in the neutron star matter, their chemical potential $\mu_\nu \neq 0$, whereas the second examines the influence of neutrinos with zero chemical potential $\mu_\nu = 0$. In the case of cold neutron star neutrinos are neglected since they leak out from the star, whose energy diminishes at the same time.

Chapter 7

Strange nuclear matter

The analysis of the experimental data concerning the binding energies of Λ's bound in single particle orbitals in hypernuclei over an extensive range of mass numbers makes it possible to determine the potential depth of a single Λ in nuclear matter at the value of

$$U_{\Lambda}^{(N)} \simeq 27 - 30\,\mathrm{MeV} \tag{7.1}$$

which corresponds to $\sim 1/2$ of the nucleon well depth $U_N^{(N)}$. Calculations done within the Skyrme–Hartree–Fock [122] approach as well as those performed with the use of relativistic mean field models [123, 124, 125, 126, 127, 128] satisfactorily reproduce the single particle energy for various hypernuclei. As an example the result of calculations within the relativistic mean field model for hypernucleus ${}^{17}_{\Lambda}\mathrm{O}$ is presented in Fig. 7.1 [129]. In this figure the Coulomb, Λ and nucleon potentials are presented together with the single particle levels. A very characteristic feature of this figure is the location of the 1p states of the Λ which are very close to each other. This fact explains the weak spin-orbit force of the Λ-nucleon interaction [122]. There is still considerable uncertainty about the experimental status of Σ-nucleus potential. The calculations of Σ hypernuclei have been based on analysis of Σ^- atomic data. Phenomenological analysis of level shifts and widths in Σ^- atoms made by Batty et al. [130, 131] indicates that the Σ potential is attractive only at the nuclear surface, becoming repulsive for increasing density. The small attractive component of this potential is not sufficient to form bound Σ-hypernuclei. Balberg et al. in their paper [132] show that the system which includes Σ, Λ hyperons and nucleons will be unstable with respect to strong reactions $\Sigma + N \rightarrow \Lambda + N$, $\Sigma + \Sigma \rightarrow \Lambda + \Lambda$, $\Sigma + \Lambda \rightarrow \Xi + N$, $\Sigma + \Xi \rightarrow \Lambda + \Xi$ [133]. In order to study hyperon

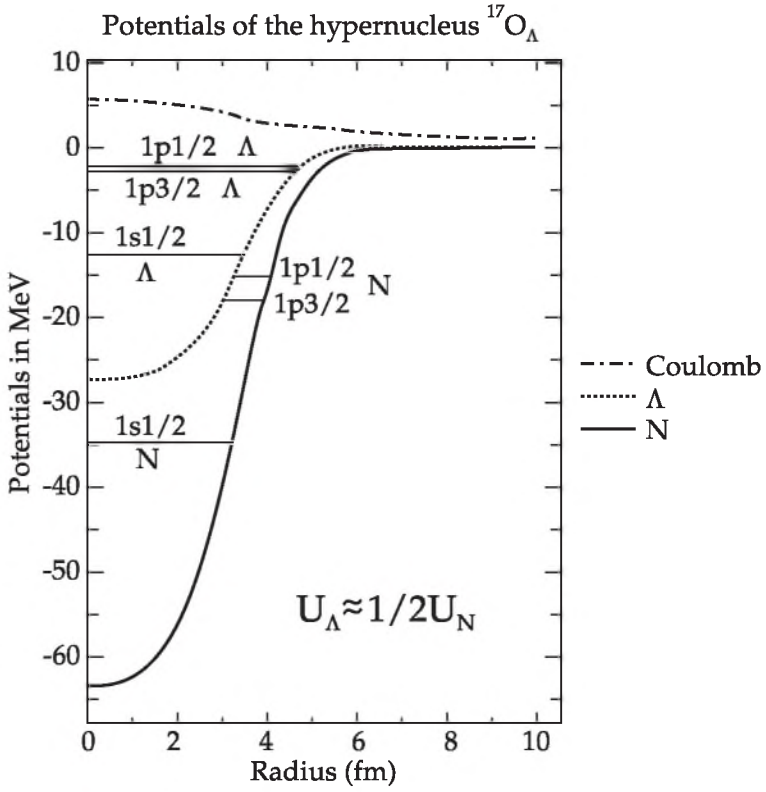

Figure 7.1: The potentials and the single particle levels for the hypernucleus ${}^{17}_{\Lambda}$O (Taken from [129])

rich neutron star matter, the knowledge of the multi-strange system is necessary. Data on ΛΛ hypernuclei are scarce. Observation of double-strange hypernuclei ΛΛ provide information about the ΛΛ interaction. Several events have been identified which indicate an attractive ΛΛ interaction. The analysis of the data allows one to estimate the binding energies of ${}^{6}_{\Lambda\Lambda}$He, ${}^{10}_{\Lambda\Lambda}$Be and ${}^{13}_{\Lambda\Lambda}$B. The experimental data concerning the double-Λ hypernuclei gives information on the sum of the binding energy of the two Λ hyperons $B_{\Lambda\Lambda}$ and the ΛΛ interaction energy $\Delta B_{\Lambda\Lambda}$. These two quantities can be defined as

$$\begin{aligned} B_{\Lambda\Lambda}({}^{A}_{\Lambda\Lambda}Z) &= B_{\Lambda}({}^{A}_{\Lambda\Lambda}Z) + B_{\Lambda}({}^{A-1}_{\Lambda}Z), \\ \Delta B_{\Lambda\Lambda}({}^{A}_{\Lambda\Lambda}Z) &= B_{\Lambda}({}^{A}_{\Lambda\Lambda}Z) - B_{\Lambda}({}^{A-1}_{\Lambda}Z). \end{aligned} \tag{7.2}$$

Table 7.1 collects experimental values of the two above mentioned observables [136, 137, 138, 139]. The obtained values of $\Delta B_{\Lambda\Lambda}$ indicate

Table 7.1: The value of $\Delta B_{\Lambda\Lambda}$ and $B_{\Lambda\Lambda}$ of the double Λ-hypernuclei (Taken from [129])

Hypernucleus	$B_{\Lambda\Lambda}[MeV]$	$\Delta B_{\Lambda\Lambda}$[MeV]
${}^{6}_{\Lambda\Lambda}He$	10.9 ± 0.6	4.7 ± 0.6
${}^{10}_{\Lambda\Lambda}Be$	17.7 ± 0.4	4.3 ± 0.4
${}^{13}_{\Lambda\Lambda}B$	27.5 ± 0.7	4.8 ± 0.7

that the ΛΛ interaction is attractive and rather strong. For comparison the value of ΔB_{NN} equals 6–7 MeV. Following the estimation made by Schaffner et al.[134] it is possible to determine approximately the ratio of the Λ well depth in Λ matter and nucleon well depth in nuclear matter

$$\frac{U_{\Lambda}^{(\Lambda)}}{U_{N}^{(N)}} \approx \frac{1}{4}. \tag{7.3}$$

For $U_N^N \simeq 80$ MeV the estimated value of U_Λ^Λ potential is $\simeq 20$ MeV.

However, recent data analysis of double hypernucleus ${}^{6}_{\Lambda\Lambda}$He done by Takahashi et al. [135] gives the following value of the ΛΛ interaction energy $\Delta B_{\Lambda\Lambda} = 1.01 \pm 0.20^{+0.18}_{-0.11}$ MeV which indicates that the interaction is much weaker. The potential well depth evaluated for this data has the value $U_\Lambda^{(\Lambda)} \simeq 5$ MeV. Using the meson exchange potentials for hyperon-hyperon interactions from Nijmegen Model D Schaffner et al. [134] made a rough estimate:

$$U_{\Xi}^{\Xi} \approx U_{\Lambda}^{\Xi} \approx 2U_{\Xi}^{\Lambda} \approx 2U_{\Lambda}^{\Lambda}. \tag{7.4}$$

A theoretical description of strange hadronic matter requires the extension of the relativistic mean field model by the inclusion of all baryons of the lowest SU(3) baryon octet. In order to describe the strongly attractive ΛΛ interaction two additional meson fields, the scalar meson $f_0(975)$ denoted as σ^* and the vector meson $\phi(1020)$ have to be introduced.

The Lagrangian function for the system can be written as a sum of a baryonic part including the full octet of baryons together with baryon-meson interaction terms, a mesonic part containing additional interactions between mesons which mathematically express themselves

as supplementary, nonlinear terms in the Lagrangian function, and a free leptonic part

$$\mathcal{L} = \mathcal{L}_{BM} + \mathcal{L}_M + \mathcal{L}_L. \tag{7.5}$$

$\mathcal{L}_{BM}$ represents the Lagrangian density of interacting baryons and has the following form

$$\mathcal{L}_{BM} = \sum_B \bar{\psi}_B i\gamma^\mu D_\mu \psi_B - \sum_B m_{eff,B}\overline{\psi}_B\psi_B, \tag{7.6}$$

where the spinor $\Psi_B^T = (\psi_N, \psi_\Lambda, \psi_\Sigma, \psi_\Xi)$ is composed of the following isomultiplets [2]:

$$\Psi_N = \begin{pmatrix}\psi_p\\ \psi_n\end{pmatrix}, \qquad \Psi_\Lambda = \psi_\Lambda,$$

$$\Psi_\Sigma = \begin{pmatrix}\psi_{\Sigma^+}\\ \psi_{\Sigma^0}\\ \psi_{\Sigma^-}\end{pmatrix}, \quad \Psi_\Xi = \begin{pmatrix}\psi_{\Xi^0}\\ \psi_{\Xi^-}\end{pmatrix}.$$

D_μ being the covariant derivative is defined as

$$D_\mu = \partial_\mu + ig_{\omega B}\omega_\mu + ig_{\phi B}\phi_\mu + ig_{\rho B}I_{3B}\tau^a\rho_\mu^a. \tag{7.7}$$

The meson sector of the Lagrangian (6.1) has to be supplemented by

$$\mathcal{L}_{\mathcal{M}} = \frac{1}{2}(\partial^\mu\sigma^*\partial_\mu\sigma^* - m_{\sigma^*}^2\sigma^{*2}) - \frac{1}{4}\phi_{\mu\nu}\phi_{\mu\nu} + \frac{1}{2}m_\phi^2\phi_\mu\phi^\mu, \tag{7.8}$$

where the field tensor is given by $\phi_{\mu\nu} = \partial_\mu\phi_\nu - \partial_\nu\phi_\mu$.
When the two additional mesons are included the field equations at the mean field level are given by:

$$m_\sigma^2 s_0 + g_3 s_0^2 + g_4 s_0^2 = \sum_B g_{\sigma B} m_{eff,B}^2 S(m_{eff,B}, k_{F,B}), \tag{7.9}$$

$$m_\omega^2 w_0 + c_3 w_0^3 = \sum_B g_{\omega B} n_B, \tag{7.10}$$

$$m_\rho^2 r_0 = \sum_B g_{\rho B} I_{3B} n_B, \tag{7.11}$$

$$m_\delta^2 d_0^3 = \sum_B g_{\delta B} I_{3B} S(m_{eff,B}, k_{F,B}), \tag{7.12}$$

$$m_{\sigma^*}^2 s_0^* = \sum_B g_{\sigma^* B} m_{eff,B}^2 S(m_{eff,B}), \tag{7.13}$$

$$m_\phi^2 f_0 = \sum_B g_{\phi B} n_B, \tag{7.14}$$

where s_0^* and f_0 are the classical mean field values of the field σ^* and ϕ_μ.

The function $S(m_{eff,B}, k_{F,B})$ is expressed with the use of an integral

$$S(m_{eff,B}, k_{F,B}) = \frac{2J_B + 1}{2\pi^2} \int_0^{k_{FB}} \frac{m_{eff,B}}{\sqrt{k^2 + m_{eff,B}}} k^2 dk, \tag{7.15}$$

where J_B and I_{3B} are the spin and isospin projection of baryon B, $k_{F,B}$ is the Fermi momentum of species B, n_B denotes the baryon number density given by equation (5.3).

The presence of the σ^* and ϕ meson fields provides new potential terms to the Dirac equation (6.15) which now takes the form

$$(i\gamma^\mu \partial_\mu - m_{eff,B} - g_{\omega B}\gamma^0 \omega_0 - g_{\rho B} I_{3B} \gamma^0 \tau^3 r_0 - g_{\phi B}\gamma^0 f_0)\psi_B = 0 \tag{7.16}$$

with $m_{eff,B}$ being the effective baryon mass generated by the baryon and scalar fields interaction and defined as

$$m_{eff,B} = m_B - (g_{\sigma B} s_0 + I_{3B} g_\delta d_0 + g_{\sigma^* B} s_0^*). \tag{7.17}$$

In the case of finite nuclei the performed calculations in the relativistic mean field approach leads to results comparable with those obtained in the Skyrme–Hartree–Fock model. In Fig. 7.2 the experimental values of single particle energy for different hypernuclei are presented. For comparison the results obtained for the relativistic mean field and Skyrme–Hartree–Fock model are included. Neglecting the spin-orbit splitting the particular shells are labelled by s-shell, p-shell... All levels converge at a point which crosses the y-axis at the energy of about $\sim 27 - 28$ MeV. Bulk matter corresponds to this point and the Λ potential depth in nuclear matter is of about 28 MeV.

The scalar $g_{\sigma B}$ and vector $g_{\omega B}$ coupling constants are strongly correlated by the potentials felt by a single Λ, Σ and Ξ in saturated nuclear matter ($\rho_0 \sim 2.5\ 10^{14}$ gcm^{-3}). The general form of this potential is given by the following relation:

$$U_Y^N = g_{\sigma Y} s_0 - g_{\omega Y} w_0, \tag{7.18}$$

where Y stands for Λ, Σ and Ξ hyperons respectively. In the scalar sector the scalar coupling of the Λ, Σ and Ξ hyperons requires constraining in order to reproduce the estimated values of the potential

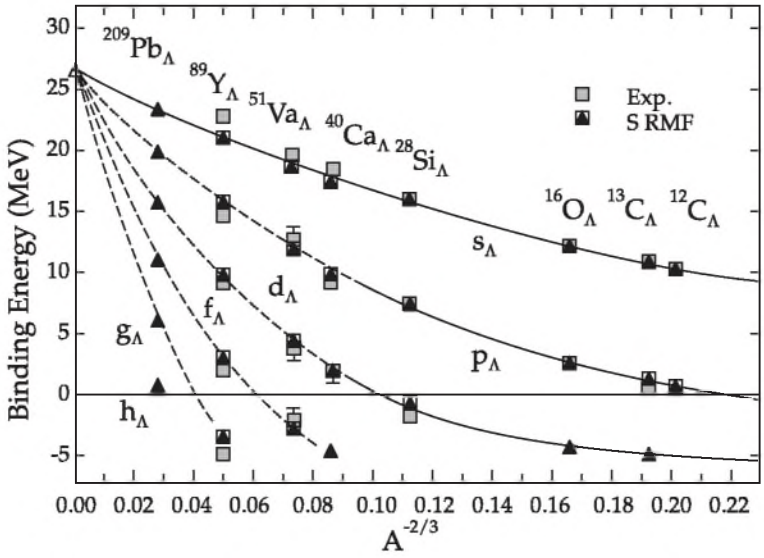

Figure 7.2: The single particle energy of several hypernuclei in comparison with the relativistic mean field calculations and with the results obtained in the Skyrme–Hartree–Fock model (Taken from [129])

felt by a single Λ and a single Ξ in saturated nuclear matter

$$\begin{aligned} U_\Lambda^{(N)}(\rho_0) &= g_{\sigma\Lambda}s_0(\rho_0) - g_{\omega\Lambda}w_0(\rho_0) \simeq -(27-30)\,\mathrm{MeV} \quad (7.19)\\ U_\Sigma^{(N)}(\rho_0) &= g_{\sigma\Sigma}s_0(\rho_0) - g_{\omega\Sigma}w_0(\rho_0) \simeq +30\,\mathrm{MeV} \\ U_\Xi^{(N)}(\rho_0) &= g_{\sigma\Xi}s_0(\rho_0) - g_{\omega\Xi}w_0(\rho_0) \simeq -(18-20)\,\mathrm{MeV}. \end{aligned}$$

Assuming the SU(6) symmetry for the vector coupling constants

$$\begin{aligned} \frac{1}{2}g_{\omega\Lambda} = \frac{1}{2}g_{\omega\Sigma} = g_{\omega\Xi} = \frac{1}{3}g_{\omega N} \quad (7.20)\\ \frac{1}{2}g_{\rho\Sigma} = g_{\rho\Xi} = g_{\rho N};\, g_{\rho\Lambda} = 0 \\ 2g_{\phi\Lambda} = 2g_{\phi\Sigma} = g_{\phi\Xi} = \frac{2\sqrt{2}}{3}g_{\omega N} \end{aligned}$$

and determining the scalar coupling constants from the potential depths, the hyperon-meson couplings can be fixed.

The strength of hyperon coupling to strange meson σ^* is restricted through the following relation [140]

$$U_\Xi^{(\Xi)} \approx U_\Lambda^{(\Xi)} \approx 2U_\Xi^{(\Lambda)} \approx 2U_\Lambda^{(\Lambda)}. \quad (7.21)$$

which together with the estimated value of hyperon potential depths in hyperon matter provides effective constraints on scalar coupling constants to the σ^* meson [141].

7.1 The effective field theoretical model

The relativistic mean field models have been very successful in describing properties of finite nuclei with relatively high precision. Extrapolation of the relativistic mean field models to the high density regime predicts stiffer equation of state compared to the results of the Dirac–Brueckner–Hartree–Fock theory. The chiral effective Lagrangian proposed by Furnstahl, Serot and Tang (FST) [36, 37] constructed on the basis of the effective field theory and density functional theory for hadrons gave in the result the extension of the standard relativistic mean field theory and introduced additional non-linear scalar-vector and vector-vector meson self-interactions. This Lagrangian in general includes all non-renormalizable couplings consistent with the underlying symmetries of QCD. Applying the dimensional analysis of Georgi and Manohar [38, 39] and the concept of naturalness one can expand the nonlinear Lagrangian and organize it in increasing powers of the fields and their derivatives and truncate at a given level of accuracy [25]. From the paper [142, 143, 144] one can see that the effective relativistic mean field models containing terms up to the quartic order give satisfactory results when applied to study the properties of finite nuclei. Thus if the truncated Lagrangian includes terms up to the fourth order it can be written in the following form

$$\begin{aligned}
\mathcal{L} &= \sum_B \bar{\psi}_B(i\gamma^\mu D_\mu - m_B + g_{\sigma B}\sigma + g_{\sigma^* B}\sigma^*)\psi_B + \qquad (7.22)\\
&+ \frac{1}{2}\partial_\mu\sigma\partial^\mu\sigma - m_\sigma^2\sigma^2\left(\frac{1}{2} + \frac{\kappa_3}{3!}\frac{g_{\sigma B}\sigma}{M} + \frac{\kappa_4}{4!}\frac{g_{\sigma B}^2\sigma^2}{M^2}\right) + \frac{1}{2}\partial_\mu\sigma^*\partial^\mu\sigma^* -\\
&- \frac{1}{2}m_{\sigma^*}^2\sigma^{*2} + \frac{1}{2}m_\phi^2\phi_\mu\phi^\mu - \frac{1}{4}\phi_{\mu\nu}\phi^{\mu\nu} - \frac{1}{4}\Omega_{\mu\nu}\Omega^{\mu\nu} - \frac{1}{4}R_{\mu\nu}^a R^{a\mu\nu} +\\
&+ \frac{1}{2}\left(1 + \eta_1\frac{g_{\sigma B}\sigma}{M} + \frac{\eta_2}{2}\frac{g_{\sigma B}^2\sigma^2}{M^2}\right)m_\omega^2\omega_\mu\omega^\mu +\\
&+ \left(1 + \eta_\rho\frac{g_{\sigma B}\sigma}{M}\right)\frac{1}{2}m_\rho^2\rho_\mu^a\rho^{a\mu} + \frac{1}{24}\zeta_0 g_{\omega B}^2(\omega_\mu\omega^\mu)^2, \qquad (7.23)
\end{aligned}$$

where $\Psi_B^T = (\psi_N, \psi_\Lambda, \psi_\Sigma, \psi_\Xi)$. The covariant derivative D_μ is given by (7.7), whereas $R^a_{\mu\nu}$, $\Omega_{\mu\nu}$ and $\phi_{\mu\nu}$ are the field tensors. m_B denotes baryon mass whereas m_i $(i = \sigma, \omega, \rho, \sigma^*, \phi)$ are masses assigned to the meson fields, M is the nucleon mass. Due to the fact that the expectation value of the ρ meson field is an order of magnitude smaller than that of ω meson field, the Lagrangian function (6.1) does not include the quartic ρ meson term. In addition, as this paper deals with the problem of infinite nuclear matter the terms in the Lagrangian function in the paper [36] involving tensor couplings and meson field gradients have been excluded.

The derived equations of motion constitute a set of coupled equations which have been solved in the mean field approximation. Derivative terms are neglected and only time-like components of the vector mesons will survive if one assumes homogenous and isotropic infinite matter. The field equations derived from the Lagrange function at the mean field level are [145]

$$m_\sigma^2 \left(s_0 + \frac{g_{\sigma B}\kappa_3}{2M} s_0^2 + \frac{g_{\sigma B}^2 \kappa_4}{6M^2} s_0^3 \right) - \frac{1}{2} m_\omega^2 \left(\eta_1 \frac{g_{\sigma B}}{M} + \eta_2 \frac{g_{\sigma B}^2}{M^2} s_0 \right) w_0^2 -$$
$$- \frac{1}{2} m_\rho^2 \eta_\rho \frac{g_\sigma}{M} r_0^2 = \sum_B g_{\sigma B} m_{eff,B}^2 S(m_{eff,B}), \tag{7.24}$$

$$m_\omega^2 \left(1 + \frac{\eta_1 g_\sigma}{M} s_0 + \frac{\eta_2 g_\sigma^2}{2M^2} s_0^2 \right) w_0 + \frac{1}{6} \zeta_0 g_{\omega B}^2 w_0^3 = \sum_B g_{\omega B} n_B, \tag{7.25}$$

$$m_\rho^2 \left(1 + \frac{g_{\sigma B}\eta_\rho}{M} s_0 \right) r_0 = \sum_B g_{\rho B} I_{3B} n_B, \tag{7.26}$$

$$m_{\sigma *}^2 s_0^* = \sum_B g_{\sigma^* B} m_{eff,B}^2 S(m_{eff,B}), \tag{7.27}$$

$$m_\phi^2 f_0 = \sum_B g_{\phi B} n_B. \tag{7.28}$$

The function $S(m_{eff,B})$ is expressed with the use of integral (7.15) whereas n_B is given by equation (5.3).

Chapter 8

Properties of nuclear matter

8.1 Infinite symmetric nuclear matter

For symmetric nuclear matter there is no isospin dependence, and thus no contributions coming from the ρ meson field. The analysis has been performed for the standard nonlinear $\sigma - \omega$ model, for which only isoscalar non-linear self-interaction terms are present. The interacting Lagrangian includes the Yukawa couplings of the nucleon field to isoscalar scalar σ and vector ω meson fields. In addition there are nonlinear scalar self-interaction terms and the quartic meson coupling term. The last one is absent in the case of NL3 [41] parameterization.

In the FST model there is also the mixed isoscalar scalar-vector $\sigma - \omega$ coupling term (the parameter $\eta_1 \neq 0$ and $\eta_2 \neq 0$).

The saturation properties of nuclear matter related to the selected parameter sets are shown in Table 8.1. These standard nuclear matter properties are: the saturation density n_0, binding energy E_{b0} at saturation density, compression modulus K_0 and the value of the effective nucleon mass m_{effN}/m_N at the saturation density.

The presented parameterizations (Table 8.2 and 8.3) have been used to calculate binding energies for symmetric nuclear matter as a function of baryon density. As the Dirac–Brueckner–Hartree–Fock (DBHF) approach provides a very good description of nuclear matter properties it is interesting to relate the obtained results with those calculated within the DBHF approach. For comparison the equation of state obtained with the use of Dirac–Brueckner T-matrix calculations has been chosen [146, 147].

Table 8.1: Saturation properties of nuclear matter

Parameter set	$n_0(fm^{-3})$	E_b(MeV)	K_0(MeV)	J(MeV)	m_{effN}/m_N
G2	0.153	-16.07	215.0	36.4	0.664
TM1*	0.145	-16.30	281.1	36.9	0.634
TM1	0.145	-16.30	281.1	36.9	0.634
NL3	0.148	-16.24	271.5	37.4	0.595

Table 8.2: TM1 parameter set and its extensions

Parameter set	m_σ(MeV)	$g_{\sigma N}$	$g_{\omega N}$	$g_{\rho N}$
TM1	511.198	10.029	12.614	9.264
TM1+δ	511.198	10.029	12.614	14.752
TM1+Λ_V	511.198	10.029	12.614	10.029
TM1+Λ_4	511.198	10.029	12.614	11.442

Parameter set	$g_{\delta N}$	c_3	Λ_V	Λ_4
TM1	0.0	71.308	0.0	0.0
TM1+δ	8.0	71.308	0.0	0.0
TM1+Λ_V	0.0	71.308	0.01	0.0
TM1+Λ_4	0.0	71.308	0.0	0.01

Table 8.3: Parameter sets of the effective field theoretical models

Parameter set	m_σ(MeV)	$g_{\sigma N}$	$g_{\omega N}$	$g_{\rho N}$	c_3
G2	520.255	10.496	12.762	9.484	71.015
TM1*	511.198	11.222	14.979	10.003	134.624
Parameter set	κ_3	κ_4	η_1	η_2	η_ρ
G2	3.247	0.632	0.650	0.110	0.390
TM1*	2.513	8.970	1.1	0.1	0.45

Table 8.4: Strange scalar sector parameters

Parameter set	Y–Y coupling	$g_{\sigma\Lambda}$	$g_{\sigma\Xi}$	$g_{\sigma^*\Lambda}$	$g_{\sigma^*\Xi}$
TM1	weak	6.227	3.201	4.072	11.517
	strong	6.227	3.201	8.138	12.602
TM1*	weak	6.971	3.583	5.526	13.449
	strong	6.971	3.583	9.158	14.394
G2	weak	6.410	3.337	3.890	11.644
	strong	6.410	3.337	8.025	12.460

Table 8.5: Strange scalar sector parameters obtained for different values of the potential $U_\Lambda^{(N)}$ felt by a single Λ in saturated nuclear matter. Calculations have been done for $U_\Lambda^{(N)}$= −27, −28, −30 MeV

$U_\Lambda^{(N)}$	−27 MeV	−28 MeV	−30 MeV
$g_{\sigma\Lambda}$	6.872	6.905	6.971
$g_{\sigma^*\Lambda}$	9.203	9.158	9.054

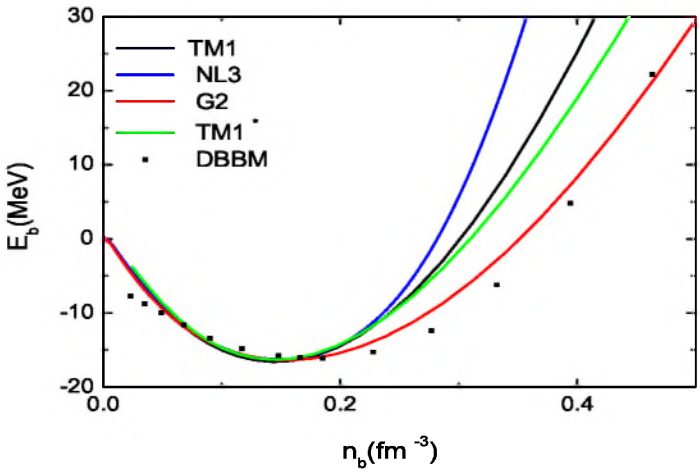

Figure 8.1: Binding energy as a function of the baryon density for symmetric nuclear matter

From Fig. 8.1 one can see that at low densities there is a good correlation between the relativistic mean field and DBHF results. The NL3 parameter set gives the stiffest equation of state, which in consequence leads to an unrealistically high value of the maximum neutron star mass. The G2 and TM1* parameter sets give the best agreement with the DBHF results at the high density region.

8.2 Infinite symmetric strange hadronic matter

For symmetric strange hadronic matter there is still no isospin dependence. There are only two conserved charges: the baryon number $n_b = n_N + n_\Lambda + n_\Xi$ where $n_B = \gamma_B k_{F_B}^3/6\pi^2$, $B = N, \Lambda, \Xi$ and γ_B stands for the spin-isospin degeneracy factor which equals 4 for nucleons and Ξ hyperons and 2 for Λ, and the strangeness number $n_S = n_\Lambda + 2n_\Xi$. These two quantities allow one to define the parameter which specifies the strangeness content in the system and is strictly connected to the

appearance of particular hyperon species in the model

$$f_s = \frac{n_\Lambda + 2n_\Xi}{n_b}. \tag{8.1}$$

In a multi-strange system, for sufficient number density of Λ hyperons, the process $\Lambda + \Lambda \rightarrow \Xi + N$, where N stands for nucleon, becomes energetically allowed. Thus, apart from nucleons and Λ hyperons, Ξ^- and Ξ^0 hyperons also have to contribute to the composition of strange hadronic matter. In general, the chemical equilibrium conditions for the processes $\Lambda + \Lambda \rightarrow n + \Xi^0$ and $\Lambda + \Lambda \rightarrow p + \Xi^0$ are established by the following relations between chemical potentials

$$2\mu_\Lambda = \mu_n + \mu_{\Xi^0} \qquad 2\mu_\Lambda = \mu_p + \mu_{\Xi^-}. \tag{8.2}$$

These relations for symmetric matter can be rewritten as $2\mu_\Lambda = \mu_N + \mu_\Xi$. The chemical potential μ_B ($B = N, \Lambda, \Xi$) is related to the Fermi energy of each baryon in the following way

$$\mu_B = \sqrt{m_{B,eff}^2 + k_{F,B}^2} + g_{\omega B} w_0 + g_{\phi B} f_0 \tag{8.3}$$

and the binding energy of the system can be obtained from the relation

$$E_b = \frac{1}{n_b}(\varepsilon - Y_N m_N - Y_\Lambda m_\Lambda - Y_\Xi m_\Xi), \tag{8.4}$$

where Y_B ($B = N, \Lambda, \Xi$) denotes relative concentrations of particular baryons.

The density dependence of the binding energies of multi-strange system involving nucleons, Λ and Ξ hyperons for TM1 and TM1* parameter sets are presented in Fig. 8.2, 8.3, 8.4 and 8.5.

For each parameterization the strong and weak Y – Y coupling are considered (Table 8.4). Individual lines represent the binding energies obtained for different values of the strangeness fraction f_s. In all cases the value $f_s = 0$ corresponds to the state when only nucleons are present in the system and the EOS characteristic to nuclear matter is reproduced. For both parameterizations (TM1 and TM1*), in the case of strong Y – Y interaction the increasing value of f_s leads to a more bound system with the minimum shifted towards higher densities. Contrary to this situation the increasing value of strangeness content in hyperon matter characterized by weak Y – Y interaction gives shallower minima in the result. Increasing the value of the parameter f_s, which

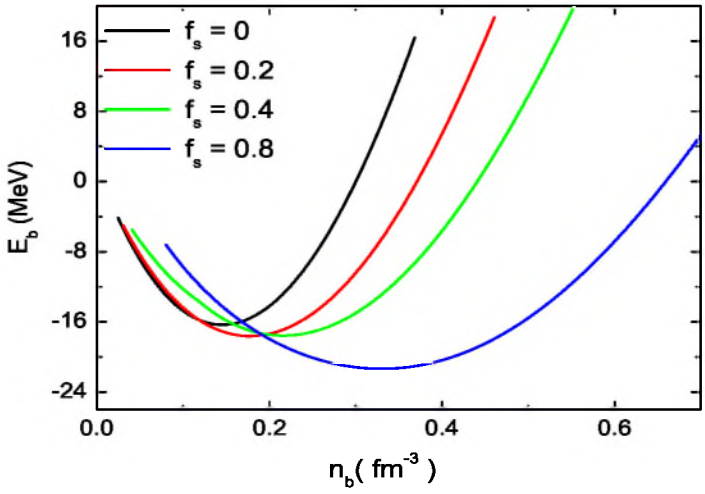

Figure 8.2: Density dependence of the binding energy E_b for TM1 parameter set, for different values of strangeness fraction f_s. The results have been obtained for the strong $Y-Y$ coupling model

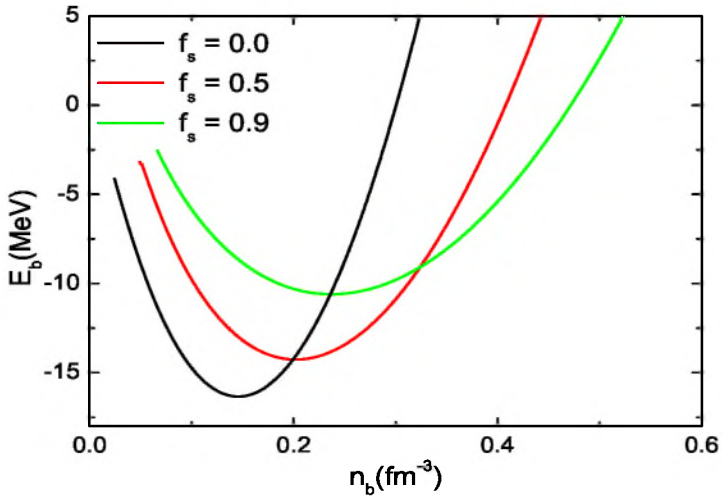

Figure 8.3: Density dependence of the binding energy E_b for TM1 parameter set, for different values of strangeness fraction f_s. The results have been obtained for the weak $Y-Y$ interaction model

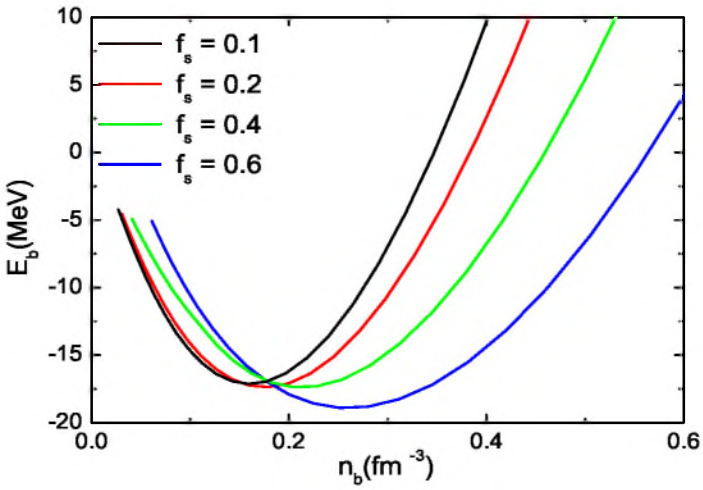

Figure 8.4: Density dependence of the binding energy E_b for TM1* parameter set obtained for different values of strangeness content f_s. The results for the strong $Y-Y$ interaction are presented

is equivalent to the increasing value of the strangeness content in the matter, the binding energy for each fixed value of the parameter f_s has been calculated. The minimum values of binding energies for the fixed values of f_s have been determined and the results are plotted in Fig. 8.6 and 8.7.

The equilibrium density n_0 can be calculated by minimizing the binding energy with respect to the baryon number density n_b. In Fig. 8.8 the equilibrium density n_0 as a function of the strangeness content for the two above mentioned cases is presented.

Results are depicted for TM1 parametrization. In the weak model the saturation density depends weakly on the strangeness ratio, while in the strong model this dependence is much stronger. Relative concentrations of Λ and Ξ hyperons in the case of symmetric strange hadronic matter are presented in Fig. 8.9 and 8.10. In both cases the onset of Λ hyperons is followed by the onset of Ξ hyperons. The populations of Λ hyperons obtained with the use of TM1 and TM1*– weak parameter sets are reduced in comparison with those calculated for the strong Y – Y interaction models. Concentrations of Ξ hyperons are higher for the weak TM1 and TM1* models. In the case of weak Y – Y interaction model the Ξ hyperon thresholds are shifted towards lower strangeness

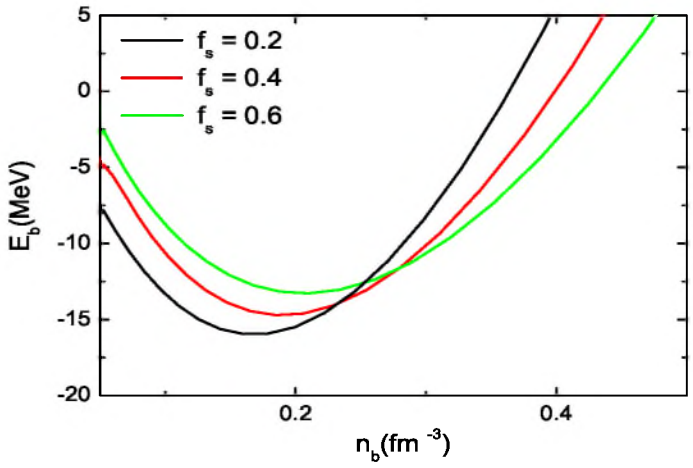

Figure 8.5: Density dependence of the binding energy E_b for TM1* parameter set supplemented with the weak $Y-Y$ interaction obtained for different values of strangeness content f_s

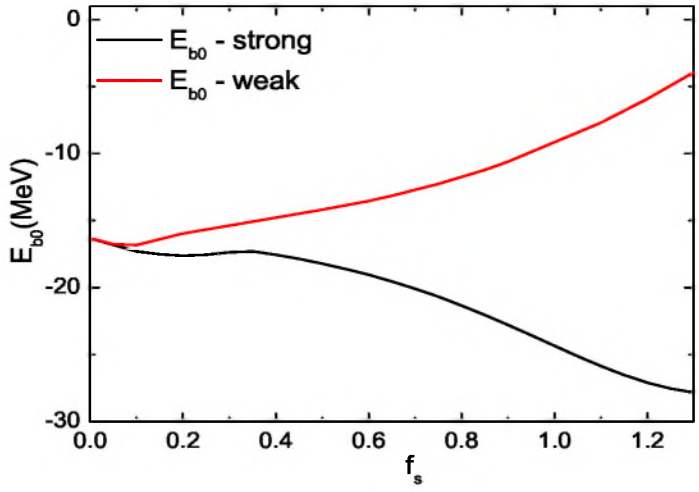

Figure 8.6: The minimized energy per baryon for TM1 parameter set calculated for the strong and weak $Y-Y$ interaction models

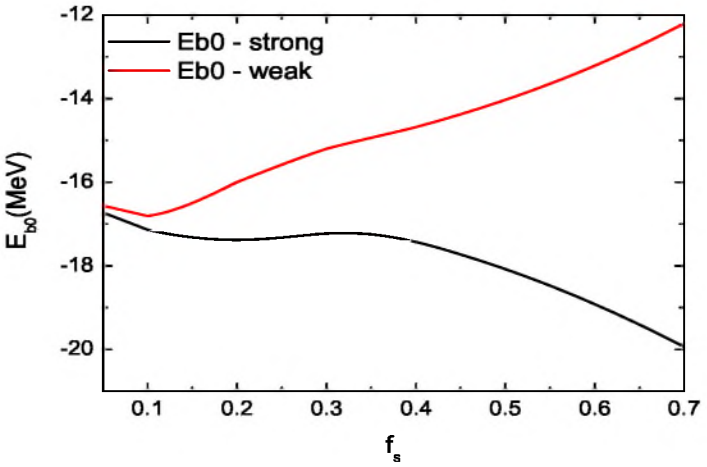

Figure 8.7: The minimized energy per baryon for TM1* parameter set calculated for the strong and weak $Y-Y$ interaction models

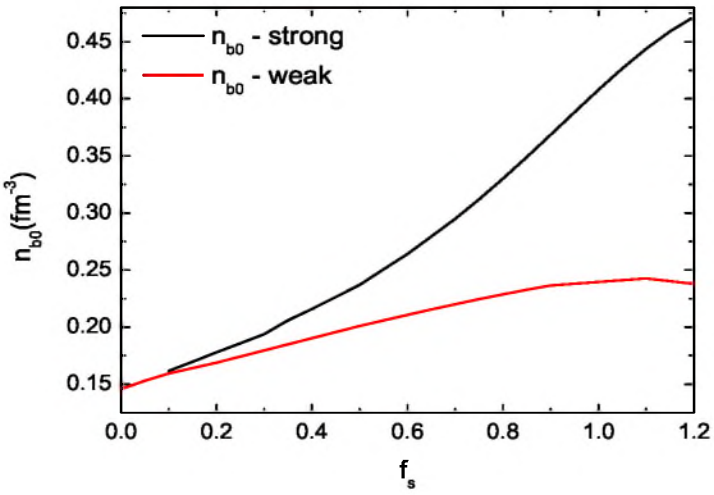

Figure 8.8: The equilibrium density n_0 as a function of the strangeness content f_s

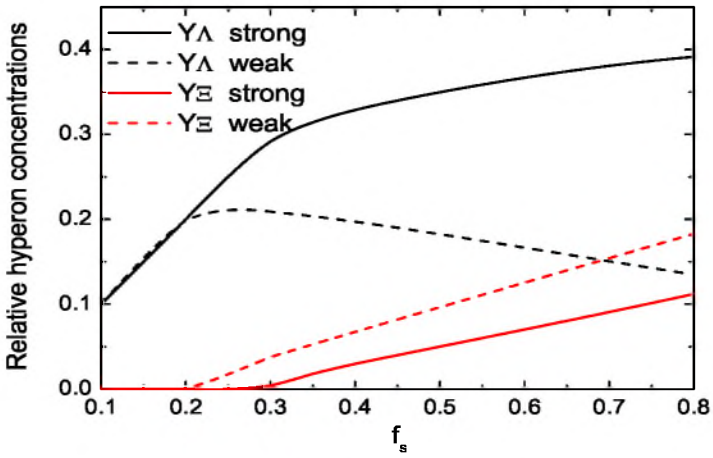

Figure 8.9: Relative concentrations of Λ and Ξ hyperons in strange hyperon matter for TM1 parameter set

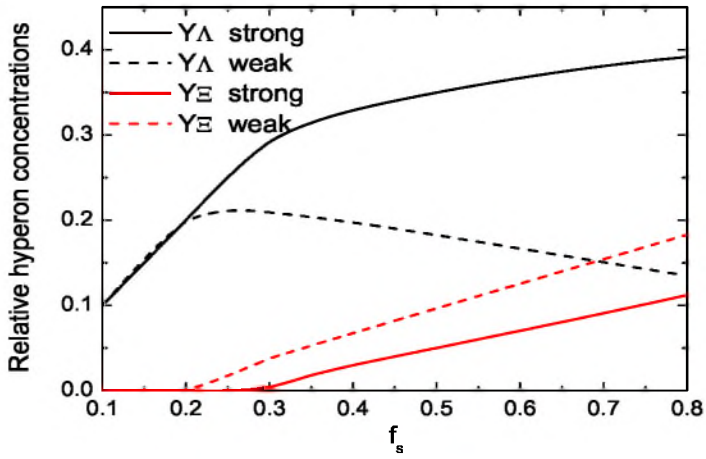

Figure 8.10: Relative concentrations of Λ and Ξ hyperons in strange hyperon matter for TM1* parameter set

fractions. This influences the properties of neutron star matter. The population of Ξ hyperons in the TM1* model is reduced in comparison with that obtained within the TM1 model for both strong and weak hyperon-hyperon couplings [141].

8.3 Asymmetric nuclear matter

The properties of isospin asymmetric nuclear matter have been extensively analyzed with the use of many different methods based on: the non-relativistic Brueckner approach, the relativistic Brueckner approach, the variational many-body approach, relativistic mean field theory, relativistic and non-relativistic Hartree–Fock and Thomas–Fermi approximation and the chiral sigma model. In the relativistic mean field approach the nuclear system is characterized by baryonic fields surrounded by a background of classical mesonic fields with different Lorentz properties. The isoscalar part describes the symmetric matter but the description of asymmetric nuclear matter requires the inclusion of the isovector sector. This can be introduced in a minimal fashion with only the isovector ρ meson included. However, more detailed analysis can be done when the model is supplemented by additional mixed isoscalar-isovector couplings Λ_V and Λ_4 or by the inclusion of the virtual δ (a_0 (980)) meson. The isovector sector contains the isovector-vector part – the ρ^a_μ meson and the isovector-scalar part – the δ^a meson. Using the asymmetry parameter f_a which specifies the relative neutron excess in the system the EOS for differen isospin asymmetry can be obtained. Increasing the value of the parameter f_a, which is equivalent to the increasing number of neutrons in the matter, the binding energy for each fixed value of the parameter f_a has been calculated. In Fig. 8.11 and 8.12 the density dependence of binding energies for different values of asymmetry parameters f_a are presented. Calculations have been performed for TM1 and TM1* parameter sets.

Analyzing forms of the of asymmetric nuclear matter obtained for the chosen parameterizations one can conclude that the characteristic common feature for all considered cases is that the asymmetric nuclear matter is less bound and less stiff at saturation. Increasing the isospin asymmetry adds more repulsion to the system. The minimum values of binding energies for the fixed values of f_a have been determined and the results are plotted in Fig. 8.13 and 8.14.

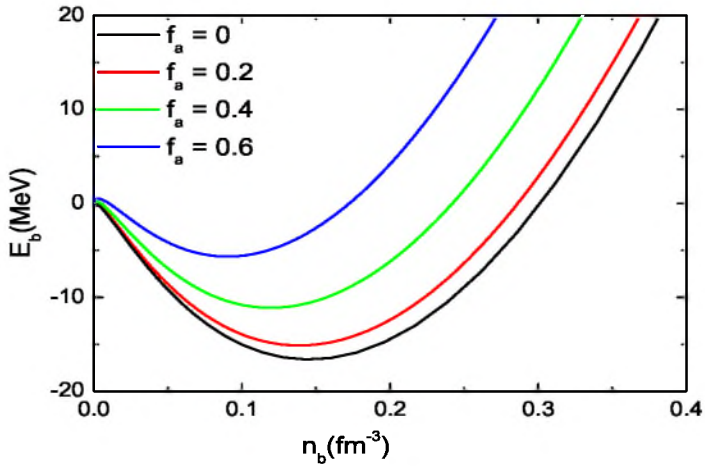

Figure 8.11: Binding energy as a function of baryon density n_b for different values of the asymmetry parameter f_a for TM1 parameter set

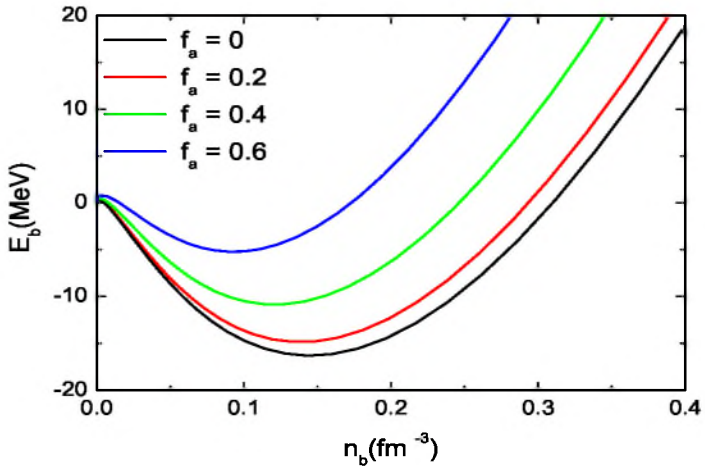

Figure 8.12: Binding energy as a function of baryon density n_b for different values of the asymmetry parameter f_a for TM1* parameter set

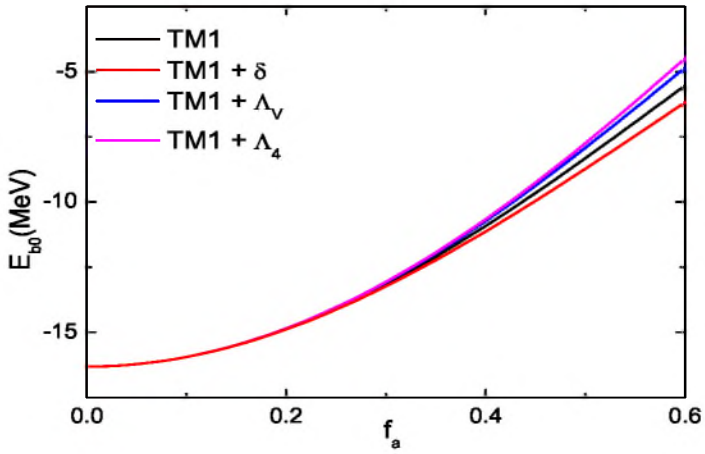

Figure 8.13: The minimized energy per baryon as a function of the asymmetry parameter f_a for TM1 parameter sets and its extensions

Fig. 8.13 compares the results obtained for TM1 parameter set and for its extensions. The variant forms of the standard TM1 parameter set are characterized by the inclusion of isospin dependent terms namely: the mixed $\omega - \rho$ and $\sigma - \rho$ meson interaction terms with the parameters Λ_V and Λ_4 respectively and the model with the inclusion of δ meson. The binding energy at saturation depends weakly on the isospin asymmetry for low values of the f_a parameter. The dependence is stronger for more neutron rich matter. The presence of Λ_V and Λ_4 terms leads to a less bound system, whereas inclusion of δ meson leads to the lowest energy at saturation. A similar analysis has been performed for the TM1* and G2 parameter sets. The results are presented in Fig. 8.14. G2 parameterization gives the less bound matter at saturation and for TM1* parameter set calculations indicates the lowest value of the minimum binding energy. In all of the presented models there is a strong dependence of the saturation density on the isospin asymmetry. For more asymmetric matter the equilibrium density is shifted to lower densities (Fig. 8.15 and 8.16). For example, calculations performed within the Skyrme–Hartree–Fock approach indicate only a slight influence of the isospin asymmetry on

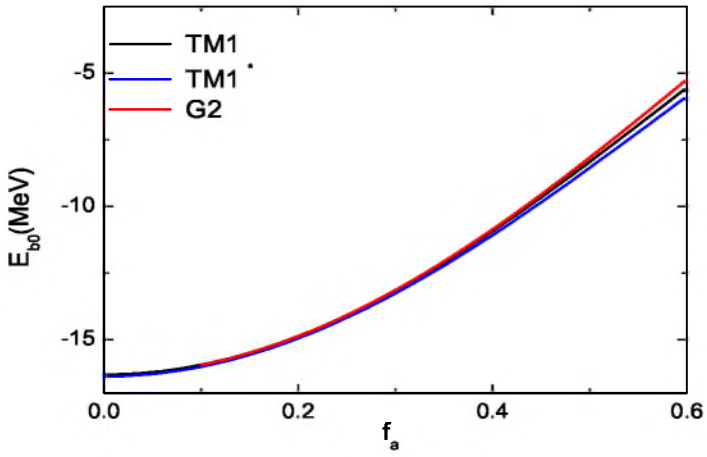

Figure 8.14: The minimized energy per baryon as a function of the asymmetry parameter f_a for TM1, TM1* and G2 parameter sets

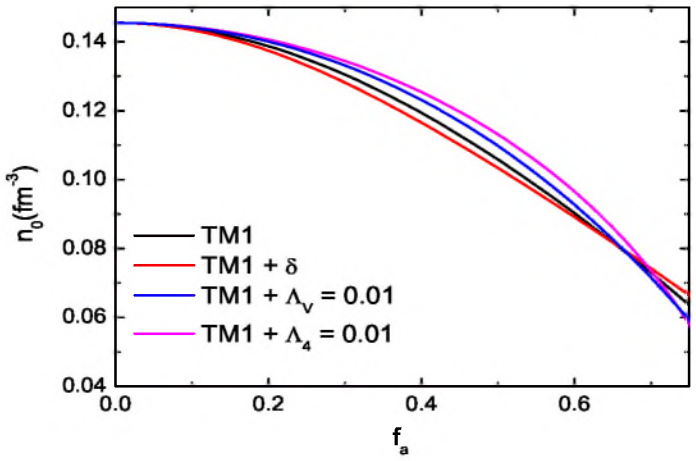

Figure 8.15: The equilibrium density n_0 as a function of the isospin asymmetry for TM1 parameter sets and its extensions

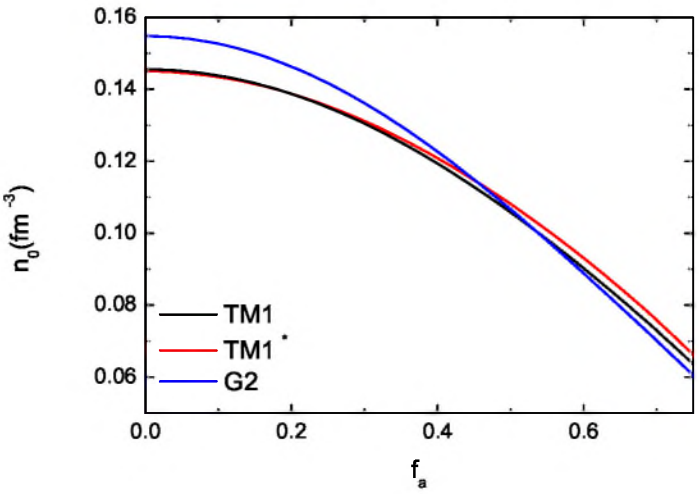

Figure 8.16: The equilibrium density n_0 as a function of the isospin asymmetry for TM1, TM1* and G2 parameter sets

the saturation density. The isospin dependence of the nuclear compressibility at saturation is presented in Fig. 8.17 and 8.18. A basic feature which is common to all the considered models is the decrease of the compressibility with the increasing isospin asymmetry f_a. Similar results have been obtained for the Dirac–Hartree–Fock approach using isoscalar (σ, ω) mesons and both isoscalar and isovector mesons (π, ρ) and in the non-relativistic Hartree-Fock approach with the Skyrme SIII interaction. The rate of decrease varies among models. The model with the δ meson appears to give the stiffest equation of state, whereas inclusion of Λ_V and Λ_4 terms results in softer equations of state. The comparison between the compressibility at saturation for TM1, TM1* and G2 models with respect to isospin effects indicates that the system described with G2 parameterization has the smallest incompressibility at saturation density and TM1* gives the higher values of K_0 at equilibrium. The softening of the equation of state due to the isospin asymmetry is of particular importance in astrophysical applications, especially for the models of supernova explosion and proto-neutron and neutron star structure. Another effect connected with the inclusion of δ meson is the neutron and proton effective mass splitting. Depending on the sign of the third component of the isospin

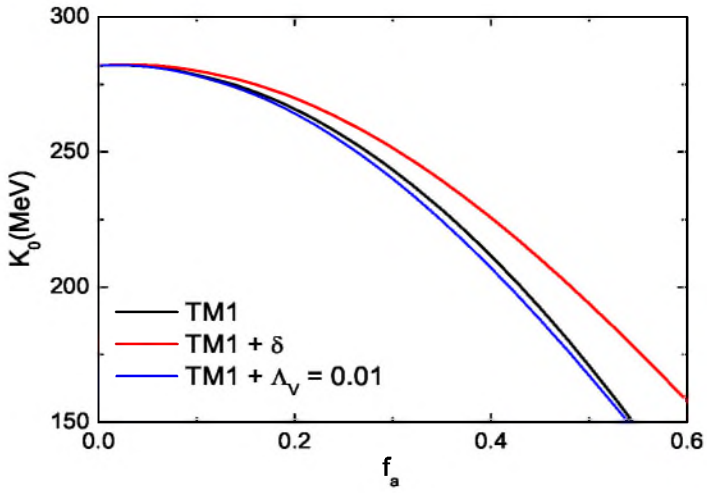

Figure 8.17: The compressibility at saturation as a function of the asymmetry parameter f_a obtained for TM1 parameter sets and its extensions

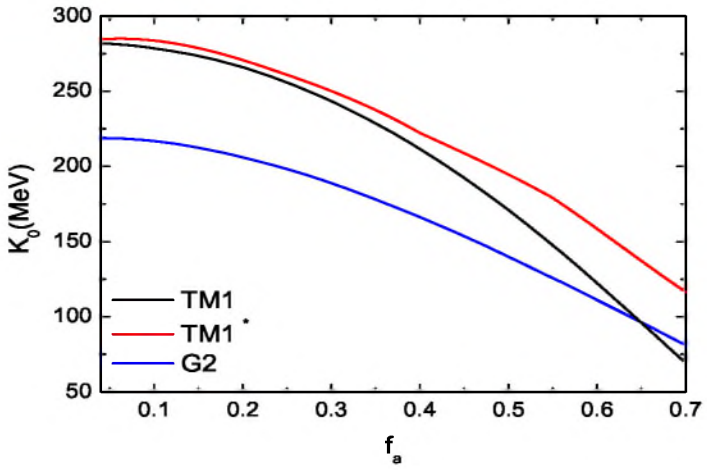

Figure 8.18: The compressibility at saturation as a function of the asymmetry parameter f_a for TM1, TM1* and G2 parameter sets

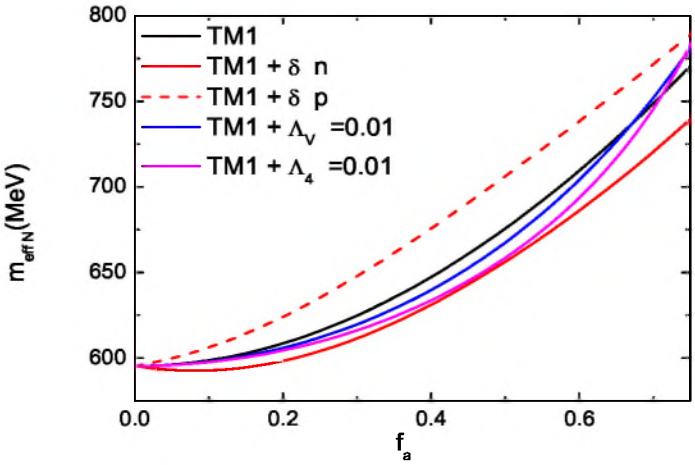

Figure 8.19: The effective nucleon mass at saturation as a function of the asymmetry parameter f_a for TM1 parameter sets

the δ meson interaction increases the proton and decreases the neutron effective masses. In Fig. 8.19 and 8.20 the influence of isospin asymmetry on the effective nucleon mass at saturation is presented. The effective mass at saturation increases with the increasing asymmetry.

The presence of δ meson field and its contribution to the symmetry energy E_{sym} imposes constraints on $g_{\rho N}$ and $g_{\delta N}$ coupling constants. With the use of the equation (6.40) the explicit expression for the symmetry energy E_{sym} can be obtained. Parameters $g_{\rho N}$ and $g_{\delta N}$ in the equation (6.40) are adjusted to get the experimental value of the symmetry energy coefficient $E_{sym}(n_0)$.

The obtained results namely the symmetry energy as a function of density are presented in Fig. 8.21 and 8.22. The symmetry energies for TM1 model and its extensions are presented in Fig. 8.21. The inclusion of δ meson in all the presented models increases the stiffness of the symmetry energy especially at high densities, whereas the nonlinear terms make the symmetry energy softer. Comparing the results obtained with the use of TM1, TM1* and G2 parameterizations it is obvious that G2 parameter set gives the softer symmetry energy and TM1 the stiffest one. The presence of nonlinearities leads to rather soft symmetry energy.

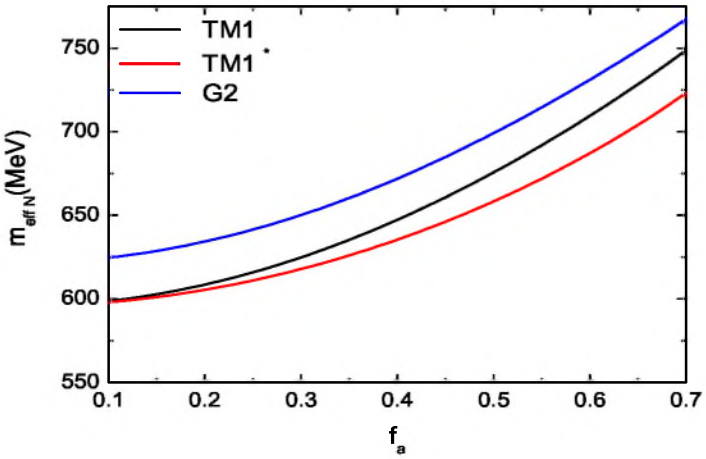

Figure 8.20: The effective nucleon mass at saturation as a function of the asymmetry parameter f_a for TM1, TM1* and for G2 parameter sets

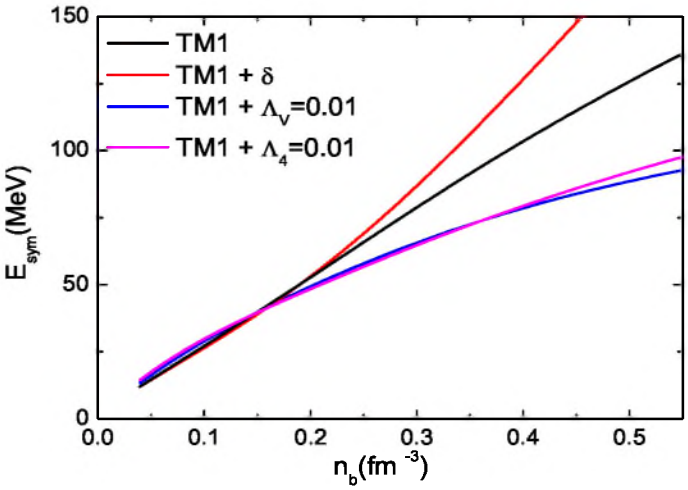

Figure 8.21: The density dependence of the symmetry energy for TM1 parameter set and its extensions

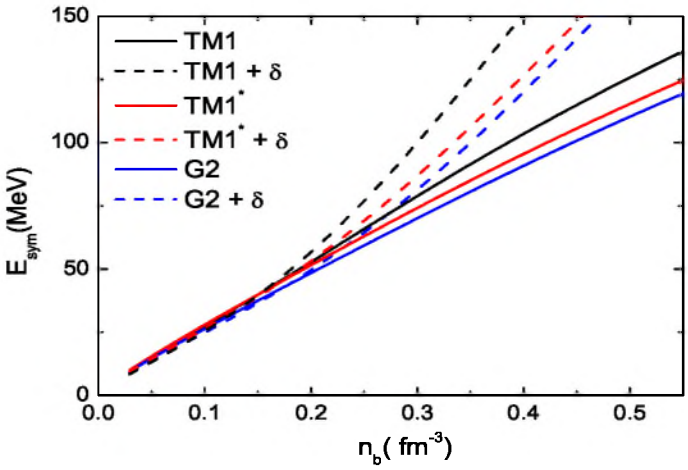

Figure 8.22: The density dependence of the symmetry energy for TM1, TM1* and G2 parameter sets. The effect of the inclusion of δ meson is shown

8.4 Asymmetric strangeness-rich matter

The formation of strange matter during the evaporation process which follows central collisions of heavy ions leads either to the creation of small lumps of strange quark matter (strangelets) or strange hadronic matter (Metastable Exotic Multihypernuclear Objects – MEMOs) [148], [149]. Depending on the lifetime of the strange matter system it can be considered as stable against weak hadronic decay for long-lived matter and stable against strong decay for the short-lived one. Only the short-lived strange matter system is taken into account in this analysis which is equivalent to the time scale, during which the system is observed. It has to be short enough so that the weak decays of the strange baryons can be neglected. As has been shown certain classes of MEMOs exist [148]. In this analysis the Pauli blocked system consisting of p, n, Λ, Ξ^0 and Ξ^- has been considered. The system is characterized by the conservation of baryon, isospin and strangeness numbers. In order to study the properties of asymmetric strangeness-rich matter, two parameters are incorporated one that defines the strangeness of the system $f_s = n_b^S/n_b$ where n_b^S is the strangeness density and the another which is connected with the total isospin of the system and is defined

as the ratio of the isospin density to the baryon density $f_3 = n_b^3/n_b$. The isospin density is given by the relation

$$n_b^3 = \sum_b I_b^3 n_b. \tag{8.5}$$

The quantity f_3 can be related to the asymmetry parameter f_a, now extended to the case when Ξ^0 and Ξ^- hyperons are also included leading to the relation $f_a = -2f_3$. In consecutive figures (Fig. 8.23, 8.24, 8.25, 8.26, 8.27, 8.28, 8.29 and 8.30) the binding energies of the system as a function of baryon number density are presented. Two parameterizations have been used, TM1 and TM1*. For both parameterizations the strong and weak Y – Y interactions are considered.

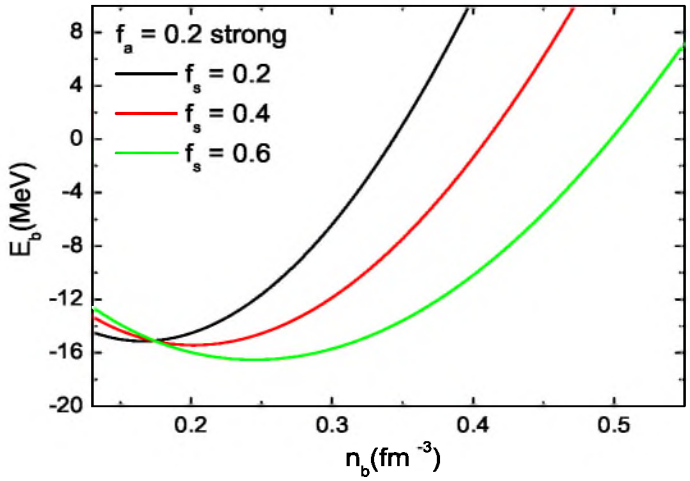

Figure 8.23: Density dependence of the binding energy E_b for TM1 parameter set for different values of strangeness contents f_s, for the strong $Y - Y$ interaction ($f_a = 0.2$)

These figures have been constructed for two different values of the asymmetry parameters $f_a = 0.2$ and $f_a = 0.6$. Thus each figure includes curves obtained for various strangeness ratios at a fixed value of the isospin asymmetry parameter f_a. In the case of strong Y – Y interaction when the asymmetry is low ($f_a = 0.2$) the increasing value

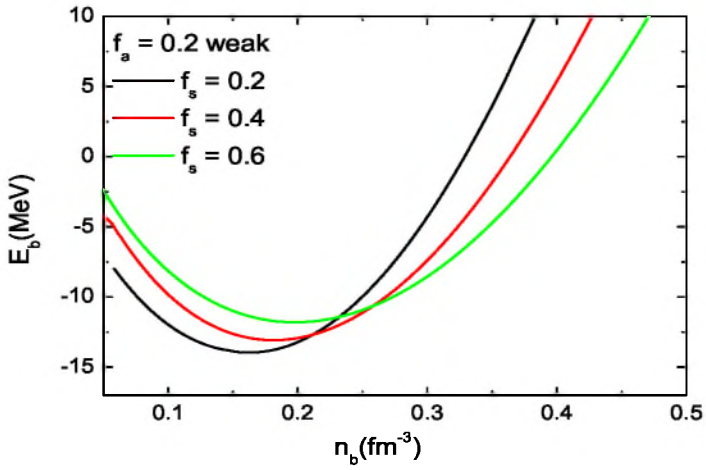

Figure 8.24: Density dependence of the binding energy E_b for TM1 parameter set for different values of strangeness fraction f_s, for the weak $Y-Y$ interaction model ($f_a = 0.2$)

of strangeness ratios leads to a more bound system with the minima shifted to higher densities. In Fig. 8.24 the same analysis has been done for the weak model. The matter is less bound for the increasing value of the strangeness fraction. When the asymmetry of the system is significantly increased ($f_a = 0.6$) in the case of strong Y – Y interaction models (for TM1 and TM1* parameter sets) the increasing value of strangeness gives only slight differences in the binding energy at saturation density. Contrary to this situation the increasing value of strangeness contents in hyperon matter characterized by weak Y – Y interaction gives shallower minima in the result. The more asymmetric system is less bound and there are only minor changes of the saturation densities when compared with the more symmetric ($f_a = 0.2$) system. These results are shown in Fig. 8.26. For comparison the results for TM1* parameterization are shown in Fig. 8.27 and 8.30.

Results for TM1* parameterization for strong and weak Y – Y interactions for the more asymmetric matter are presented in Fig. 8.29 and 8.30. The minimum values of binding energies as functions of the asymmetry parameter f_a for fixed values of f_s have been determined and the results are plotted in Fig. 8.31 and 8.32 for TM1 and TM1* parameter sets, for the strong hyperon-hyperon interaction, whereas in

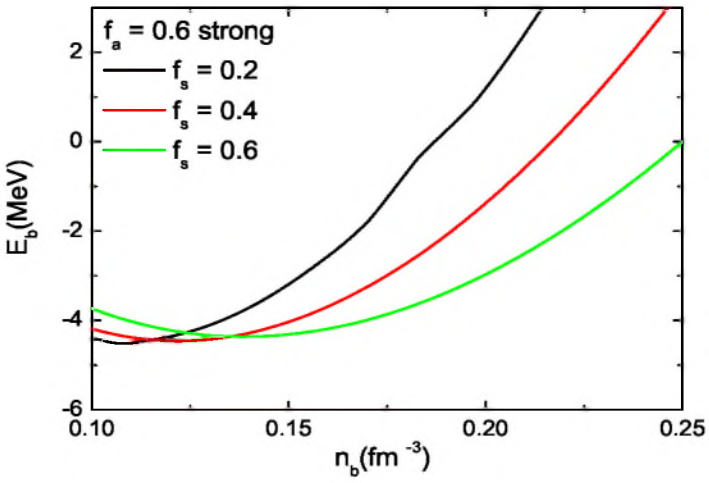

Figure 8.25: Density dependence of the binding energy E_b for TM1 parameter set for different values of strangeness contents f_s, for the strong $Y-Y$ interaction ($f_a = 0.6$)

Fig. 8.33 and 8.34 the same results for the weak models are shown. In Fig. 8.35 and 8.36 and 8.37 and 8.38 the minimum values of binding energies as functions of the strangeness ratio f_s for the fixed values of the isospin asymmetry f_a have been shown. The strong and weak parameter sets have been considered.

Analyzing the case of high asymmetry and high strangeness contents in the system for strong Y – Y interaction one can see that when the isospin asymmetry of the system is sufficiently high the increasing value of strangeness content leads to less bound matter.

This can be seen also in Fig. 8.39 and 8.40 where the saturation energy as a function of the parameter f_s is plotted. Two separate cases are considered: the first for $f_a = 0.4$ and the second for $f_a = 0.6$. The latter one depicts the behavior of the saturation energy for the strong model when the asymmetry of the matter is high and the matter becomes less bound for the higher value of the strangeness fraction f_s.

A similar analysis has been performed for the behavior of the compression modulus K_0 of the strange, asymmetric nuclear matter. Calculations performed for TM1 and TM1* parameter sets with the weak hyperon-hyperon interaction lead to the similar results as in the case of non-strange asymmetric nuclear matter. However, value of K_0 shows

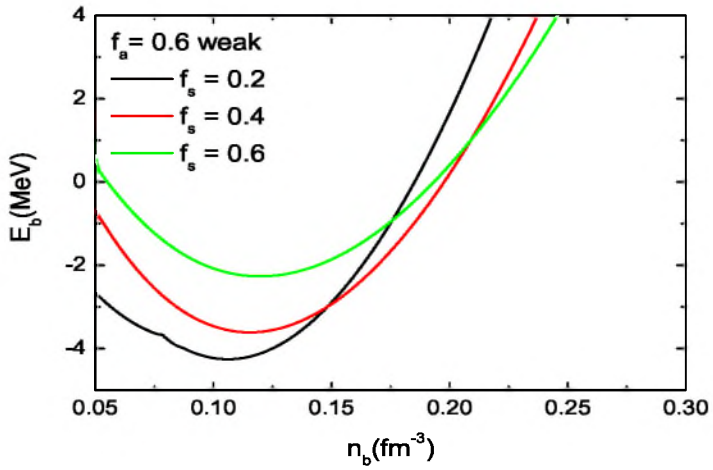

Figure 8.26: Density dependence of the binding energy E_b for TM1 parameter set for different values of the parameter f_s, for the weak $Y-Y$ coupling model ($f_a = 0.6$)

significant variations in the case of TM1* parameter set with the strong hyperon-hyperon interactions. Fig. 8.41 shows the changes of K_0 with the increasing value of the strangeness contents f_s. Calculations have been done for fixed values of the asymmetry parameter f_a. For the low value of the asymmetry parameter ($f_a = 0.2$) the increasing value of strangeness contents only slightly influences the value of K_0. When the nuclear matter becomes more asymmetric the compression modulus decreases for low values of the f_s parameter and after reaching the minimal value increases for nuclear matter with high strangeness content. Fig. 8.42 presents the values of the compression modulus K_0 as a function of the asymmetry parameter f_a for the selected values of the strangeness content f_s. Although the compression modulus K_0 is not always a reliable parameter that specifies the stiffness of the EOS, however, in this case it indicates variations of the stiffness of the EOS. Fig. 8.43 and 8.44 illustrate the variation of the baryon effective masses m_{effB} at saturation with the increasing value of the f_a and f_s parameters.

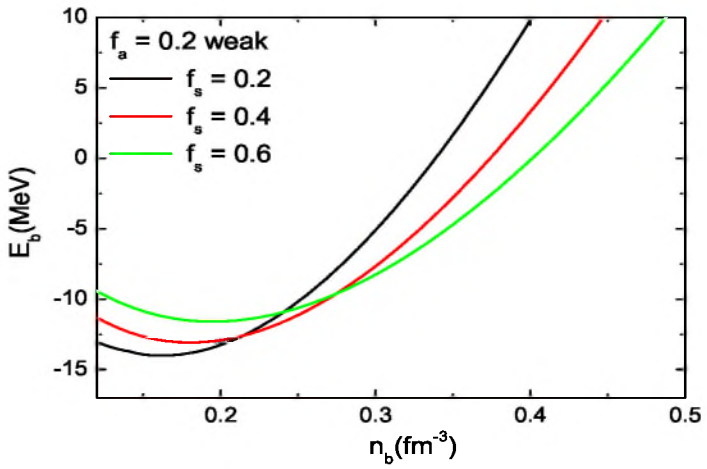

Figure 8.27: Density dependence of the binding energy E_b for TM1* parameter set for different values of strangeness contents, for the strong $Y-Y$ coupling ($f_a = 0.2$)

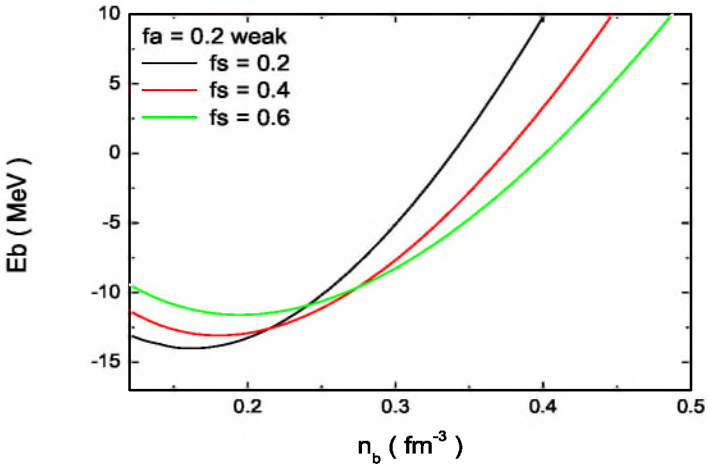

Figure 8.28: The same as in Fig. 8.27 for the weak $Y-Y$ coupling model ($f_a = 0.2$)

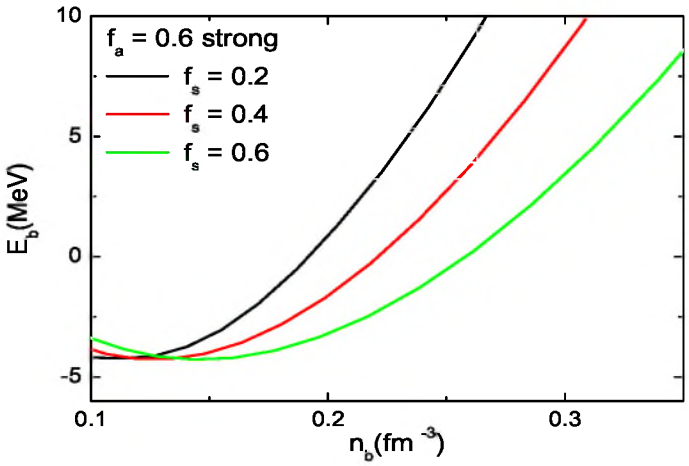

Figure 8.29: Density dependence of the binding energy E_b for TM1* parameter set with the strong $Y-Y$ coupling for different values of strangeness contents f_s ($f_a = 0.6$)

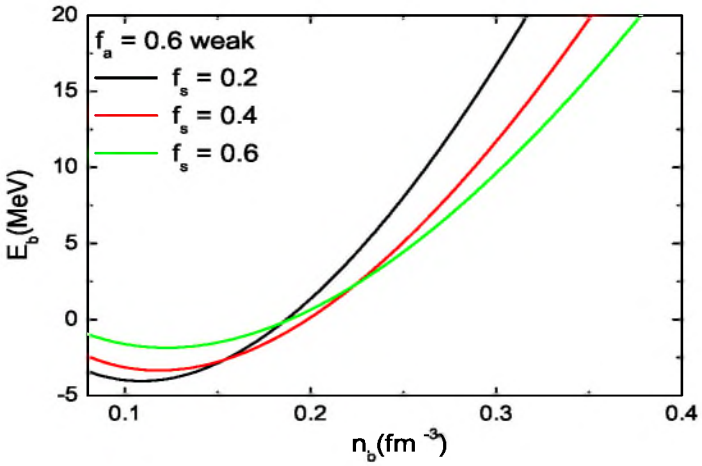

Figure 8.30: The same as in Fig. 8.29 for the weak $Y-Y$ coupling model ($f_a = 0.6$)

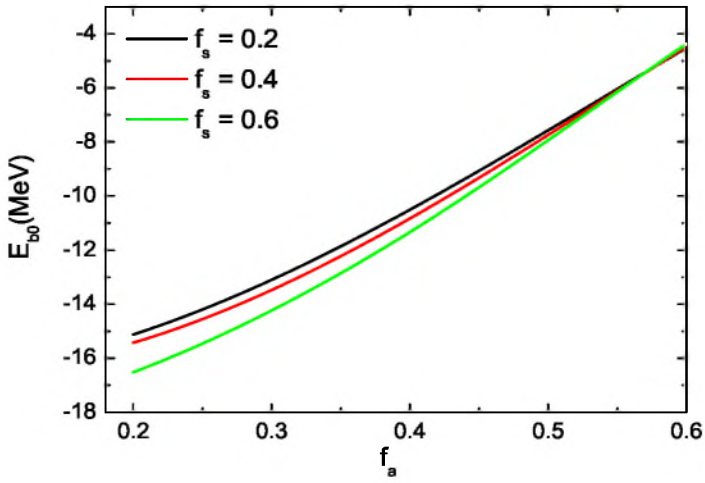

Figure 8.31: The binding energy at saturation as a function of the asymmetry parameter f_a for fixed values of strangeness contents f_s, for TM1 parameter set with the strong $Y-Y$ interactions

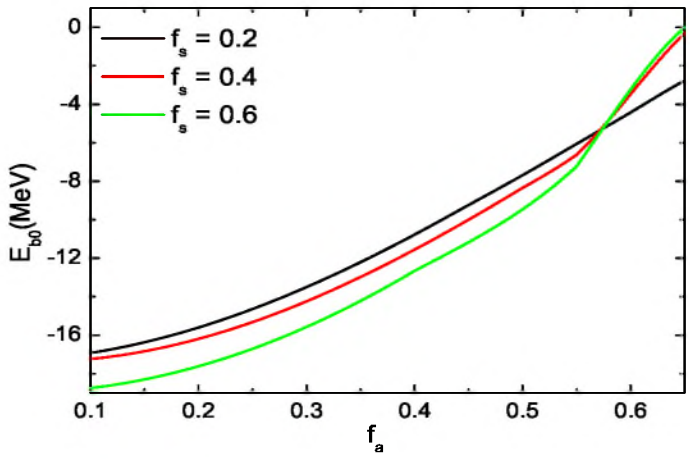

Figure 8.32: The binding energy at saturation as a function of the asymmetry parameter f_a for fixed values of strangeness content f_s, for the TM1* parameter set with the strong $Y-Y$ coupling

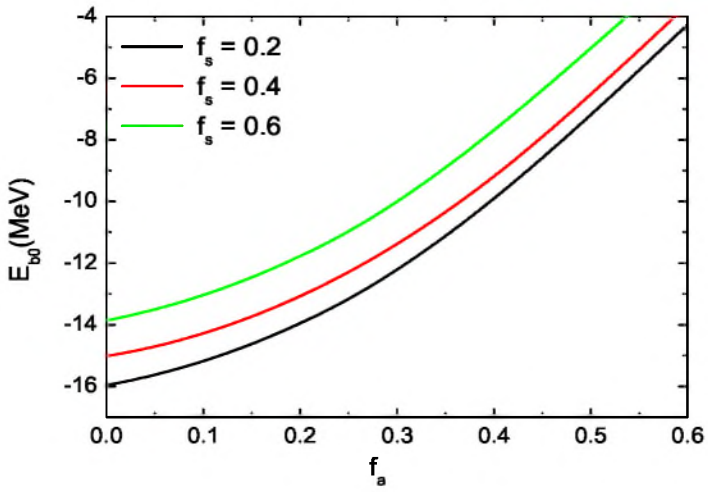

Figure 8.33: The binding energy at saturation as a function of the asymmetry parameter f_a for fixed values of strangeness contents f_s, for the weak $Y-Y$ coupling for TM1 parameter set

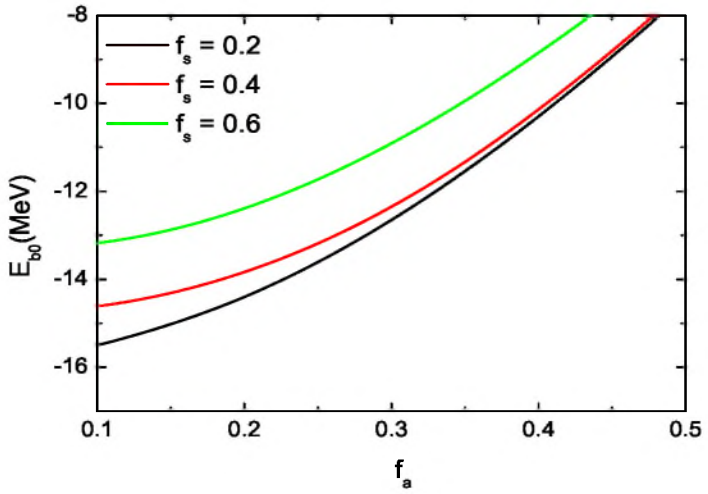

Figure 8.34: The binding energy at saturation as a function of the asymmetry parameter f_a for fixed values of strangeness content f_s, for the weak $Y-Y$ coupling, for the TM1* parameter set

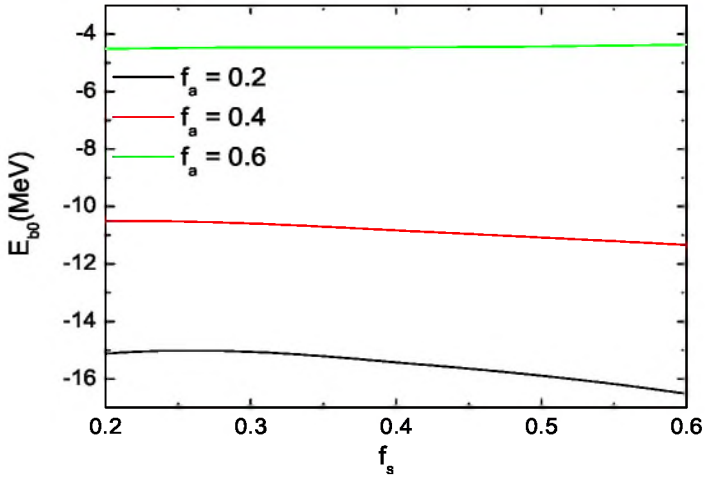

Figure 8.35: The binding energy at saturation as a function of the parameter f_s for fixed values of the isospin asymmetry f_a, for the strong $Y-Y$ coupling, for TM1 parameter set

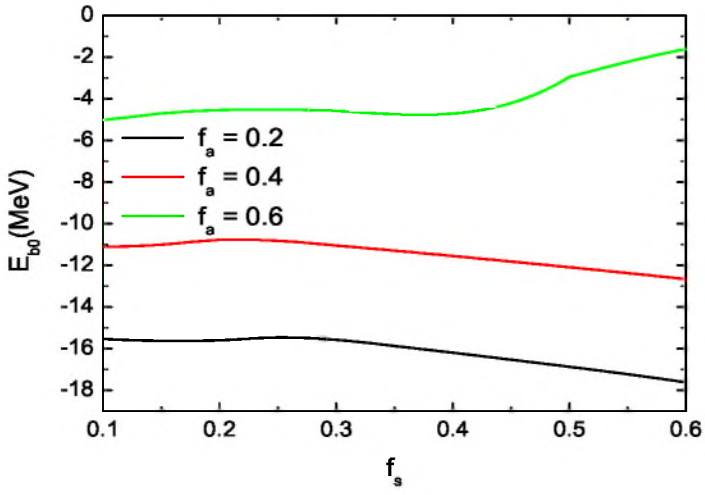

Figure 8.36: The binding energy at saturation as a function of the parameter f_s for fixed values of the isospin asymmetry f_a, for the strong $Y-Y$ coupling, for TM1* parameter set

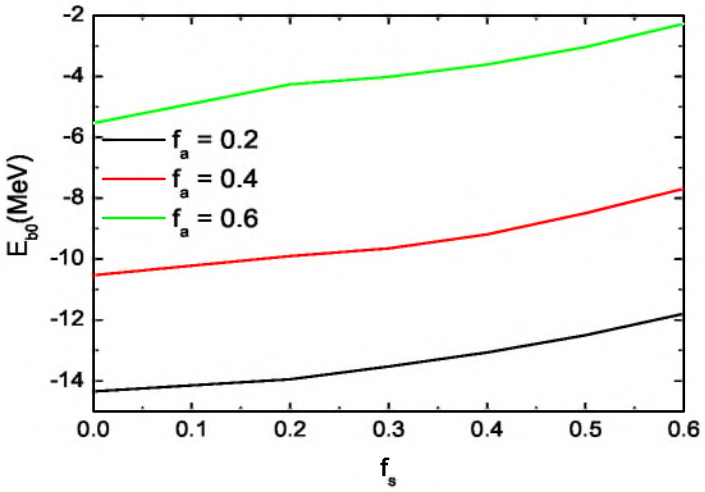

Figure 8.37: The binding energy at saturation as a function of the parameter f_s for fixed values of the isospin asymmetry f_a, for the weak $Y-Y$ coupling, for TM1 parameter set

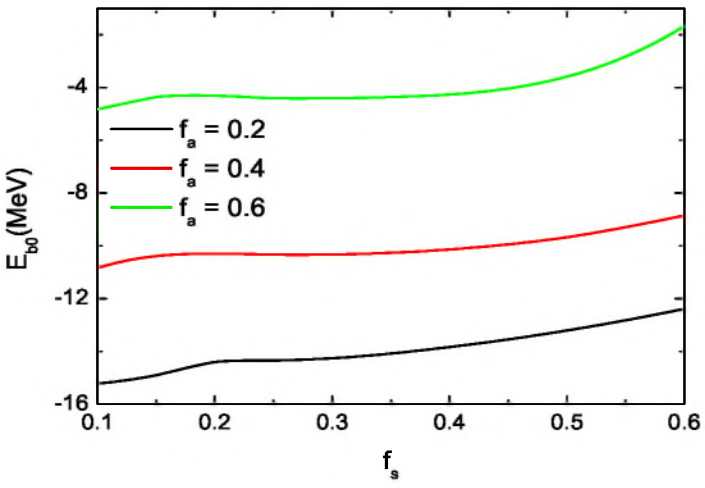

Figure 8.38: The binding energy at saturation as a function of the parameter f_s for fixed values of the isospin asymmetry f_a, for the weak $Y-Y$ coupling, for TM1* parameter set

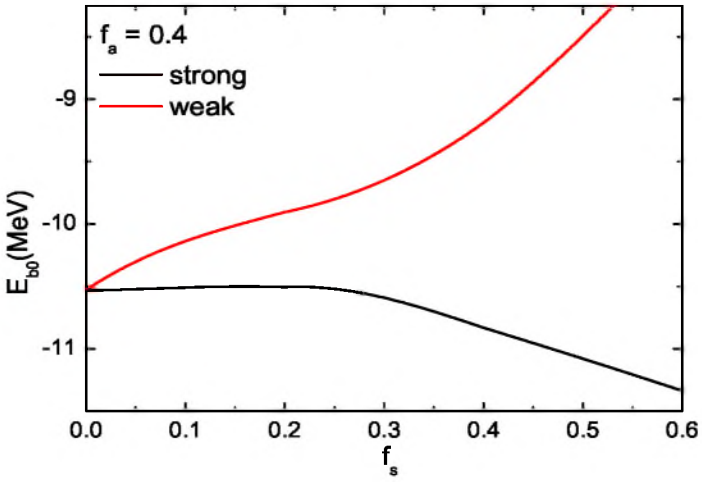

Figure 8.39: The minimized energy per baryon as a function of the strangeness content for TM1* parameter set, for the asymmetry parameter $f_a = 0.4$

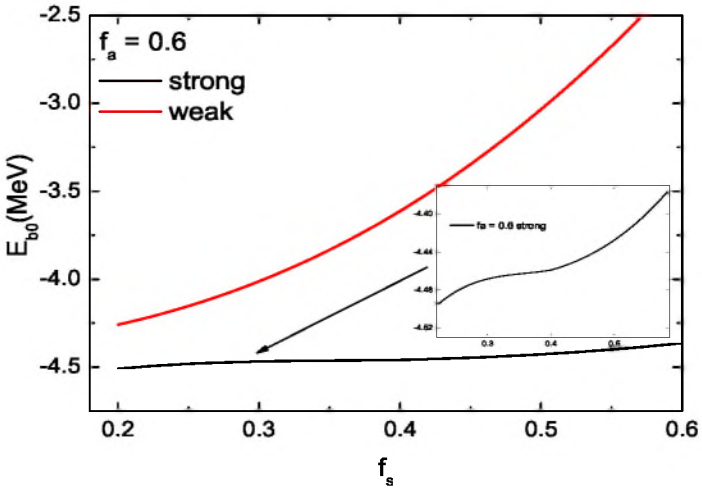

Figure 8.40: The minimized energy per baryon as a function of the strangeness content for TM1* parameter set, for the more asymmetric matter $f_a = 0.6$

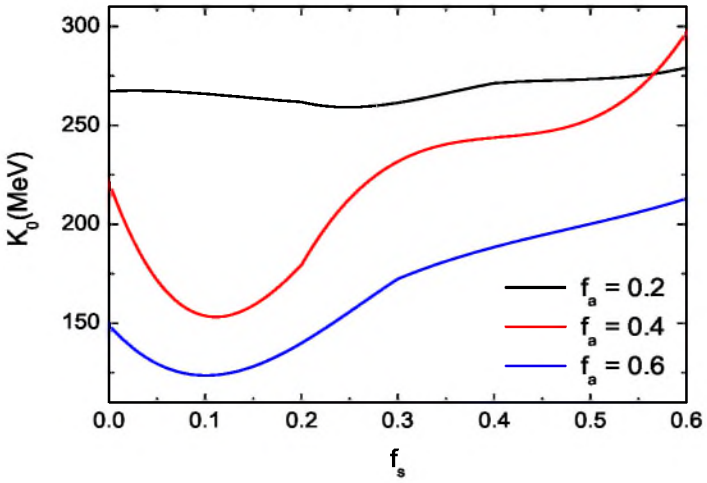

Figure 8.41: The value of the compression modulus K_0 as a function of the strangeness fraction f_s for TM1* parameter set with the strong $Y-Y$ coupling model, for the fixed values of the asymmetry f_a

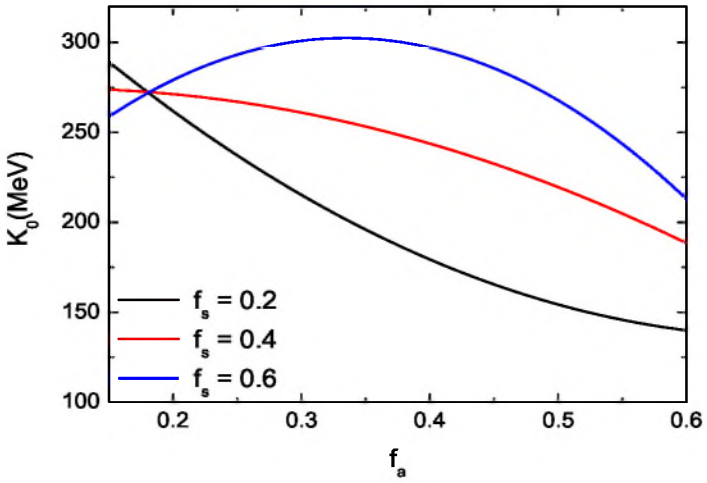

Figure 8.42: The value of the compression modulus K_0 as a function of the asymmetry parameter f_a for fixed values of the strangeness fraction, for TM1* parameter set with the strong $Y-Y$ interaction

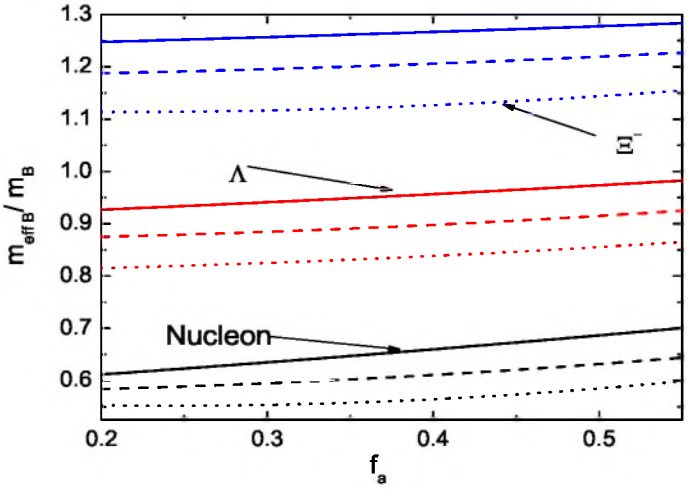

Figure 8.43: The effective baryon mass as a function of the strangeness content f_s for TM1* parameter set with the strong $Y - Y$ coupling, for the selected values of the asymmetry parameter: $f_a = 0.2$ – solid lines, $f_a = 0.4$ – dashed lines, $f_a = 0.6$ – dotted lines

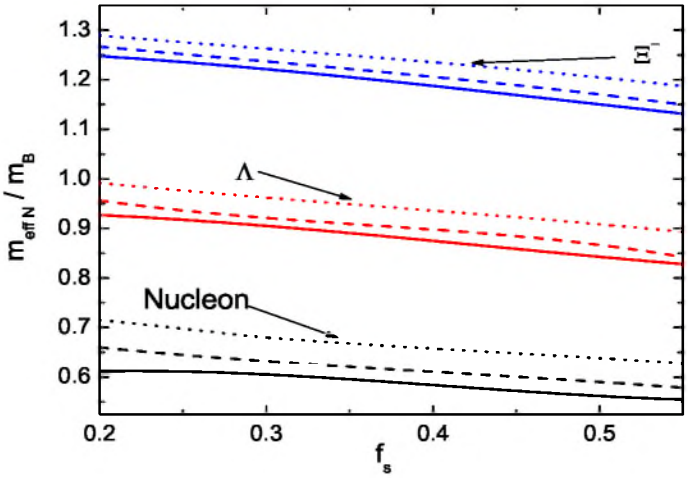

Figure 8.44: The same as in Fig. 8.43 for TM1* parameter set

For the fixed value of the asymmetry parameter, the higher value of the parameter f_s, the lower is the baryon effective mass, whereas for the fixed value of the strangeness content the higher value of the asymmetry parameter f_a leads to a bigger effective baryon mass.

Chapter 9

Neutron star matter

9.1 The equilibrium conditions and composition of stellar matter

The analysis of the role of strangeness in nuclear structure in the context of multi-strange systems is of great importance for neutron star matter. An imperfect knowledge of the neutron star matter EOS, especially in the presence of hyperons causes many uncertainties in determining neutron star structure. The comparison between weak interaction time scales (10^{-10} s) and a time scale connected with the lifetime of a relevant star has been drawn. It indicates that there is a difference between the neutron star matter constrained by charge neutrality and generalized β-equilibrium and the matter in high energy collisions; the second system is constrained by isospin symmetry and strangeness conservation [150]. Since the dynamical time scale of neutron star evolution is much longer than the weak decay time scale of baryons (including strangeness conservation breaking processes), neutron star matter is considered as a system with the conserved baryon number $n_b = \sum_B n_B$ (B = n, p, Λ, Ξ^-, Ξ^0) and electric charge in chemical equilibrium with respect to weak decays. Considering the most general case of neutrino-trapped, strangeness-rich matter the chemical equilibrium is characterized by the correlations between chemical potentials, which in the case of the process $p + e^- \leftrightarrow n + \nu_e$ leads to the following relation

$$\mu_{asym} \equiv \mu_n - \mu_p = \mu_e - \mu_{\nu_e}. \tag{9.1}$$

The similar weak process $\mu + \nu_e \leftrightarrow e + \nu_\mu$ leads to

$$\mu_\mu = \mu_e - \mu_{\nu_e} + \mu_{\nu_\mu} = \mu_{asym} + \mu_{\nu_\mu}. \tag{9.2}$$

Assuming that the muon neutrinos are not trapped inside the neutron star matter ($\mu_{\nu_\mu} = 0$) these relations involve three independent chemical potentials μ_n, μ_e and μ_{ν_e} corresponding to baryon number, electric charge and lepton number conservation. In general, weak processes for baryons can be written in the following form [151]

$$B_1 + l \leftrightarrow B_2 + \nu_l, \tag{9.3}$$

where B_1 and B_2 are baryons, and l and ν_l denote lepton and neutrino of the corresponding flavor, respectively. Provided that the weak processes stated above take place in thermodynamic equilibrium the following relation between chemical potentials can be established

$$\mu_B = q_B \mu_n - q_{e_B}(\mu_e - \mu_{\nu_e}). \tag{9.4}$$

In this equation μ_B denotes the chemical potential of baryon B with the baryon number q_B and the electric charge q_{e_B}.

Using the relation (9.4) for Λ, Σ and Ξ hyperons the following results can be obtained

$$\begin{aligned} \mu_\Lambda &= \mu_{\Sigma^0} = \mu_{\Xi^0} = \mu_n,\ \mu_{\Sigma^-} = \mu_{\Xi_-} = \mu_n + (\mu_e - \mu_{\nu_e}), \\ \mu_p &= \mu_{\Sigma^+} = \mu_n - (\mu_e - \mu_{\nu_e}). \end{aligned} \tag{9.5}$$

Muons start to appear in neutron star matter in the process

$$e^- \leftrightarrow \mu^- + \bar{\nu}_\mu + \nu_e \tag{9.6}$$

after μ_μ has reached a value equal to the muon mass. The appearance of muons not only reduces the number of electrons but also affects the proton fraction. Numerical models of the collapsing inner core have shown that there are no muon neutrinos ($\mu_{\nu_\mu} = 0$) and only electron neutrinos are trapped in the matter [9], [151]. Thermally produced μ and τ neutrino pairs are also trapped but the following condition has to be satisfied $\mu_{\nu_i} = -\mu_{\bar{\nu}_i}$, where $i = \mu, \tau$. After deleptonization of proto-neutron star matter there are no trapped neutrinos and $\mu_{\nu_e} = 0$. In this case the number of independent chemical potentials reduces to two (μ_n and μ_e). Thus the ground state of cold non-strange neutron

star matter is thought to be a question of equilibrium dependence on baryon and electric-charge conservation.

Neutrons are the principal components of a neutron star when the density of matter is comparable with the nuclear density. For higher densities it is the equilibrium of the process

$$p + e^- \leftrightarrow n \tag{9.7}$$

which establishes the relation between chemical potentials

$$\mu_p + \mu_e = \mu_n. \tag{9.8}$$

Thus, realistic neutron star models describe electrically neutral high density matter in β equilibrium.

9.2 Neutron star matter with zero strangeness

The high density EOS has a decisive role in determining neutron star global parameters (the mass and radius) and thereby in relating the star central density and its mass and radius. The mass-central density relation can be established for a mass sequence obtained for the specified EOS. The value of the maximum mass given by the EOS is one of the most important parameters which imposes important constraints on the equation of state. The calculated forms of the EOS for the obtained parameter sets are presented in Fig. 9.1 and 9.2. The stiffness of the EOS shows variations. When the δ meson is included all models lead to stiffer equations of state, whereas nonlinearities soften the EOS. At densities in the vicinity of the saturation density the differences between particular equations of state are negligible. The influence of both the δ meson and nonlinearities on the EOS becomes visible at higher densities, however, it is not too strong. Similar analysis can be done comparing the results obtained with the use of the standard TM1 parameter set [197], TM1* and G2. The G2 model gives the softest EOS.

After obtaining the EOS, the mass and radius of the star can be calculated for a given value of the central density. This can be done by integrating the Tolman–Oppenheimer–Volkoff equations:

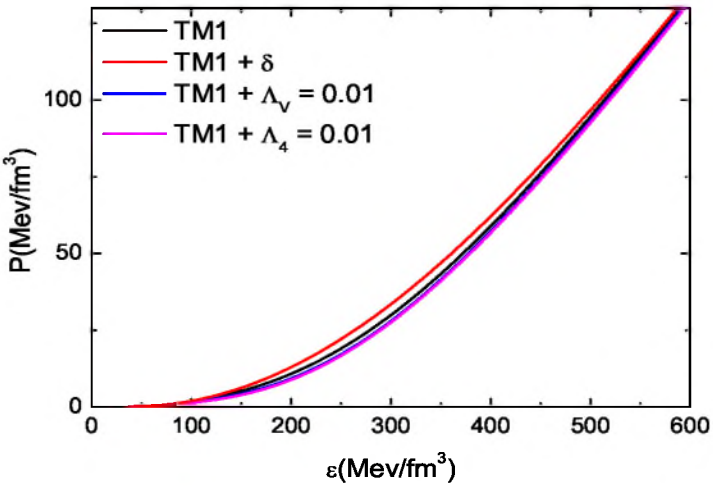

Figure 9.1: The equations of state for TM1 parameter set and its extensions

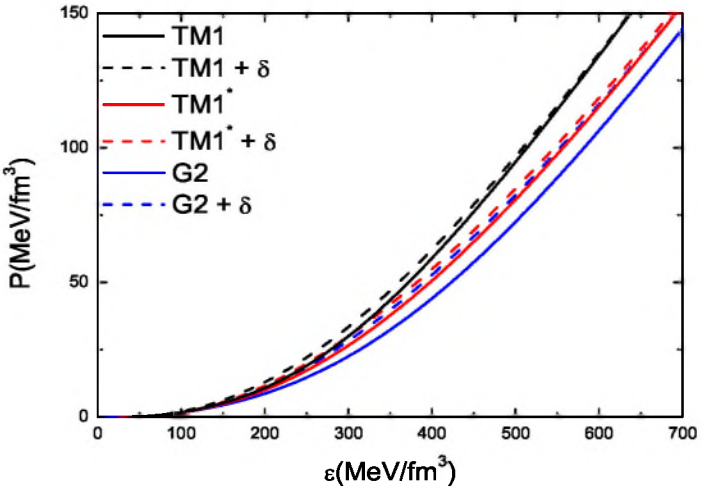

Figure 9.2: The equation of state for TM1, TM1* and G2 parameter sets

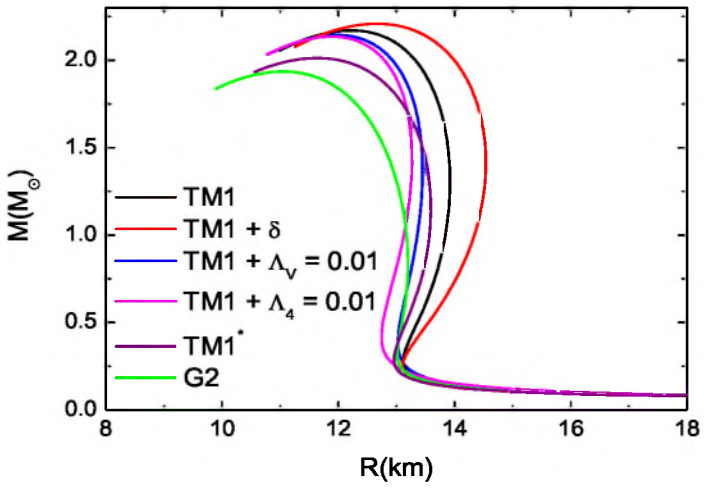

Figure 9.3: The mass-radius relations calculated for TM1 parameter sets

$$\begin{aligned} \frac{dP(r)}{dr} &= -\frac{Gm(r)\varepsilon(r)}{r^2}\frac{(1+\frac{P(r)}{\varepsilon(r)})(1+\frac{4\pi r^3 P(r)}{m(r)})}{1-\frac{2Gm(r)}{r}}, \\ \frac{dm(r)}{dr} &= 4\pi r^2 \varepsilon(r), \end{aligned} \tag{9.9}$$

where ε is the energy density, and P is the pressure.

By varying the central density it is possible to obtain a sequence of masses and radii predicted for the given equation of state. For subnuclear densities the equations of state of Negele–Vautherin (NV) and Bonn have been used. As a result the mass-radius relation can be drawn. It is presented in Fig. 9.3 and 9.4.

The resulting mass-central density relations are presented in Fig. 9.5 and 9.6 whereas, radius-central density relations are given in Fig. 9.7 and 9.8.

The inclusion of the δ meson permits the biggest masses and radii for each parameterization. The smallest masses and radii can be obtained for the G2 parameter set. Neutron star parameters for the maximum mass configurations calculated for the considered models are collected in Table 9.1.

Relative concentrations of protons in neutron star matter are of

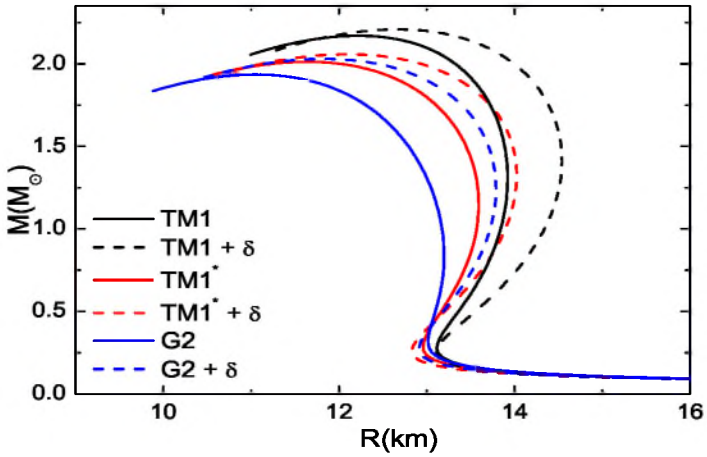

Figure 9.4: The mass-radius relations calculated for TM1, TM1* and G2 equations of state

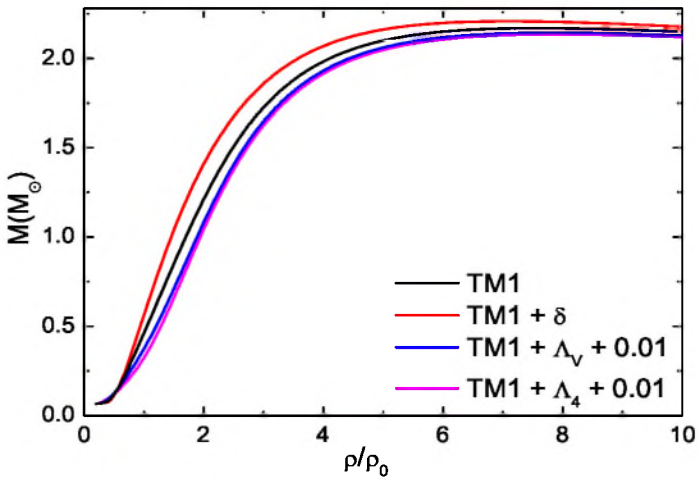

Figure 9.5: Neutron star masses as a function of central density ρ_c for TM1 parameter sets

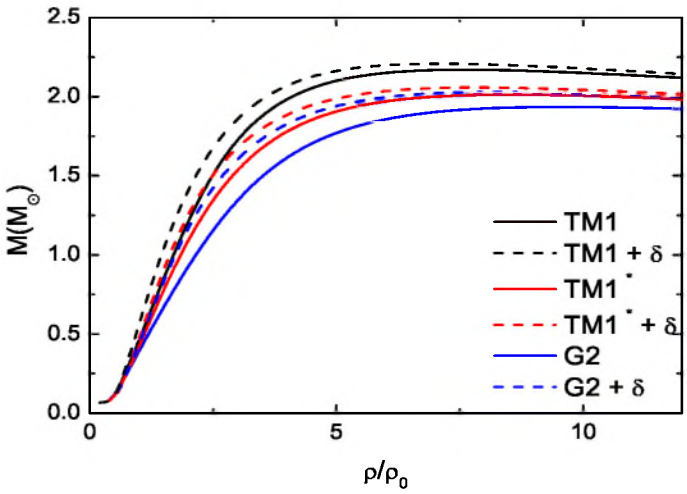

Figure 9.6: The $M - \rho_c$ curves for TM1, TM1* and G2 parameterizations

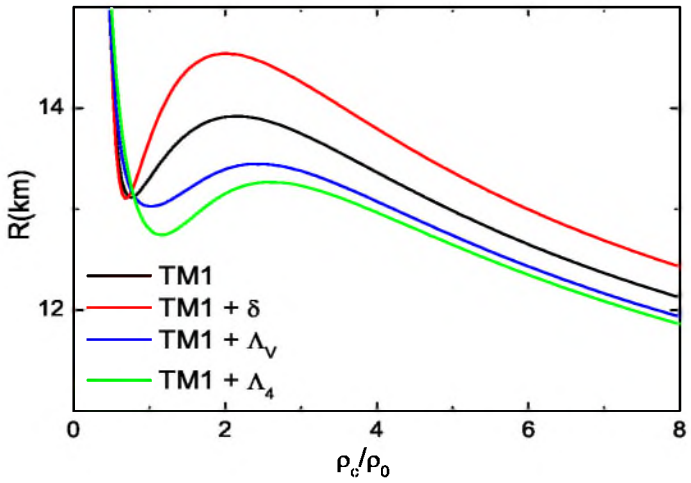

Figure 9.7: Neutron star radii as a function of central density ρ_c The results have been obtained for TM1 parameter sets

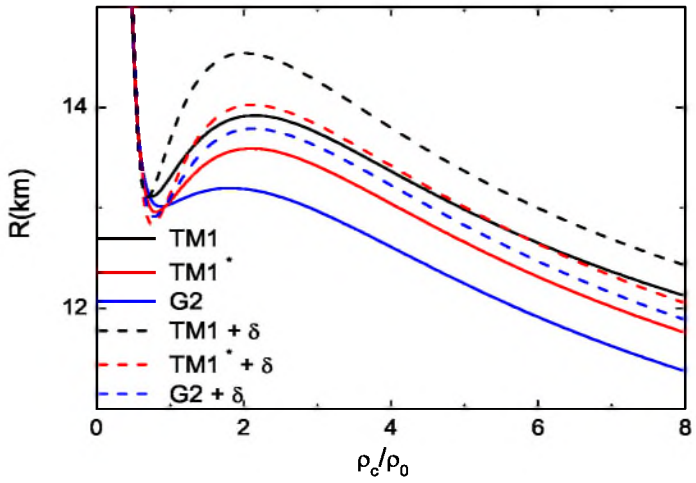

Figure 9.8: Neutron star radii as a function of central density ρ_c for TM1, TM1* and G2 parameterizations

Table 9.1: Neutron star parameters

Parameter set	$M_{max}(M_\odot)$	$M_b(M_{max})(M_\odot)$	R(M_{max})(km)	ρ_c(g/cm^3)
TM1	2.17	2.51	12.21	7.64
TM1+δ	2.21	2.54	12.66	7.12
TM1+Λ_V	2.14	2.52	11.91	7.80
TM1+Λ_4	2.13	2.47	11.88	7.92
TM1*	2.01	2.30	11.60	8.52
TM1*+δ	2.06	2.35	12.11	7.92
G2	1.94	2.23	11.04	9.60
G2+δ	2.03	2.37	11.81	8.32

special interest as it has been shown that if the proton concentration in neutron star matter exceeds the critical value Y_p^{crit}, direct URCA processes can occur [9], [76], [151], [152], [154]. Thus proton concentration in neutron star matter affects the thermal evolution of a neutron star. Direct URCA processes are possible if the Fermi momenta of neutrons, protons and electrons fulfill the so-called triangle inequality $k_{F_n} \leq k_{F_p} + k_{F_e}$. This condition, together with the requirement of charge neutrality allows one to estimate the threshold proton fraction for the direct URCA process (Y_p^{crit}) which is given by the following relation

$$Y_p^{crit} = \frac{1}{1 + (1 + Y_{e,l}^{1/3})^3} \tag{9.10}$$

where $Y_{e,l}$ is defined as $Y_{e,l} = n_e/(n_e + n_\mu)$.

The critical proton concentration is within the range whose lower limit is obtained for the matter without muons ($k_{F_e} < m_\mu$). In this case the proton fraction at the onset of the direct URCA process is $Y_p^{crit} = 0.111$ – the muon free threshold [152]. Including the effect of muons the upper limit of the proton fraction at the level $Y_p^{crit} = 0.148$ – massless muon threshold – can be obtained. The threshold proton concentration Y_p^{crit} occurs at a given density denoted as ρ_{crit} and determines the value of a critical neutron star mass M_{crit} in which proton concentration reaches the level sufficient for the onset of direct URCA process. Results for the considered parameterizations are collected in Table 9.2. For each case the value of density for the threshold proton concentration (Table 9.2) is lower than the maximal central density for the stable stellar configuration. In Fig. 9.9 the relative proton concentrations for TM1 parameterization and its extensions are presented. Whereas the results for G2, TM1 and TM1* are given in Fig. 9.10.

Horizontal lines indicate the position of the critical proton fractions. The presence of the δ meson shifts the onset of the direct URCA process to very low density and thus for very low value of the critical mass M_{crit}. Models with nonlinear couplings Λ_V and Λ_4 lead to the highest value of the ρ_{crit}. The same result is obtained for G2 parameter set. Klahna et al. [152] present the result of the analysis, which is based on the population synthesis and the mass measurement of binary radio pulsars, it sets the limit for the critical mass $M_{crit} > 1.35\,\mathrm{M}_\odot$. If the onset of the direct URCA process occurs at low densities this process will also be allowed for neutron stars with masses smaller than 1.35 $\mathrm{M}_\odot$ and the star will be cooled very efficiently. All the considered models

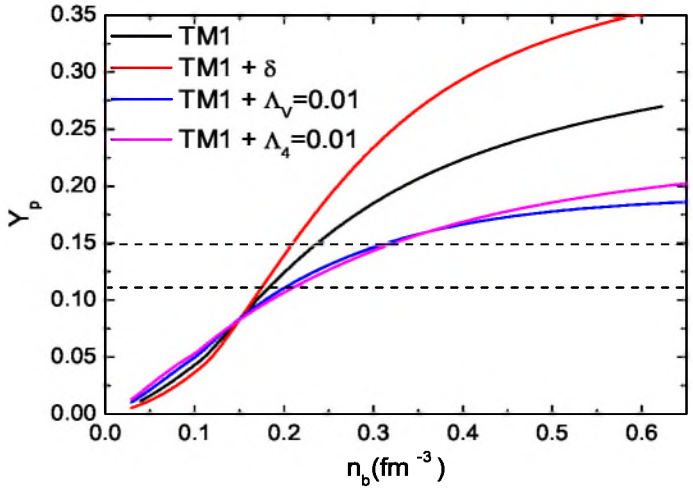

Figure 9.9: Relative concentrations of protons in neutron star matter for the TM1 parameterizations (left panel) and TM1* and G2 parameter sets (right panel)

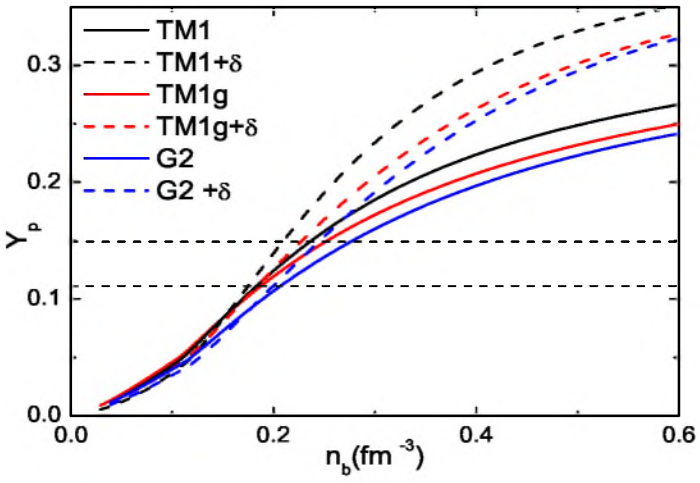

Figure 9.10: Relative concentrations of protons in neutron star matter for the TM1 parameterizations (left panel) and TM1* and G2 parameter sets (right panel)

permit the direct URCA processes. As was pointed out in the paper by Horowitz and Piekarewicz [153] X-ray observations of the neutron star in 3C58 [155], Vela [156] and Geminga [157] as well as the low quiescent luminosity in the transiently accreting binaries KS 1731-260 [158] and Cen X-4 [159], indicate low surface temperature. This may result in enhanced cooling and in the necessity of the direct URCA process occurring. However, there are examples of neutron stars, such as RX J0822-4300 [153], with high surface temperature and thus with cooling mechanisms well described by the modified URCA process. Due to the anisotropy of neutron star surface temperatures their measurements are very difficult. The obtained results also crucially depend on the model of the atmosphere employed.

The threshold proton fraction is determined by the symmetry energy of the considered model. The density dependence of the symmetry energy is still unconstrained and the extrapolation of proton fraction to higher densities is very difficult. Horowitz and Piekarewicz [153] have shown that the predictions for the neutron radius in ^{208}Pb are correlated to the proton fraction in β-equilibrated neutron star matter. Analyzing a wide range of relativistic effective field theory models they found that models which predict a neutron skin in ^{208}Pb of $R_n - R_p < 0.20$ fm lead to a small proton fraction below the limiting value which permits the direct URCA process in 1.4 $M_\odot$ neutron stars. For $R_n - R_p > 0.25$ fm all considered models predict the enhanced cooling of a 1.4 $M_\odot$ neutron star. Calculations performed for the non-relativistic equation of state of Friedman and Pandharipande [160] give too small a proton fraction for URCA cooling to be possible. This equation of state also leads to the neutron skin in ^{208}Pb of $R_n - R_p = 0.16 \pm 0.02$ fm. These two facts-the equilibrium proton fraction and the value of the neutron skin-confirmed the result obtained for the relativistic effective field theory models. As the Parity Radius Experiment at the Jefferson Laboratory uses model independent parity violating electron scattering to measure the neutron radius in ^{208}Pb, the measurement of the neutron radius in ^{208}Pb may be decisive for a given model to permit the direct URCA processes [153].

Analyzing the density dependence of the symmetry energy (Fig. 8.21, Fig. 8.22) and the density dependence of the proton concentrations Y_p in neutron star matter Fig. 9.9 and 9.10 the tendency for a more rapid increase of the proton fraction for models with the stiffest symmetry energy becomes evident. This can also be analyzed by the

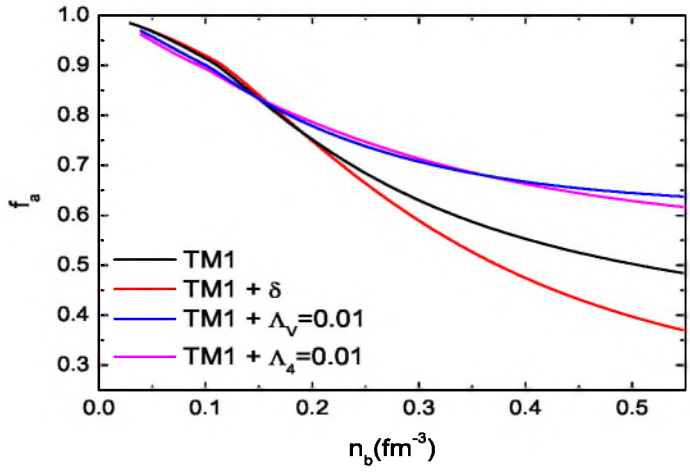

Figure 9.11: The asymmetry parameter f_a for neutron star matter for TM1 parameter set and its extensions

density dependence of the isospin asymmetry parameter f_a in neutron star matter. This parameter is related to the proton fraction Y_p through the relation $f_a = 1 - 2Y_p$. Results are depicted in Fig. 9.11 and 9.12. The parameter f_a takes the lowest value when the δ meson is included.

The equilibrium proton fraction Y_p is directly connected with the electron concentrations Y_e. Fig. 9.13 and 9.14 presents the electron concentrations for the considered model. Calculations performed with the δ meson give a relatively high electron fraction, whereas G2 parameterization and the presence of nonlinear couplings Λ_V and Λ_4 lead to models with reduced electron concentrations.

For the sake of completeness the result obtained by Engvik [105] et. al. should be presented. As was shown in their paper using various new nucleon-nucleon potentials they obtained the symmetry energy which increases with density. This influences the proton fraction in β-stable matter. For the CD-Bonn potential the direct URCA process can occur at a density of 0.88 fm^{-3}, for the Nijm I it starts at 1.25 fm^{-3}, for the Reid93 the critical density is reached at 1.36 fm^{-3}. The Argonne potential allows the direct URCA process at a density of 1.05 fm^{-3}. For the Nijm II the onset of this process is shifted to a very high density above 1.5 fm^{-3}.

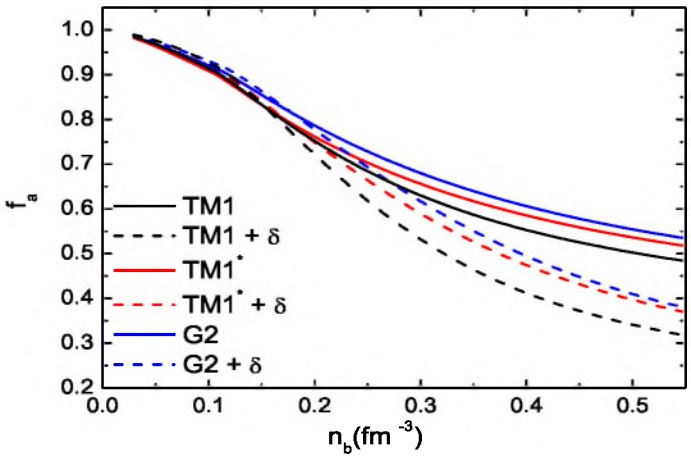

Figure 9.12: The asymmetry parameter f_a for neutron star matter for TM1, TM1* and G2 parameter sets. For comparison the influence of δ meson is also presented

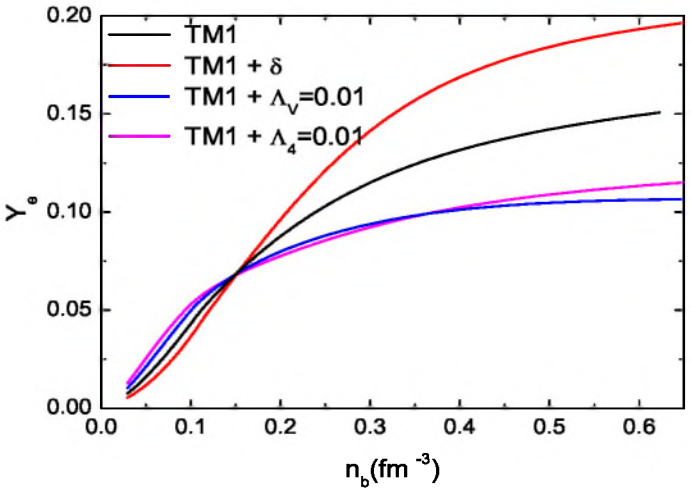

Figure 9.13: Relative concentrations of electrons for TM1 parameter sets

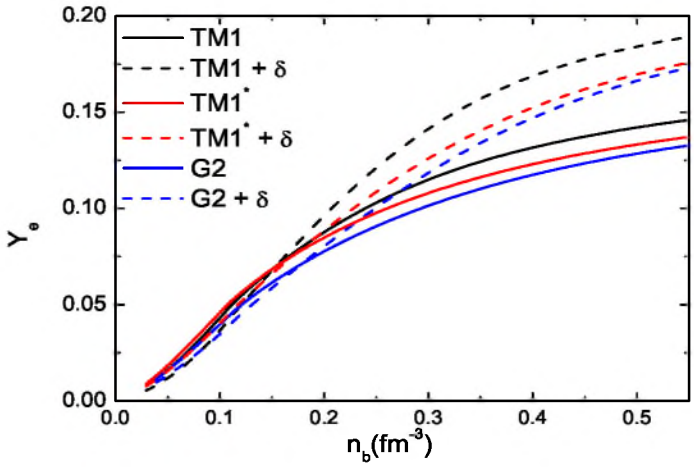

Figure 9.14: Relative concentrations of electrons for TM1, TM1* and G2 parameter sets

Table 9.2: Neutron star parameters for the threshold proton concentrations

Parameter set	n_b(URCA)(fm^{-3})	ρ_c/ρ_0(URCA)	M(URCA)(M$_\odot$)
TM1	0.235	1.65	0.99
TM1+δ	0.207	3.65	2.01
TM1+Λ_V	0.303	2.17	1.19
TM1+Λ_4	0.314	2.29	1.24
TM1*	0.247	1.75	0.95
G2	0.273	1.95	0.91

Chapter 10

Strange neutron star matter

The softening of the EOS with density strongly suggests the presence of the exotic high density phase - the strange matter. Analysis of the properties of neutron star matter with hyperons has been performed for the same selected parameter sets as in the previous section. Thus there are TM1 parameter set, supplemented with the nonlinear terms Λ_V and Λ_4, and G2 and TM1* parameterizations. The parameters of the considered models now are extended by the hyperon-meson coupling constants. Parameters are collected in Table 8.4 and 8.5. In the scalar sector the scalar coupling of the Λ and Ξ hyperons requires constraining in order to reproduce the estimated values of the potential felt by a single Λ and a single Ξ in saturated nuclear matter. The influence of the strength of the hyperon coupling constants has been investigated twofold by analyzing the change of the chemical composition and by comparing the hydrostatic structure of neutron stars. The appearance of hyperons significantly affects the equilibrium composition of neutron star matter. The analysis of the neutron stars chemical compositions starts from the presentation of proton concentrations for the chosen models which is a decisive factor in creating the neutron star cooling rate. The results are depicted in Fig. 10.1 and 10.2. The considered models lead to very similar proton fractions for lower densities. The onset of hyperons changes this situation. The TM1, TM1* and G2 models with strong hyperon-hyperon interaction give rather high concentrations of protons. The inclusion of the nonlinear meson terms Λ_V and Λ_4 in both cases very efficiently reduces proton concentration (Fig. 10.1). The dotted lines indicate the values of the critical proton concentrations. The obtained proton profiles in the case of TM1 para-

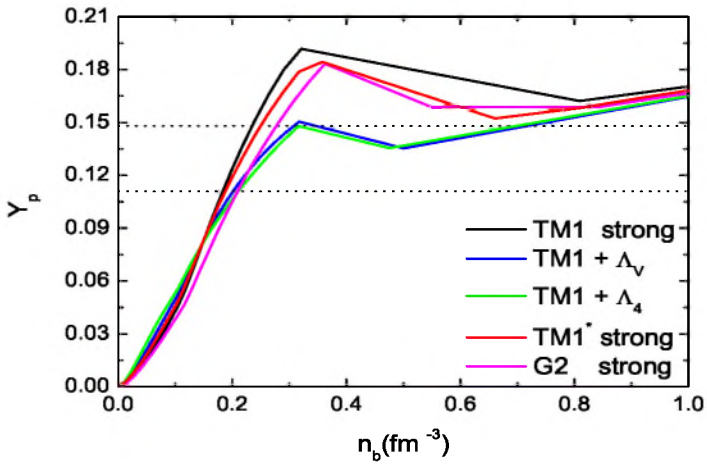

Figure 10.1: The relative concentration of protons for TM1 parameter sets and for G2 and TM1* models. The straight, dotted lines show the threshold proton concentrations

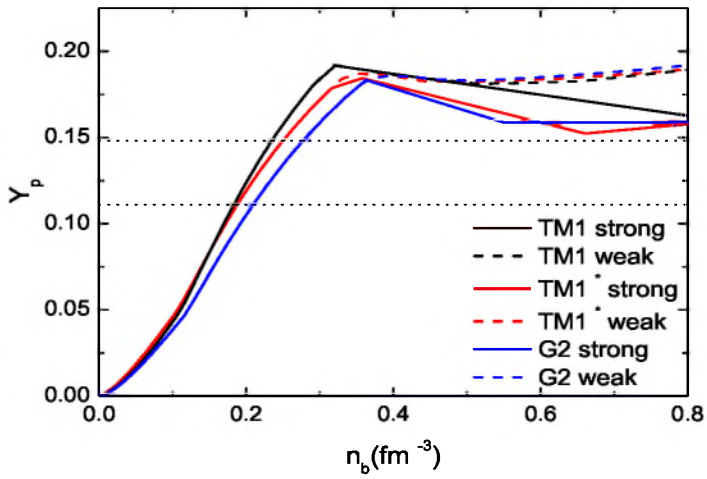

Figure 10.2: The relative proton concentrations for the strong and weak $Y-Y$ coupling for TM1, TM1* and G2 parameter sets. The dashed lines represent the cases for the weak $Y-Y$ coupling. The straight, dotted lines show the threshold proton concentrations

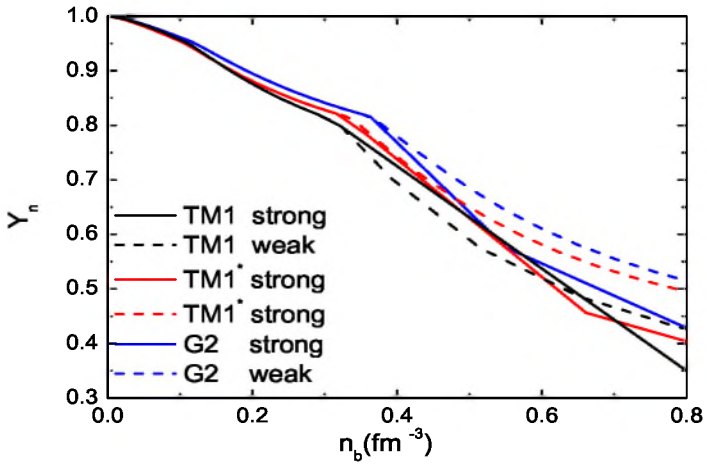

Figure 10.3: The relative concentration of neutrons for neutron star matter obtained for TM1 parameter set and its extensions and for the G2 and TM1* models

meter sets with the nonlinear Λ_V and Λ_4 terms, for densities up to $\sim 5\rho_0$ lie below the level of Y_p^{crit}, which denotes the threshold proton concentration for the onset of the direct URCA process. It is also possible to make the comparison between the calculations made for the considered parameterizations taking into account the strong and weak hyperon-hyperon couplings. The results obtained for TM1 parameter sets (strong and weak) and for G2 and TM1* are presented in Fig. 10.2. Models with weak hyperon-hyperon interactions lead to higher proton fractions. Among the models presented in this figure G2 parameter set gives the lowest content of protons. Neutrons are the major component in the presented models at low and moderate densities. Neutron concentrations for the presented parameterizations are depicted in Fig. 10.3 and 10.4. There are parameterizations which at sufficiently high density lead to the situation when Λ hyperons are more abundant than neutrons. This case is carried out for TM1 parameter set with the strong hyperon-hyperon interaction. In Fig. 10.5 the equilibrium composition for this parameterization is presented. For comparison the equilibrium baryon concentration for G2 parameter set is depicted in Fig. 10.6. In the case of G2 model the concentration of Λ hyperons is higher then neutron concentration for very high densities.

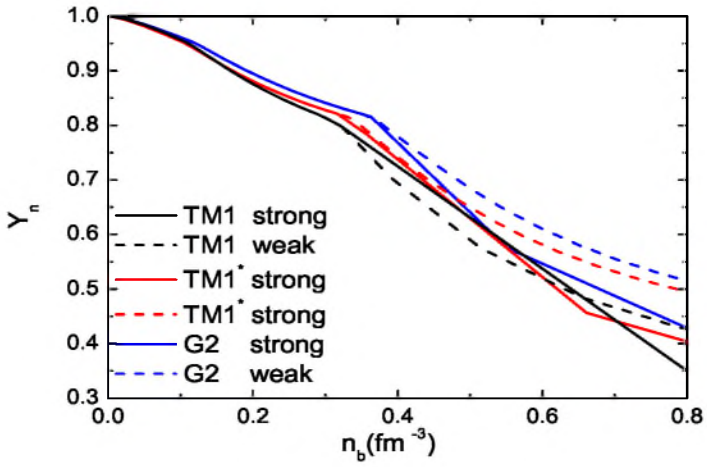

Figure 10.4: The relative concentration of neutrons in neutron star matter. This figure includes results for TM1, TM1* and G2 parameter sets for strong and weak hyperon-hyperon interactions

The composition of hyperon star matter as well as the the threshold density for hyperons, is altered when the strength of the hyperon-hyperon interaction is changed and when the nonlinear meson interaction terms are present. The appearance of hyperons follows from the chemical potential relations. Figures 10.7, 10.8, 10.9, 10.10, 10.11 and 10.12 show relative fractions of particular strange baryon species YB_i ($i = \Lambda, \Xi^-, \Xi^0$) as a function of baryon number density n_b for the chosen parameterizations. All calculations have been done under the assumption that the repulsive Σ interaction shifts the onset points of Σ hyperons to very high densities and that they do not appear in the considered neutron star models. In the presented figures the results for TM1 parameter sets and for TM1* and G2 are given. For comparison the analysis of the influence of the hyperon-hyperon interaction strength has been included. Dashed lines in Fig. 10.8, 10.9 and 10.12 represent the concentrations of baryons for a weak Y – Y interaction. In these cases there is a substantial reduction of the Λ hyperon population in comparison with the case of a strong Y – Y interaction. The appearance of nonlinear meson interaction terms also lowers the Λ concentration in neutron star matter. Λ is the first strange baryon that

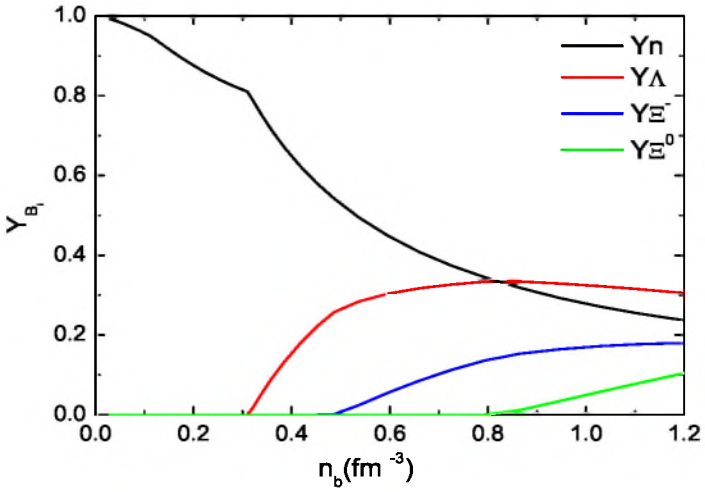

Figure 10.5: The equilibrium baryon concentrations. Result obtained for TM1 parameter set with the strong hyperon-hyperon interaction

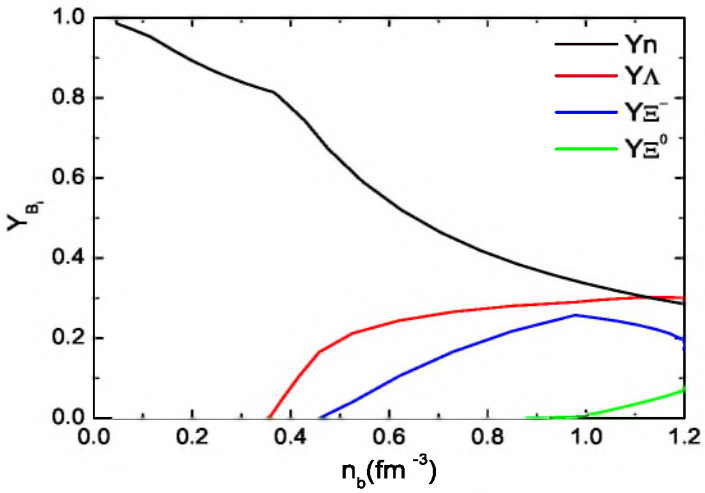

Figure 10.6: The equilibrium baryon concentrations for G2 parameter set with the strong hyperon-hyperon interaction

emerges in hyperon star matter, it is followed by Ξ^- and Ξ^0 hyperons. The presence of nonlinearities very efficiently reduces the population of Ξ^- hyperons in neutron star matter. The TM1 parameterization without nonlinearities for the strong Y – Y interaction gives the highest fraction of Ξ^- hyperons. Comparing the results for the strong and weak models one can see that weak models enhance the populations of Ξ^- hyperons.

Nonlinear terms significantly affect the onset points of Ξ^0 hyperons shifting them to lower densities. The population of Ξ^0 hyperons is enhanced in this case. The result obtained with the use of TM1* parameterization leads to neutron star matter with substantially reduced Ξ^0 hyperon fraction. The models with the weak Y – Y interaction also give lower populations of Ξ^0 hyperons.

In Fig. 10.13 and 10.14 the electron profiles in neutron star matter are presented. From these figures it is evident that lepton populations are altered not only by the change of strength of hyperon coupling constants but also by the isospin dependent nonlinearities which determine the symmetry energy of the system. A very special aspect of the existence of hyperons is the intrinsic deleptonization of neutron star matter. First the appearance of Λ hyperons stops the increase in the lepton population and additionally when negatively charged Ξ^- hyperons emerge further deleptonization occurs. Thus the charge neutrality can be guaranteed with the reduced lepton contribution.

The relative hadron-lepton compositions in the presented models can be also analyzed through the density dependence of the asymmetry parameter f_a which describes the neutron excess in the system and the parameter $f_s = (N_\Lambda + 2N_{\Xi^-} + 2N_{\Xi^0})/n_b$ which is connected with the strangeness content. Fig. 10.15, 10.16, 10.17 and 10.18 present both parameters as functions of the baryon number density. As the density increases, the asymmetry of the matter decreases and the strangeness contents f_s increases for all the considered cases.

The values of electron chemical potentials are shown in Fig. 10.19 and 10.20.

The calculated EOS for the chosen parameter sets are presented in Fig. 10.21 and 10.22. Fig. 10.21 compares the respective equations of state for TM1 parameter set, its extensions by the nonlinear meson interaction terms and TM1* and G2 parameterizations. All these EOS have been calculated for the strong hyperon-hyperon interaction. There are qualitative differences between the presented equations.

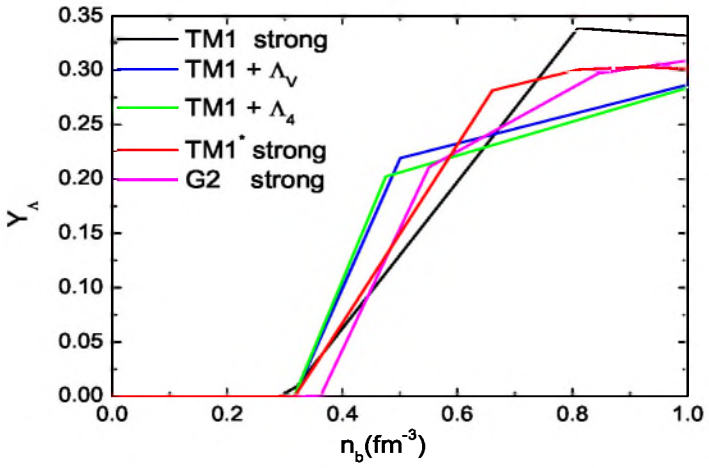

Figure 10.7: The relative concentration of Λ hyperons for β-equilibrated neutron star matter for TM1 parameter set and its extensions

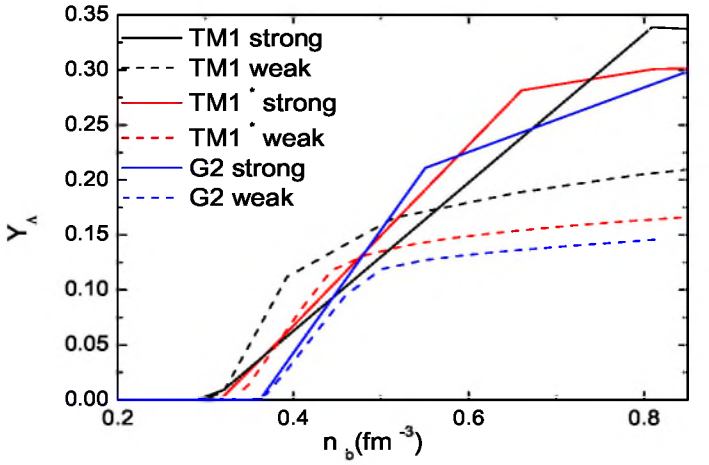

Figure 10.8: The relative concentration of Λ hyperons for β-equilibrated neutron star matter for TM1, TM1* and G2 parameter sets. The dashed lines represent the cases for the weak $Y-Y$ interaction

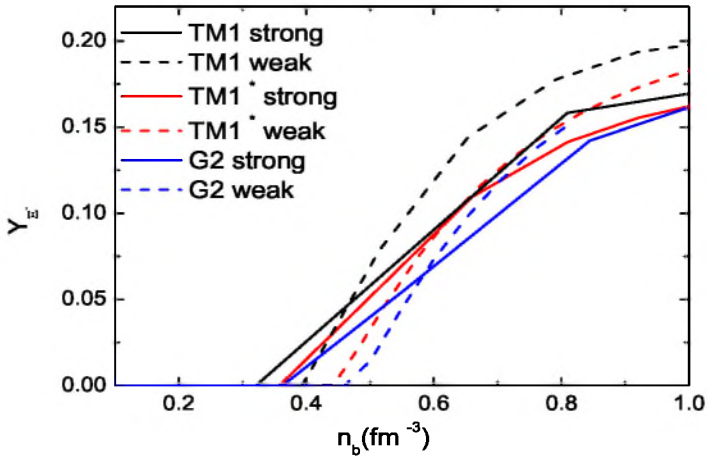

Figure 10.9: The relative concentration of Ξ^- hyperons for neutron star matter. The results for TM1 parameter set and its extensions are presented. The dashed lines represent the cases for the weak $Y-Y$ interaction

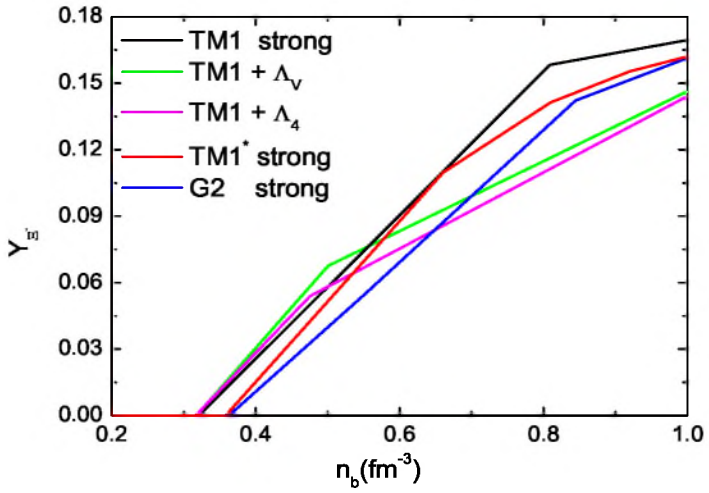

Figure 10.10: The relative concentration of Ξ^- hyperons for neutron star matter for TM1, TM1* and G2 parameter sets

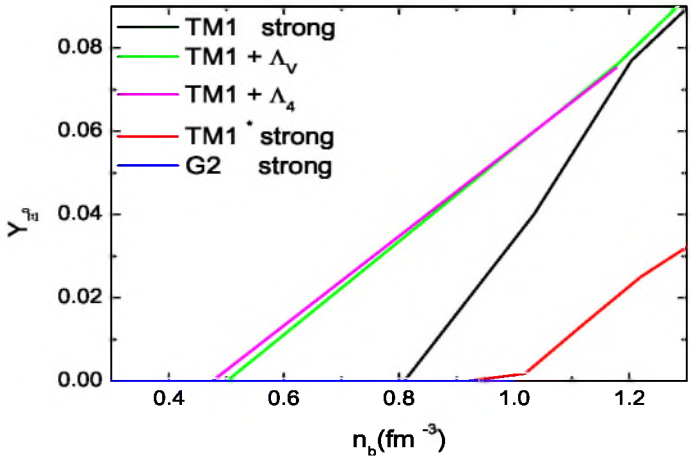

Figure 10.11: The relative concentration of Ξ^0 for neutron star matter for TM1 parameter set and its extensions are presented

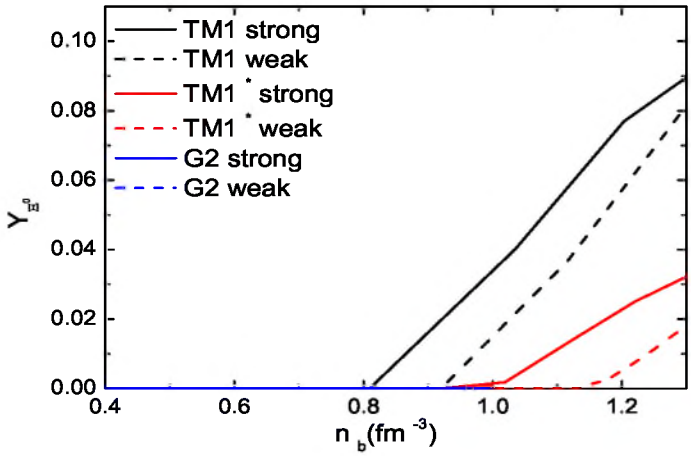

Figure 10.12: The relative concentration of Ξ^0 for neutron star matter. The results for TM1, TM1* and G2 parameter sets. The dashed lines represent the cases for the weak $Y-Y$ interaction

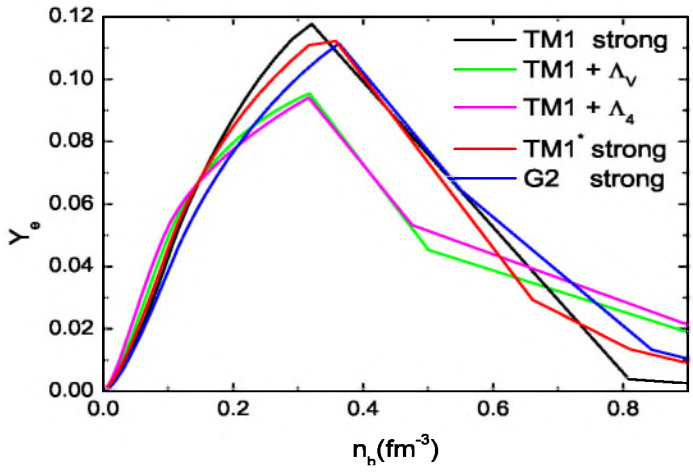

Figure 10.13: The relative concentration of electrons for neutron star matter for TM1 parameter set and its extensions

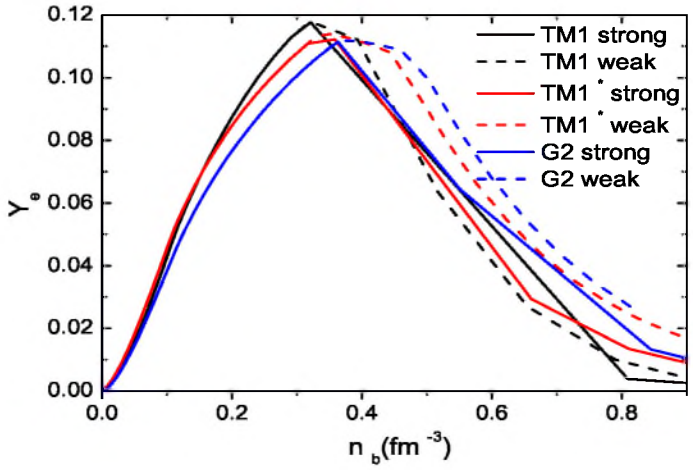

Figure 10.14: The relative concentration of electrons for neutron star matter. This figure includes results for TM1, TM1* and G2 parameter sets. The dashed lines represent the cases for the weak $Y - Y$ interaction

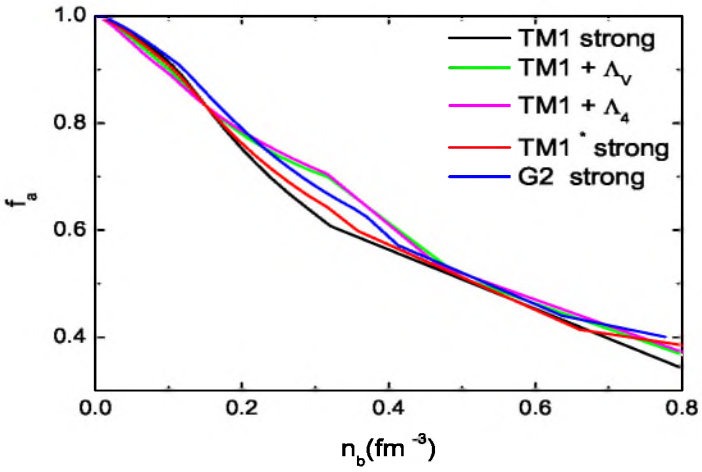

Figure 10.15: The asymmetry parameter f_a for neutron star matter the results for TM1 parameter set and its extensions

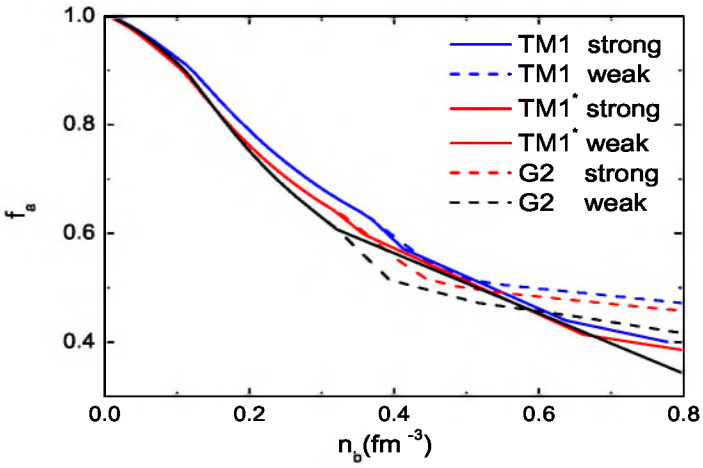

Figure 10.16: The asymmetry parameter f_a for neutron star matter for TM1, TM1* and G2 parameter sets. Dashed lines represent the cases for the weak $Y-Y$ interaction

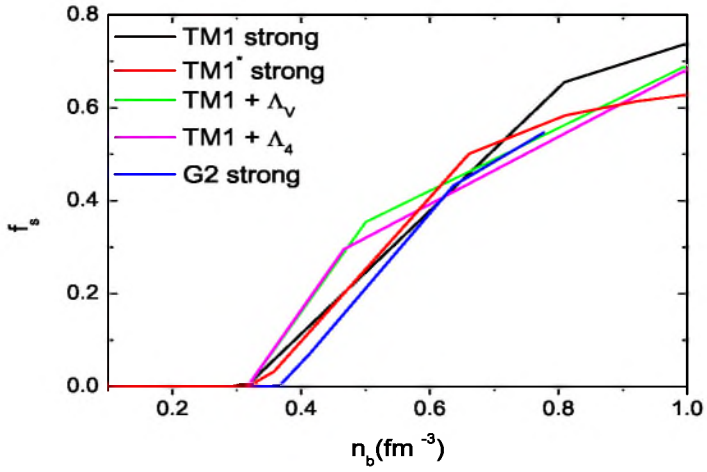

Figure 10.17: The strangeness content f_s for neutron star matter for TM1 parameter set and its extensions

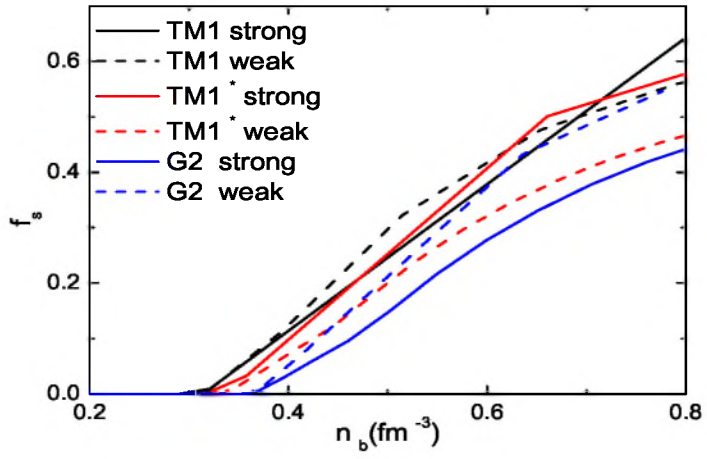

Figure 10.18: The strangeness content f_s for neutron star matter for TM1, TM1* and G2 parameter sets. Dashed lines represent the cases for the weak $Y-Y$ interaction

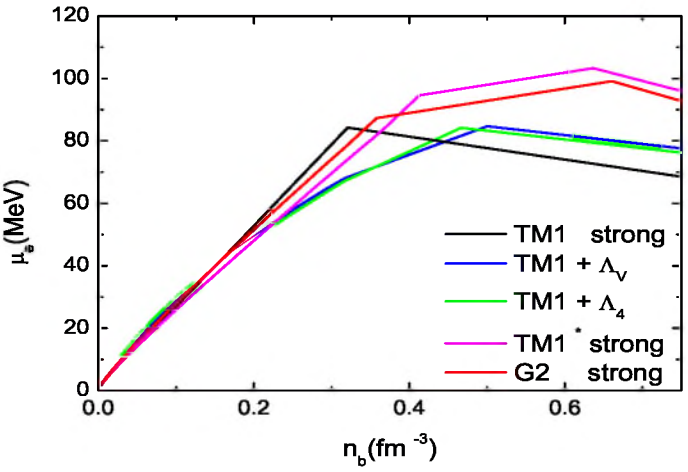

Figure 10.19: The electron chemical potentials for neutron star matter for TM1 parameter set and its extensions are presented

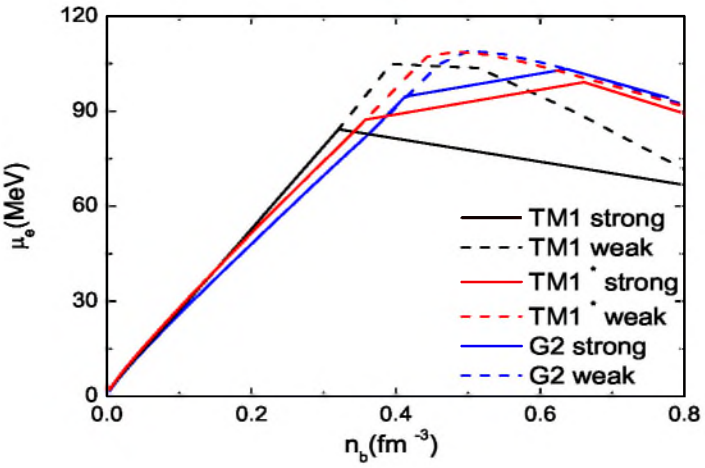

Figure 10.20: The electron chemical potentials for neutron star matter for TM1, TM1* and G2 parameter sets. Dashed lines represent the cases for the weak $Y-Y$ interaction

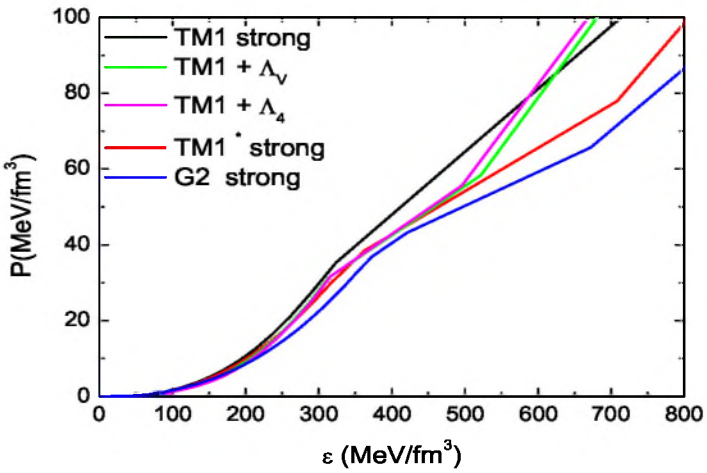

Figure 10.21: Equations of state for TM1 strong and weak models and TM1 models with nonlinear terms

As it is well known the main effect caused by the presence of hyperons in neutron star matter is the softening of the EOS. The EOS of the strong Y – Y coupling model for TM1 parameterization without nonlinearities over some density ranges is stiffer than those which include nonlinear terms. The EOS obtained for TM1* model has the same energy density dependence as those for TM1+Λ_V and TM1+Λ_4 parameter sets till the energy density ε reaches the value $\sim$ 500 MeV fm^{-3}. Starting from this point the equations TM1+Λ_4 and TM1+Λ_V become significantly stiffer than TM1 and TM1* ones.

The equations of state presented in Fig. 10.22 have been obtained for the weak and strong TM1, TM1* and G2 parameterizations. The TM1* and G2 models give the softest equations of state. Thus one can conclude that the influence of the strength of hyperon-nucleon and hyperon-hyperon interactions is strongest for G2 and TM1* models.

Solutions of the Oppenheimer-Tolman-Volkoff equation for the considered equations of state are presented in Fig. 10.23 and 10.24.

The obtained mass-radius relations are constructed for neutron star matter with hyperons and then compared with the mass-radius relation for non-strange matter. The inclusion of nonlinear meson interaction terms only slightly lowers the values of the maximum mass, but significantly reduces the radii of the maximum mass configurations.

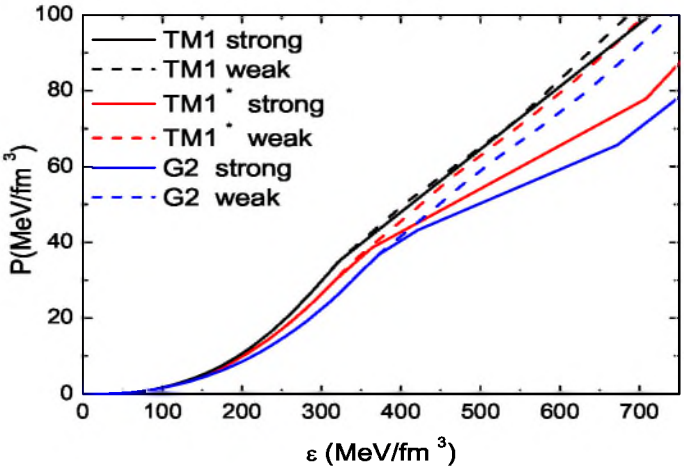

Figure 10.22: Equations of state for TM1, TM1* and G2 parametrizations. Dashed lines represent the cases for the weak $Y - Y$ coupling

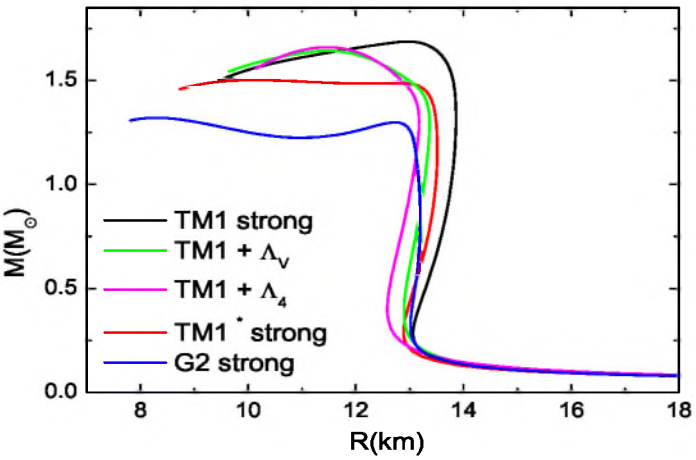

Figure 10.23: The mass-radius relations for TM1 strong and weak models and the TM1 models with nonlinear terms

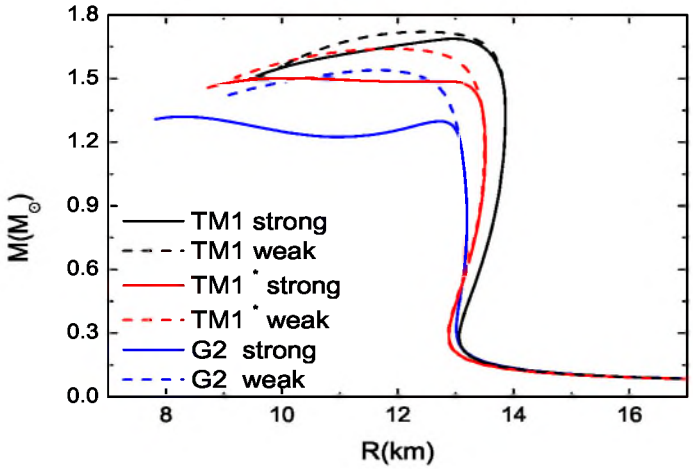

Figure 10.24: The mass-radius relations for TM1, TM1* and G2 parametrizations. Dashed lines represent the cases for the weak $Y-Y$ coupling

The key difference between TM1 and TM1* and G2 mass-radius diagrams is found in the results obtained for the strong hyperon-hyperon interaction. In the case of TM1* and G2 parameter sets apart from the ordinary stable neutron star branch there exists the additional stable branch of solutions which are characterized by a similar value of masses but with significantly reduced radii. The second stable sequence of solutions is absent in the case of the weak hyperon-hyperon coupling. These parameter sets give larger maximum masses.

In Fig. 10.25 and 10.26 the mass-central density relations are shown, whereas Fig. 10.27 and 10.28 depict the radius as a function of central density for the model considered. The comparison of the maximum mass configurations obtained for the weak and strong Y – Y couplings makes possible the estimation of the role of the hyperon-hyperon interaction strength. The strong model in comparison with the non-strange solutions gives the reduced value of the maximum mass. The mass reduction is the most pronounced for G2 parameterization and is lower for the standard TM1 parameter set. The influence of the strength of the hyperon-nucleon couplings has been analyzed for a very limited range of the $g_{\sigma\Lambda}$ parameter strictly connected with the value of the potential felt by a single Λ hyperon in saturated nuclear matter.

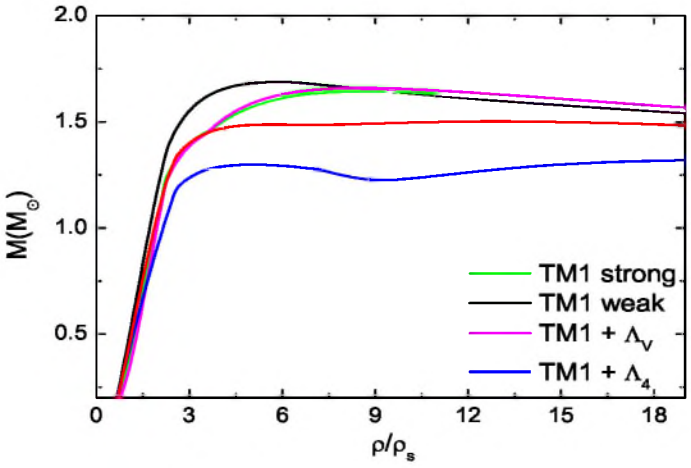

Figure 10.25: The mass-central density relations for the TM1 strong and weak models and for the TM1 models with nonlinear terms

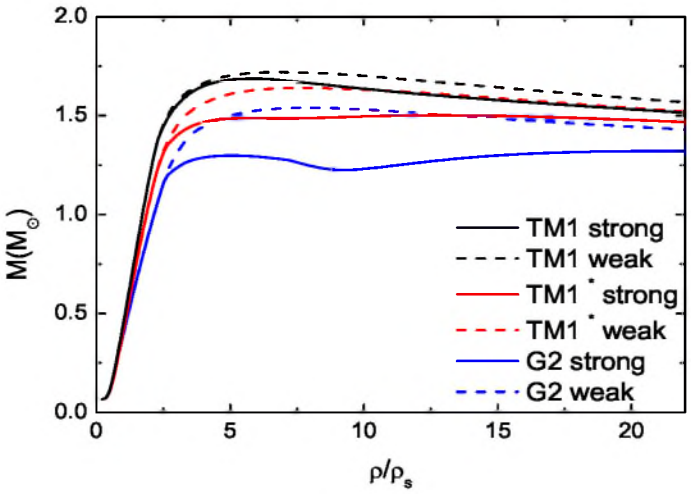

Figure 10.26: The mass-central density relations for the TM1, TM1* and G2 parameterizations are presented. Dashed lines represent the results obtained for the weak $Y-Y$ coupling

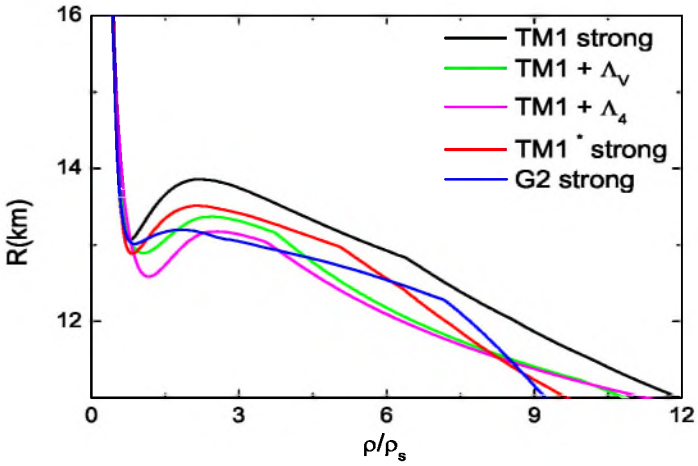

Figure 10.27: The radius-central density relations for the TM1 strong and weak models and for the TM1 models with nonlinear terms

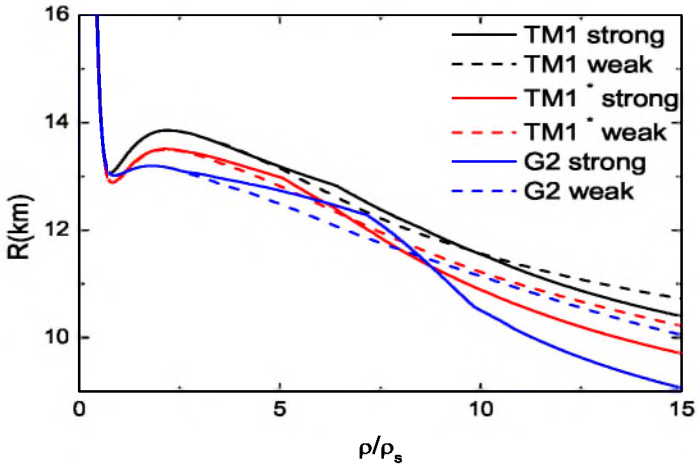

Figure 10.28: The radius-central density relations for the TM1, TM1* and G2 parameterizations are presented. Dashed lines represent the results obtained for the weak $Y - Y$ coupling

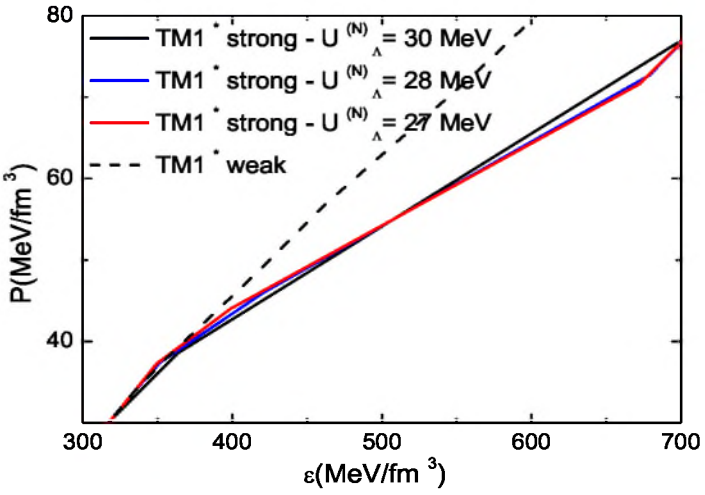

Figure 10.29: Equations of state for the TM1* strong model for different values of the $U_\Lambda^{(N)}$ potentials

The chosen values of this potential: -27 MeV, -28 MeV, -30 MeV lead to the following $g_{\sigma\Lambda}$ parameters: 9.203, 9.158, 9.054. The equations of state calculated for the selected values of the $U_\Lambda^{(N)}$ potentials for TM1* model are given in Fig. 10.29. In Fig. 10.30 the mass as a function of the central density for $U_\Lambda^{(N)} = -27, -28$ and -30 MeV is depicted. Particular curves are labelled by the three chosen values of the $U_\Lambda^{(N)}$ potential.

There are two maxima on each curve which correspond to the maximum masses of the two stable sequences of solutions on the mass-radius diagram. The height of each maximum depends on the value of $U_\Lambda^{(N)}$ potential. The second maximum is higher than the one which corresponds to the ordinary neutron star for the weakest hyperon-nucleon interaction strength.

The conditions under which the quark matter occurs in neutron star interiors, thus permitting the formation of stable hybrid star configuration, have been established in order to make the analysis more complete. Two phases of matter have been compared: the strange hadronic matter and quark matter. The phase with the highest pressure (lowest free energy) is favored.

Dashed curves show the quark matter EOS for two fixed values of

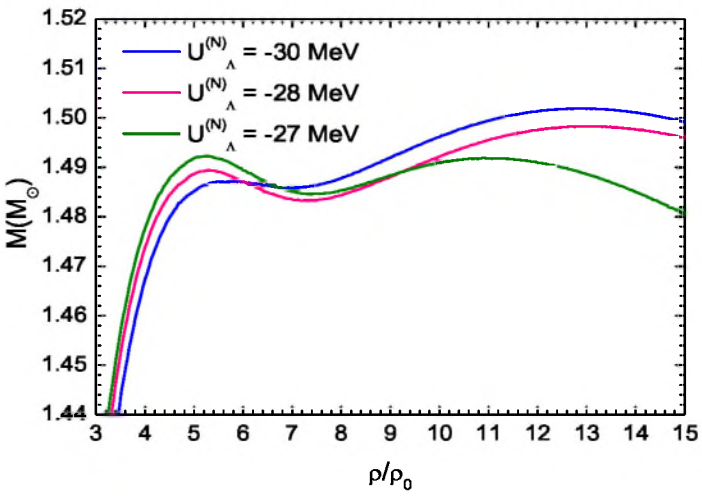

Figure 10.30: The mass-central density relations for different values of the $U_{\Lambda}^{(N)}$ potential

the bag parameter: $B^{1/4} = 150$ MeV and $B^{1/4} = 171$ MeV (B_{crit}). The influence of hyperons is considered for the weak and strong Y – Y couplings. In Fig.10.31 apart from the EOS calculated for TM1 and TM1* parameter sets the EOS of the quark matter, obtained with the use of the quark mean field model [161] with the direct coupling of the bag parameter to the scalar meson fields s_0 and s_0^*, is also included.

The results strongly depend on the value of the bag parameter. There exists the limiting value of $B_{crit}^{1/4} = 171$ MeV. For $B > B_{crit}$ there is no quark phase in the interior of a neutron star. The bag parameters $B < B_{crit}$ lead to the intersection of the quark matter equation of state and that of hyperon star matter with the strong Y – Y interactions. Thus a hybrid star with a quark phase inside can be constructed.

For the purpose of this dissertation, A denotes the maximum mass configuration of the ordinary neutron star branch, whereas B, denotes the additional maximum. The obtained mass-radius relation for hybrid stars involving quark matter is presented in Fig. 10.32 (for $B^{1/4} = 150\,MeV < B_{crit}^{1/4}$).

The maximum hybrid star mass is of about $1.52\,\mathrm{M}_{\odot}$ and is greater than the maximum mass of the very compact additional stable branch

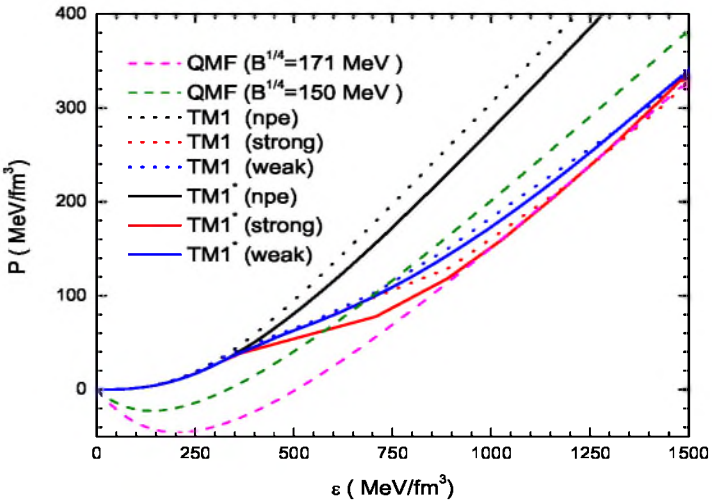

Figure 10.31: The EOS calculated for TM1 and TM1* parameter sets. Dotted curves represent the results obtained for TM1 parameter set. The case of non-strange baryonic matter is marked by npe. Dashed curves show the quark matter equations of state

configurations (B). The radius of the hybrid star maximum mass configuration is also greater than that of the configuration marked as B.

This very brief analysis of the possible existence of the mixed quark-hadron phase inside a neutron star shows that due to remaining uncertainties about the parameters of the quark star model, especially the bag constant, the construction of the equation of state of the quark phase introduces some freedom in interpreting the results. The additional nonlinear meson-meson interaction terms together with the strong hyperon-hyperon coupling create the necessary conditions for the existence of the second branch of stable neutron star configurations. The composition of hyperon star matter as well as the threshold density for hyperons are altered when the hyperon-nucleon interaction strength is changed. Fig. 10.33 presents fractions of particular baryon species Y_B and leptons as a function of the density ρ for the strong model of TM1* parametrization. Extension of presented models to higher density required an extrapolation. This leads to some uncertainties and suffers of several shortcomings.

The standard TM1 parameter set for high density range reveals an instability of neutron star matter connected with the appearance of a

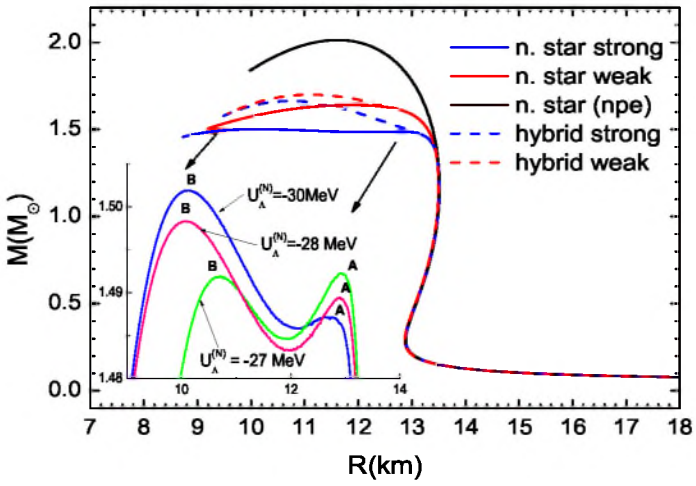

Figure 10.32: The mass-radius relations for TM1* parametrization

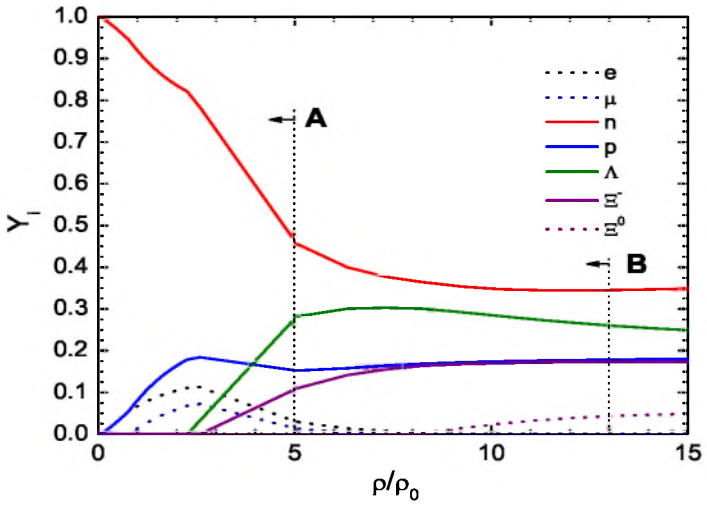

Figure 10.33: Baryon and lepton concentrations in neutron star matter as a function of the density ρ ($\varepsilon = \rho c^2$) where ε denotes the energy density, for TM1* parametrization

negative effective mass due to the presence of hyperons. The nonlinear models which are based on the effective field theory, for parameter sets G2 and TM1* exemplifies an alternative version of the Walecka model which improves the behavior of the baryon effective masses. It also influences the value of the incompressibility K of neutron star matter. The nonlinear meson interaction terms effectively introduces the density dependence of the scalar and vector coupling constants and makes possible to construct neutron star models for very high densities.

Chapter 11

Astrophysical constraints on the equation of state

The attractiveness of neutron star observations consists in their offering solutions to certain fundamental problems of physics. These include information concerning strong gravitational fields and the equation of state of matter at supranuclear densities. Another aspect of neutron star observations concerns the problem of thermonuclear burning and its propagation in degenerate matter. This is closely connected with the phenomena of classical novae and Type Ia supernovae [165]. Observations of neutron stars which allow measurements of their parameters can provide constraints on the form of the equation of state and thereby improve our understanding of matter at extreme pressure and density. As neutron star masses and radii are parameters which are in direct relation to the EOS, the knowledge of their values enables us to determine the essential details concerning the constituents of a neutron star core.

The most general constraints on neutron star masses are imposed by theoretical models which describe the evolutionary progress of stars, especially their final phases. The standard scenario for a neutron stars predicts their formation in the type II supernova explosions. Thus, there exists a theoretical, very rough limitation on neutron star masses arising from the fact that the mass of the collapsing core of a massive star has to be equal to the Chandrasekhar limit of 1.4 $M_\odot$ which corresponds to the neutron star gravitational mass greater then about 1.2 $M_\odot$ [9]. Detailed calculations of massive pre-supernova models indicate that the value of their core masses are of the order of 1.3 - 1.8 $M_\odot$ [10]. Rhoades and Ruffini in their paper [162] made some general assump-

tions concerning the problem of the maximum allowed mass of a neutron star. These assumptions put certain limits on the value of the maximum masses and establish particular correlations between neutron star masses and radii.

The first constraint is based on the correctness of general relativity as a theory of gravity. Buchdahl [163, 164] in his paper has pointed out the existence of the limiting value of GM/Rc^2 for any static neutron star satisfying the Tolman–Oppenheimer–Volkoff equation of hydrostatic equilibrium. In this case the assumption about the finite value of the central pressure P_c leads to the well-known limit on neutron star parameters which is given by the relation $GM/Rc^2 < 4/9$.

The second constraint is connected with the requirement of the stability of matter against local spontaneous collapse (Le Châtelier's principle) [2]. This is satisfied when the equation of state fulfils the condition $dP/d\rho \geq 0$. The causality condition $dP/d\rho \leq c^2$ (that is the speed of sound is less than the speed of light in neutron star matter) also has to be satisfied imposing another limitation on neutron star masses and radii [9].

The EOS which satisfies the above constraints has to match continuously to the known low-density EOS which properly describes properties of nuclear matter.

The general, theoretical assumptions connected with the existence of the maximum neutron star mass are the factors which limit the available nuclear equations of state. However, very large classes of equations of state are still allowed. Other much tighter constraints have to be imposed on neutron star masses and radii in order to limit the equations of state more severely. These additional limitations are based on neutron star observations.

Our knowledge of neutron star parameters can be mainly inferred from observations of X-ray binaries, binary radio pulsar systems or quasi-periodic oscillations in luminosity in low-mass X-ray binaries [166].

In the case of binary radio pulsar systems some estimations of the masses stem from measurements of relativistic orbital effects, whereas the others are indirectly evaluated. As far as radio pulsars are concerned, earlier mass measurements have been consistent with the value $1.35 \pm 0.04\,\mathrm{M}_\odot$ [180]. There is no evidence of the occurrence of extensive mass accretion in these systems [167]. Recent observations have found neutron star masses in double neutron stars systems lie in the

range 1.18 to 1.44 $M_\odot$. Neutron stars in circular neutron star-white dwarf binaries may have larger masses but the uncertainties are larger [168].

X-ray pulsars are accretion powered neutron stars. The measured neutron star masses in such binary systems cover a much wider range 1.1-1.5 $M_\odot$ [167]. There is evidence for a few more massive neutron stars [168, 169].

According to the mass of the companion star (M) X-ray binaries can be divided into two categories: low-mass X-ray binaries (LMXB) for which the mass companion is $M < 1\,M_\odot$ and high-mass X-ray binaries with the companion of the mass $M > 5\,M_\odot$ [170], [166]. For these two classes of binary systems, both the accretion and strength of magnetic field are different. There are different on neutron star parameters constraints which stem from observations of X-ray binaries. One of them is connected with the mass measurements from observations of radial velocity curves [166], [170]. The measurements of relativistic orbital effects in binary systems allow very precise determination of neutron star masses [166]. Through the Doppler effect the velocity variations of the members of binary systems are reflected as wavelength changes in the features of the combined spectrum or periodic shifts of pulse frequency when the observed star is a pulsar. In the case of accreting binaries due to the compact nature of these systems motions transverse to the line of sight are undetectable and only the line of sight components of the motion can be observed. The measurements of Doppler shifts from one member of the binary allow one to reveal details about the nature of the stars and their orbits and to construct the mass function f in the following form [166]

$$f \equiv \frac{P v_1^3}{(2\pi G)} = \frac{(m \sin i)^3}{(M+m)^2}, \tag{11.1}$$

where M and m are the masses of the two stars in the binary system, and i is the inclination of the orbit.

Observation of one star sets constrains on the mass of the second star in a binary system. Thus if the measured values are: the period P of the orbit and the velocity semiamplitude v_1 of the star 1 with mass M, the mass function (11.1) indicates the lower limit of the mass of the star 2. When the mass of the companion is low ($M \ll m$) the mass function can be written in the approximated form $f \approx m \sin i^3$ and the constraint imposed on the neutron star mass depends only on the

uncertainty in determining the value of the inclination. For high mass of the companion ($M \gg m$) the mass function is low and this makes the problem of constraining the neutron star mass very difficult.

The mass measurements in the case of double neutron star systems are the most precise ones. The measured masses in these systems indicate a rather narrow range of neutron star masses between $1.33 - 1.45\,\mathrm{M}_\odot$ with the maximum mass $\sim 1.5\,\mathrm{M}_\odot$ [171]. The obtained results can be affected by very similar evolutionary stage of the selected systems. However there are some systems whose mass determination results in more massive neutron stars. Vela X-1 [172], [173] and Cygnus X-2 [174] are well known examples of neutron stars in X-ray binaries with estimated masses $1.87^{+0.23}_{-0.17}\,\mathrm{M}_\odot$ and $1.78^{+0.23}_{-0.23}\,\mathrm{M}_\odot$ respectively. The binary X-ray system Vela X-1 which includes a $\sim 20\mathrm{M}_\odot$ companion star (the mass ratio is $M_{comp}/M_{NS} = 12.3$) should be considered as a potential candidate for a double neutron star binary. In these systems the measured masses take the values $\sim 1.4\,\mathrm{M}_\odot$. Quaintrell et al. [173] made an attempt to explain this inconsistency. They indicated that the radial velocity measurements of Vela X-1 optical companion after subtraction of the orbital motion show residuals. Quaintrell suggested that these residuals can be caused by tidally induced non-radial oscillations in the companion star. These oscillations might alter the observed radial velocity variations and in the result the estimated neutron star mass in this system could be reduced to the value consistent with $1.4\,\mathrm{M}_\odot$.

Quasi-periodic oscillations (QPO) [175] also provide a method for determining masses and radii of neutron stars. The kilohertz quasi-periodic brightness oscillations have been discovered in the low mass X-ray binaries. Two quasi-periodic oscillation peaks in the range 300-1300 Hz with almost constant frequency difference appear in the power spectra of the low mass X-ray binaries containing low magnetic field neutron star. The pair can be identify with the orbital frequency ν_{orb} of accreting matter in Keplerian orbits and its beat frequency with the neutron star spin. Observations of quasi-periodic oscillations in low-mass X-ray binaries point to more massive neutron stars with masses around $2\,\mathrm{M}_\odot$.

Another constraints on neutron star parameters stem from the discovery of iron resonance scattering lines in spectra of 28 thermonuclear X-ray bursts in the low-mass X-ray binary EXO 0748-676 [176]. The detected lines have been identified as resonance scattering line of Fe

XXV Hα, Fe XXV 2-3 and O VIII $Ly\alpha$. The observed energies of all three lines give the gravitational redshift $z \sim 0.35$ [177], [178]. The analysis of the profiles of the atomic lines formed at the surface of the neutron star indicates that the line profiles are influenced by various physical effects including the spin of the star, effects of special and general relativity, rotational Doppler broadening and magnetic splitting. Özel and Psaltis [177] proposed a method which leads to the estimation of the compactness of the star. This method is based on the following formula for the surface redshift $z_{surf} \equiv E_0/E_{gm} - 1$ where E_0 denotes the rest energy of the line and $E_{gm} = \sqrt{E_1 E_2}$ is the geometric mean of the low-energy and high-energy edges of the observed lines. On obtaining the z_{surf}, the compactness of the star can be calculated with the Schwarzschild formula

$$\frac{GM}{Rc^2} = \frac{1}{2}\left(1 - \frac{1}{(1+z_{surf})^2}\right). \tag{11.2}$$

The observation of highly coherent brightness oscillations during thermonuclear X-ray bursts from low-mass X-ray binaries [165], [179], [183] has provided a new method for studying the properties of matter at supranuclear density. These brightness oscillations are thought to be produced by spin modulation of the X-ray burst flux from one or two hot spots on the stellar surface. The comparison of the observed light curve, produced by the hot spots, with the light curves calculated under various physical assumptions may put constraints on neutron star structure. The emission and propagation of photons from the surface of rapidly rotating neutron stars are influenced by relativistic effects such as general relativistic light deflection or special relativistic beaming and aberration. For example, the amplitude of pulsation is affected by gravitational light deflection which depends on the compactness of the star whereas the shape of the pulse is influenced by the rotational velocity which in turn depends on the stellar radius R and the system inclination i. The most effective analysis of the lightcurve profiles can be done if the burst oscillations has some harmonic content. Thus, of special importance is the detection of the first harmonic component in the burst oscillations in the accreting millisecond pulsar XTE J1814-338. The harmonic content of the burst oscillations denotes the ratio of power at the first harmonic to that at the fundamental one and may constrain the neutron star radius. The high surface velocity of the pulsar ($v_{surf} \approx 0.07$c) and the high harmonic content indicate that

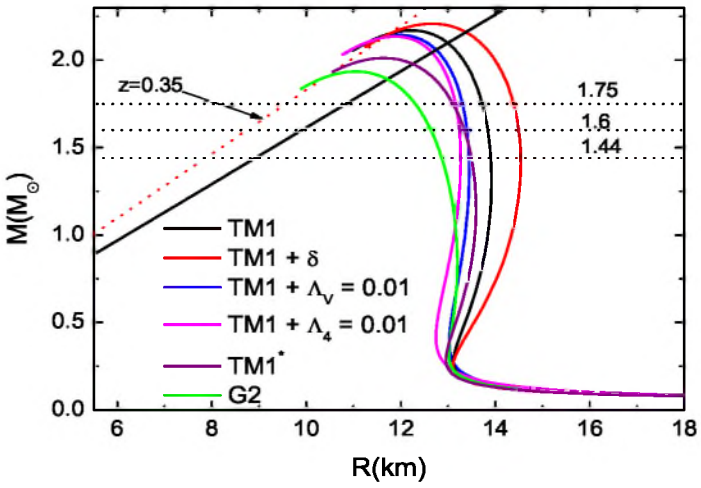

Figure 11.1: The mass-radius relations for equations of state calculated for TM1 parameter sets. The dotted, horizontal lines represent mass constraints coming from the following binary systems: 1.44 $M_\odot$-PSR 1913+16 (the most certain result), 1.6 $M_\odot$-PSR J0751+1807, 1.75 $M_\odot$-Vela X-1 (under the assumption that the measured radial velocities are purely orbital). The red dotted line indicates the constraint imposed by the surface redshift of z=0.35 measured for EXO 0748-676. The continous black line represents the constraint based on the analysis of the bolometric light curves of 22 bursts from XTE J1814-338

the radiation most likely occurs from two hot spots. The initial analysis of the burst from J1814-338 based on the calculated model of the lightcurve parameterized by the compactness, stellar spin frequency and emission parameters, results in the neutron star's compactness GM/Rc^2 at the value of 0.238 at the 90% confidence level.

In the case of white dwarf-neutron star binaries the extensive mass accretion during the low-mass X-ray binary phases occur, so there is the possibility for the existence of relatively massive pulsars in these systems. Recent observations of four millisecond pulsars in pulsar-white dwarf binaries made with the Arecibo telescope have proved the correctness of this idea [180], [181], [182].

The presented astrophysical limitations on neutron star parameters attempt to put constraints on the high density behavior of neutron star matter equation of state. The mass constraints connected with the

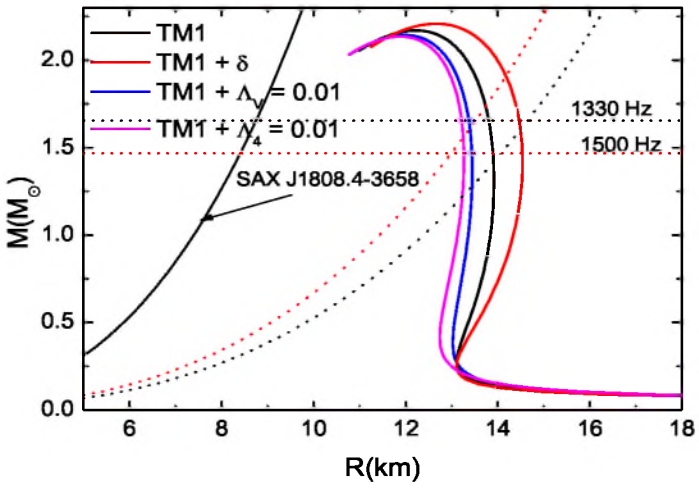

Figure 11.2: The mass-radius relations for equations of state calculated for TM1 parameter sets. This figure includes constraints from orbital frequencies. Dotted lines represent mass-radius limits for the two frequencies: the frequency measured for 4U 0614+091 (1330 Hz) and for the hypothetical 1500 Hz. Arrow indicate the results obtained for the millisecond pulsar SAX J1808.4-3658

reported masses of: PSR 1913+16-1.44 $M_\odot$ [180], PSR J0751+1807-1.6 $M_\odot$ [182] and Vela X1-1.75 $M_\odot$ [172], [173] indicate a rather stiff equation of state. Considering the presented models only the equation of state for the G2 parameter set supplemented with the strong hyperon-hyperon interaction does not satisfy this limit.

The measurements of the gravitational redshift of spectral lines produced in the neutron star photosphere made possible to determine the mass to radius ratio of a neutron star providing the constrain on the mass radius diagram. The analysis of the spectra of 28 bursts of the low-mass X-ray binary EXO 0748-676 leads to identification of the iron resonance scattering lines with a redshift of z=0.35 [176]. The comparison of this result with the theoretical mass-radius relations obtained for the considered parameter sets is presented in Fig. 11.1 and Fig. 11.3. This test only marginally indicates the pure nucleonic neutron star models and excludes the models with nonzero strangeness. The analysis of the light curves of 22 bursts from the accreting millisecond pulsar XTE J1814-338 [178] provides information on the compactness

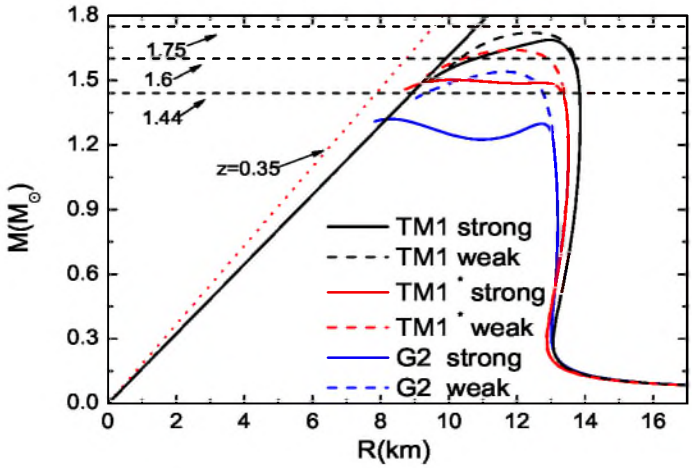

Figure 11.3: The mass-radius relations obtained for the strangeness rich matter. The results for TM1, TM1* and G2 parameter sets with strong $Y-Y$ coupling are presented and compared with that for the weak $Y-Y$ coupling. The lines which represent individual constraints, are the same as in Fig. 11.1

of this star $Rc^2/GM > 4.2$, estimating its value at the 90% confidence level. This constraint is marked on the theoretical mass-radius diagram with a black, solid, straight line in Fig. 11.1 and Fig. 11.3. Observations of the twin kilohertz quasi-periodic oscillations which result from the orbital motion in the inner accretion flow indicate the existence of the neutron star mass constraint. In Fig. 11.2 and Fig. 11.4 the results are presented for the highest detected frequency $\nu_{QPO} = 1330$ Hz [184] for 4U 0614+091 (black dotted lines), and for the hypothetical frequency $\nu_{QPO} = 1500$ Hz (red dotted lines). The discovery of the accreting millisecond X-ray pulsar SAX J1808.4-3658 offers another possibility to estimate the compactness of the pulsar. Observations of SAX J1808-3658 show pulsations at 401 Hz. Li et al. in their paper [185] proposed a method which allows to determine neutron star parameters. Assuming that the accretion of matter in this binary system is from the Keplerian accretion disc detection of X-ray pulsations leads to the following relation $R < R_0 < R_c$, where R_0 is the inner radius of the accretion flow, R is the stellar radius and R_c denotes the corotation radius defined as $R_c = (GM/(4\pi^2)P^2)^{1/3}$, M is the mass of the star

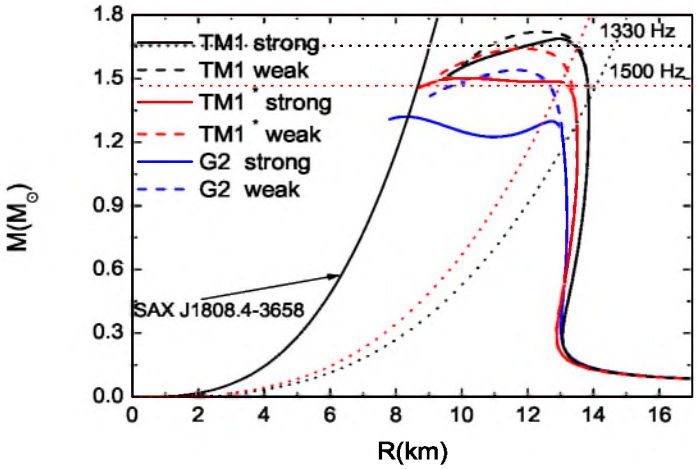

Figure 11.4: The mass-radius relations obtained for the strangeness rich matter. The results for TM1, TM1* and G2 parameter sets with strong $Y-Y$ interactions are presented and compared with that for the weak $Y-Y$ interactions. The lines, which represent individual constraints, are the same as in Fig. 11.2

and P is the pulse period. The inner disc radius R_0 is given in terms of the Alfven radius R_A which denotes the radius at which the material and magnetic stresses balance $R_0 = \zeta R_A = \zeta(B^2R^6/\dot{M}(2GM)^{1/2})^{2/7}$, where B is the surface magnetic field and $\dot{M}$ is the mass accretion rate of the pulsar. Further assuming that the accretion rate $\dot{M}$ is proportional to the flux F and the magnetic field is primarily dipolar then $R_0 \propto F^{-2/7}$ and the radius of the pulsar can be estimated from the following condition [185]

$$R < 27.6 \left(\frac{F_{max}}{F_{min}}\right)^{-2/7} \left(\frac{P}{2.49ms}\right)^{2/3} \left(\frac{M}{M_\odot}\right)^{1/3} km, \qquad (11.3)$$

where F_{max} and F_{min} denote the X-ray fluxes measured during X-ray high and low-state, respectively. In the paper [185] the value of $\frac{F_{max}}{F_{min}} \simeq 100$ has been adopted. The analysis based on data collected from observations of the pulsar SAX J1808.4-3658 lead to the following result $R < 7.5$ km. This result imposes very strong limitation on the available nuclear matter equations of state. The constraint proposed by Li et al. [185] which leads to very compact neutron stars

strongly indicates soft equations of state. In general a soft equation of state can be obtained for strange neutron star matter. The theoretical mass-radius relations calculated within the chosen models presented in Fig. 11.4 show that the neutron star model constructed for the G2 parameterization with the strong hyperon-hyperon coupling is able to sustain marginally the presented constraint. However, the idea proposed by Li et al. [185] is very model-dependent. Enforcing this model is making rigorous demands on the accretion flow controlled by the magnetic field.

Chapter 12

Proto-neutron star model

Assuming the evolutionary scenarios presented by Suzuki [62] and Prakash et al.[151] the following stages in the life of a proto-neutron star have been selected:

- Stage 1: the post bounce phase – the bounced inner core settles into a hydrostatic configuration. Under the assumption of the very low kinetic energy of the matter behind the shock, the structure of the outer envelope can also be approximated by hydrostatic equilibrium. Thus a proto-neutron star model immediately after the collapse can be constructed basing on the following physical conditions: the low entropy core $s = 1$ (s denotes the entropy per baryon in k_B units) with trapped neutrinos $Y_L = 0.4$ is surrounded by a high entropy $s = 2 - 5$ outer layer also with trapped neutrinos. The energy is carried out from a proto-neutron star by neutrinos and antineutrinos of all flavors, whereas the lepton number is lost by the emission of electron neutrinos which are produced in the β process $e^- + p \rightarrow \nu_e + n$. Deleptonization in the outer envelope proceeds faster than that in the inner core.

- Stage 2: deleptonization of the outer layer is completed. The physical conditions that characterized the whole system are as follows: the core with the entropy $s = 2$ and $Y_L = 0.4$ and the deleptonized outer envelop with $s = 2$ and $Y_\nu = 0$.

- Stage 3: during this stage the deleptonization of the core takes place, after which the core has neutrino-free, high entropy $s = 2$ matter. Thermally produced neutrino pairs of all flavors are

abundant, and they are emitted with very similar luminosities from the thermal bath of the core.

- Stage 4: cold, catalyzed object.

12.1 Neutrino opacities

Neutrinos, due to their frequent interactions with the surrounding matter at sufficiently high density are trapped in the proto-neutron star matter [9], [186], [187]. The total neutrino opacity includes contributions from both scattering and absorption processes [9]. In a proto-neutron star environment μ and τ neutrinos are thermally produced so their energies are of the order k_BT and the inequality $k_BT \leq m_\mu c^2, m_\tau c^2$ is satisfied. This means that the charged current reactions for ν_μ and ν_τ neutrinos are kinematically suppressed. Thus only electron neutrinos and antineutrinos undergo charge current reactions, whereas neutral current reactions involve all flavors of neutrinos. Neutrino coupling to leptons in the same family is modified since the scattering may proceed due to both W and Z exchange.

Having obtained the proto-neutron star model, one can calculate the radial profile of the pressure, energy density, temperature, nucleon and lepton number densities for the given proto-neutron star model. This is essential in determining the neutrino interaction rate with the surrounding medium as it depends on density and temperature. Due to the physical conditions in proto-neutron star interiors and different neutrino processes which undergo in proto-neutron star matter, several regions in the proto-neutron star can be selected. Deep inside the core of a proto-neutron star the pair creation processes occur [187], [188]:

- neutrino-pair annihilation $\nu_e\bar{\nu}_e \leftrightarrow \nu_\mu\bar{\nu}_\mu$
- electron-positron annihilation $e^+e^- \leftrightarrow \nu_\mu\bar{\nu}_\mu$
- nucleon-nucleon bremsstrahlung $NN \leftrightarrow NN\nu_\mu\bar{\nu}_\mu$.

This allows for the energy exchange and for the creation and annihilation of neutrino pairs and the concept of the so-called numbersphere has been introduced [189]. The numbersphere located at the radius R_{NS} denotes the region of the star in which neutrinos of all flavors are kept in local thermal equilibrium. Thus the position of a numbersphere determines the neutrino flux. Exterior to this region there is

no neutrino pairs creation or annihilation. Neutrinos are no longer in thermal equilibrium. However, there are still effective processes which allow for the energy exchange. They are the scattering reactions:

$$e^{\pm} + \nu_{\mu} \rightarrow e^{\pm} + \nu_{\mu}, \tag{12.1}$$

$$N + \nu_{\mu} \rightarrow N + \nu_{\mu}. \tag{12.2}$$

The rate of these reactions depends on electron and nucleon concentrations in the considered proto-neutron star model. As the nucleon concentrations exceed that of electrons, scattering on nucleons is more frequent then scattering on electrons. However, in the latter case there is a large energy transfer. The reaction (12.1) becomes ineffective in the energysphere [189] characterized by the radius R_{ES}. Outside the energysphere the process (12.2) is still effective. The energy exchange in this reaction is very small. The ineffectiveness of the reaction (12.2) determines the radius of the transportsphere R_{TS}. The surface of the transportsphere is at the same time the surface of the last scattering for neutrinos. All these processes also occur for the electron neutrinos and antineutrinos, however, the dominant source of their opacities is the charged current absorption processes

$$\nu_e + n \leftrightarrow e^{-} + p \tag{12.3}$$

$$\bar{\nu}_e + p \leftrightarrow e^{+} + n. \tag{12.4}$$

Due to the decreasing density there is a region in the star, indicated as neutrinosphere, outside which these processes are no longer efficient [190], [191]. The radius of the neutrinosphere R_{ν} defines the effective surface from which electron neutrinos and antineutrinos are emitted. Exterior to this radius, neutrinos stream off freely and their spectrum is characterized by a temperature which is the medium temperature at the neutrinosphere. The concept of a neutrinosphere does not allow for its unique localization. The cross sections of the β processes depend on neutrino energy and thus different energy neutrinos decouple energetically from the stellar background at different radii. The precise determination of a neutrinosphere position is not possible. It is energy dependent.

Different types of neutrino interactions with the surrounding matter result in different types of neutrino behavior within the star. Neutrino

transport throughout a proto-neutron star can be presented schematically using the concept of the optical depth. The optical depth can be defined as [190]

$$\tau_{\nu_i} = \int_r^{\infty} \lambda_{\nu_i}^{-1} dr' \tag{12.5}$$

where $\lambda_{\nu_i}^{-1} = \sigma_{\nu_i}(\epsilon) n_i$ is the inverse mean free path for a given interaction channel and σ_{ν_i} is the cross section for this particular process. Taking advantage of the concept of the optical depth one can determine the location of the point inside a star from which neutrinos can escape freely from their point of emission without undergoing any absorption and scattering reactions. This is equivalent to the condition $\tau < 1$. The depth at which $\tau = 2/3$ is known as the thermalization depth and marks the point above which the assumption of local thermal equilibrium is no longer valid.

Considering the scattering reactions two different mean free paths have to be defined: one for isoenergetic scattering on nucleons – the transport mean free path λ_T and the other one which is related to the scattering with large energy transfer-the mean free path λ_E for inelastic scattering off electrons. The average distance between successive energy exchange scattering events requires the definition of the effective mean free path

$$\tau_{eff}(r, \epsilon) = \int_r^{\infty} dr' \sqrt{\frac{1}{\lambda_E(r', \epsilon)} \left[\frac{1}{\lambda_T(r', \epsilon)} + \frac{1}{\lambda_E(r', \epsilon)} \right]}. \tag{12.6}$$

Assuming that neutrinos are in thermodynamical equilibrium with the proto-neutron star matter until they decouple energetically at their corresponding energyspheres, neutrino spectra can be described by Fermi-Dirac distributions with temperatures being equal to the local temperature of the stellar matter $T_{\nu_i} = T(R_{\nu_i})$ [190].

12.2 The influence of neutrino trapping on proto-neutron star properties and evolution

As the core collapse continues neutrinos are generated by thermal emission and electron capture processes. Thermal emission processes are:

pair annihilation ($e^+ + e^- \rightarrow \nu + \bar{\nu}$), photoannihilation ($e^- + \gamma \rightarrow e^- = \nu + \bar{\nu}$), bremsstrahlung ($e^- + (Z, A) \rightarrow (Z, A) + e^- + \nu + \bar{\nu}$) and plasmon decay ((plasma excitation)$\rightarrow \nu + \bar{\nu}$) [9]. These reactions proceed by charge and neutral currents. This is also the case for the electron-positron annihilation when electron neutrino pairs are produced [192]. Muon and tau neutrino pairs ($\nu_\mu, \bar{\nu_\mu}$, $\nu_\tau, \bar{\nu_\tau}$) are only produced by the exchange of the Z vector meson. During the core collapse the charged current reactions of electron capture by nuclei

$$e^- + (Z, A) \rightarrow \nu_e + (Z - 1, A) \tag{12.7}$$

and electron capture by free protons

$$e^- + p \rightarrow \nu_e + n \tag{12.8}$$

are the dominant sources of electron neutrinos. In the case of high electron degeneracy the reaction of pair production which leads to the production of neutrinos via

$$\gamma + \gamma \rightleftharpoons e^- + e^+ \rightarrow \nu_i + \bar{\nu}_i \tag{12.9}$$

can be suppressed. Pair production is favored by high temperature and low density [9]. In the very early stage of the collapse only electron neutrinos are produced by electron capture on nuclei and on free protons. The main opacity source for electron neutrinos is coherent scattering off nuclei. At the beginning of the collapse electron neutrinos can escape freely from the core. When the density of the matter ρ exceeds the value $3 \times 10^{10}\mathrm{gcm}^{-3}$ and the neutrino mean free path giving by the relation

$$\lambda_\nu \sim 10^7 cm \left(\frac{\rho}{3} 10^{10} \frac{g}{cm^3}\right)^{-5/3} \left(\frac{A}{65}\right)^{-1} \left(\frac{26 Y_e}{56}\right)^{-2/3} \tag{12.10}$$

is shorter than the core radius, the core becomes opaque for neutrinos. The presented model of a nascent neutron star is constructed under the assumption that the star can be divided into two main parts: the dense core and the outer layer. As was stated above, at the very beginning of proto-neutron star evolution neutrinos are trapped on the dynamical time scale within the matter both in the core and in the outer layer. The estimated electron lepton fraction ($Y_L = Y_e + Y_{\nu_e}$) at trapping, with the value of ≈ 0.4 and the assumption of constant entropy, allows one

to specify the star characteristics at the conditions prevailing in the star interior. The outer region of a proto-neutron star is characterized by the following conditions: it is less dense and less massive than the core, the assumptions of nearly complete disintegration of nuclei into free nucleons and β-equilibrium have been made. The chemical potentials of the constituents of the matter are evaluated by the requirement of charge neutrality and β-equilibrium. The equation of state appropriate for the description of the matter in the outermost layer of a nascent neutron star includes contributions coming from nucleons, electrons, photons and neutrinos

$$P = P_N + P_e + P_{rad}. \tag{12.11}$$

At sufficiently low density, in the absence of interactions which alter the nucleon mass, nucleons are considered as non-relativistic and they form non-degenerate, non-relativistic gas which can be described by the equation

$$P_n = k_B T n_b \tag{12.12}$$

where n_b is the baryon number density.

The theoretical model of the dense inner core can be constructed under the following assumptions: the matter includes the full octet of baryons interacting through the exchange of meson fields, the composition is determined by the requirements of charge neutrality and generalized β-equilibrium.

The loss of lepton number from the collapsed star proceeds in separate stages. First, the deleptonization of the surface layer takes place in a very short time in comparison with the Kelvin-Helmholtz neutrino cooling time. After that the deleptonization of the core proceeds by the emission of electron neutrinos which are produced efficiently via the β-processes. The events between the two distinguished moments depend on the details of the considered models, especially on the equation of state. The initial moment $t = 0$ characterizes the stage with neutrinos trapped ($Y_L = 0.4$) both in the core and in the outer envelope. Introducing a parameter α, which determines the degree of deleptonization of the proto-neutron star matter, the moment $t = 0$ can be identified with $\alpha = 1$ whereas the final completely deleptonized stage ($Y_\nu = 0$) is described by $\alpha = 0$. The density at the core-outer layer interface is time dependent. This dependence can be presented by comparing the inner core equation of state and the equations of state of the outer

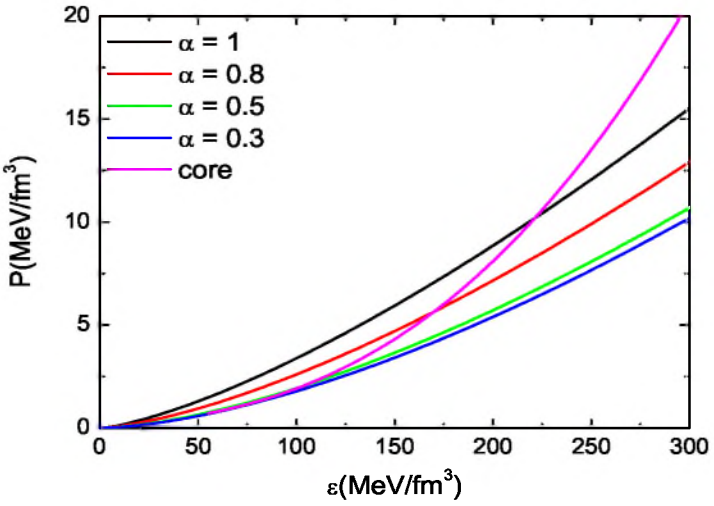

Figure 12.1: The density dependence of the interface between the inner core equation of state and the equations of state which have been obtained for different values of the parameter α in the outer layer of a proto-neutron star for the the strong hyperon-hyperon interaction for the G2 parameter set

layer which have been obtained for different values of the parameter α. Results obtained for the G2 parameter set are shown in Fig. 12.1 and Fig. 12.2. These figures have been constructed for weak and strong hyperon-hyperon interactions. The core-outer layer interface proceeds at higher densities for the weak model. The deleptonization leads to a substantial reduction in the extension of the proto-neutron star envelope.

The analysis of proto-neutron star models with conserved electron lepton number has been done on the basis of the G2 model. The obtained forms of the equations of state for of the proto-neutron star matter for the strong and weak $Y - Y$ interactions are plotted in Fig. 12.3 and 12.4.

Both models have yielded identical results up to a certain value of density: the hot, neutrino-trapped matter is described by the stiffest equation of state whereas the hot, deleptonized and cold ($T = 0$) proto-neutron star models result in softer equations of state. There are two kinks on the equation of state of cold, deleptonized neutron star matter. The presence of these kinks has profound consequences for the existence

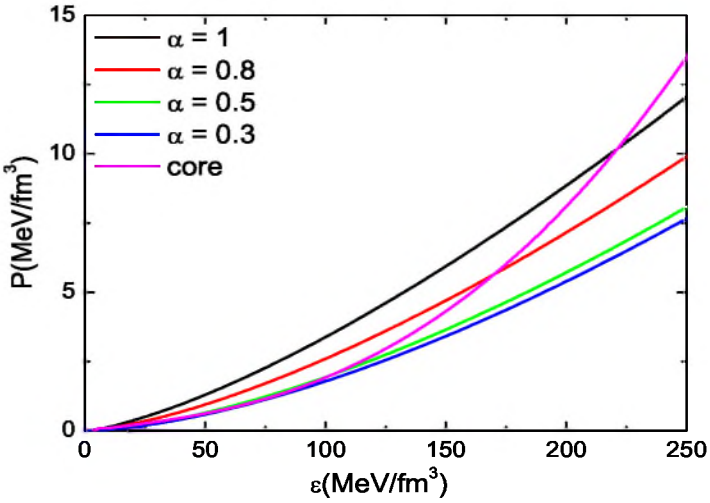

Figure 12.2: The density dependence of the interface between the inner core equation of state and the equations of state which have been obtained for different values of the parameter α in the outer layer of a proto-neutron star for the weak $Y-Y$ interaction for the G2 parameter set

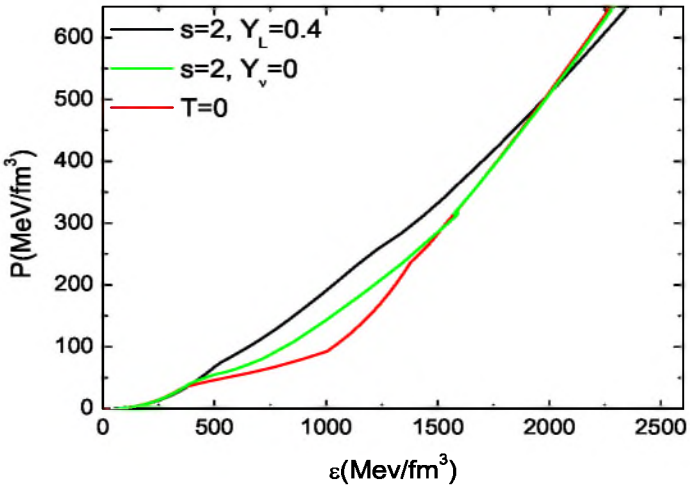

Figure 12.3: The equation of state of the proto-neutron star matter for the G2 parameter set for the strong $Y-Y$ interaction

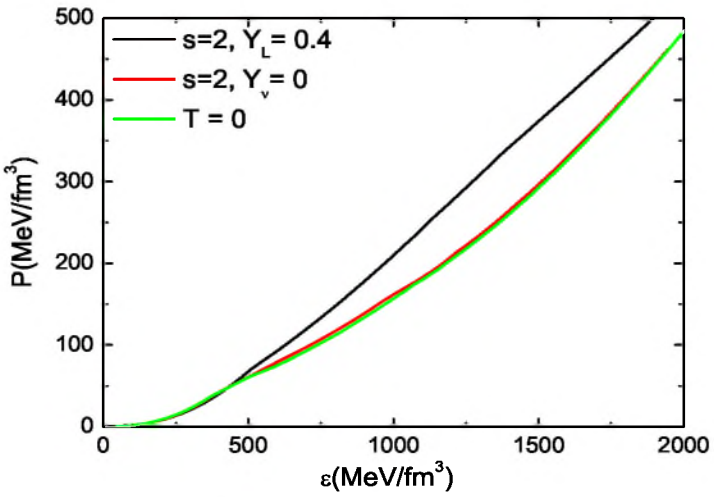

Figure 12.4: The equation of state of the proto-neutron star matter for the G2 parameter set for the weak $Y - Y$ interaction

of stable solutions on the mass-radius diagram. In general these two kinks mark the limits for which there is a noticeable softening of the equation of state and are connected with the appearance of hyperons. The composition of hyperon star matter as well as the the threshold density for hyperons are altered when the strength of the hyperon-nucleon and hyperon-hyperon interactions are changed. Fig. 12.5 and Fig. 12.6 present fractions of particular strange baryon species Y_B as a function of baryon number density n_b for the weak and strong $Y - Y$ interaction model of the G2 parameterization for the three selected evolutionary phases. All calculations have been done on the assumption that the repulsive Σ interaction shifts the onset points of Σ hyperons to very high densities and they do not appear in the considered proto-neutron and neutron star models.

The onset of Ξ^0 hyperons takes place at very high densities and they are not presented in Fig. 12.5 and Fig. 12.6. In the case of strong and weak Y – Y interactions the onset of Λ hyperons is followed by the onset of Ξ^- hyperons. In general, when Λ hyperons appear they replace protons and, in consequence, lower the energy of the system. This fact, through the requirement of charge neutrality of neutron star matter, results in diminished electron chemical potential. The populations

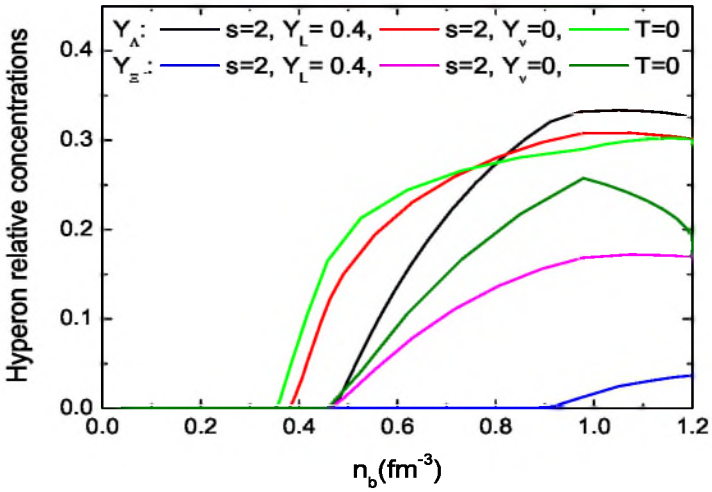

Figure 12.5: Relative concentrations of Λ and Ξ hyperons in hyperon star matter for the G2 parameter set in the case of the strong hyperon-hyperon interaction

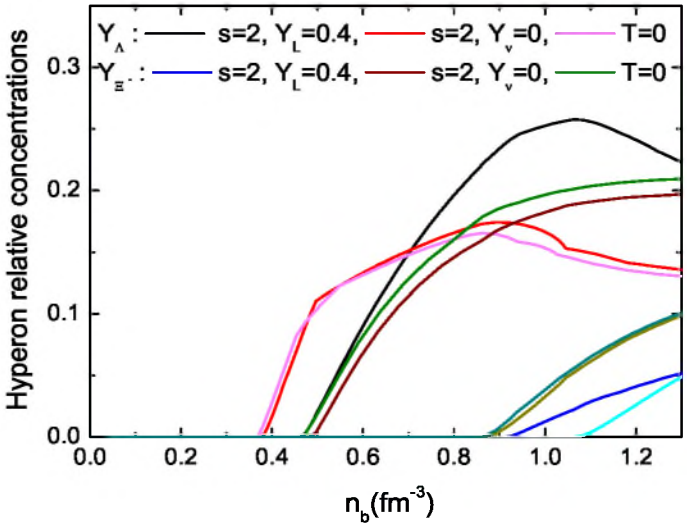

Figure 12.6: Relative concentrations of Λ and Ξ hyperons in hyperon star matter for the G2 parameter set for the weak hyperon-hyperon interaction

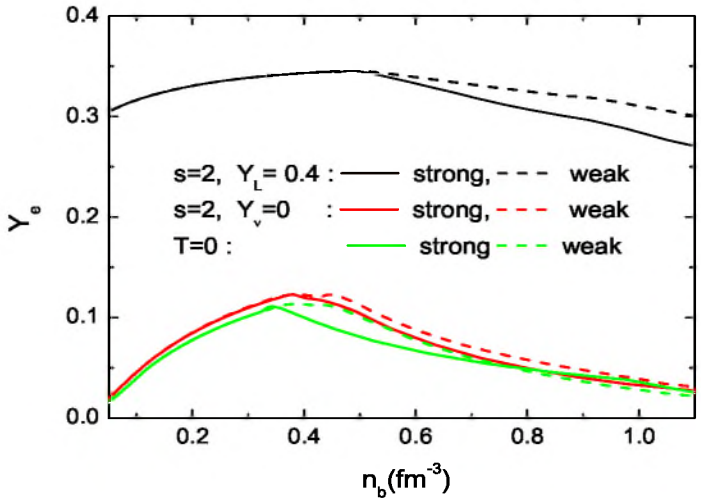

Figure 12.7: Relative concentrations of electrons in hyperon star matter for the G2 parameter set

of Λ hyperons obtained in the weak Y – Y coupling models in the considered evolutionary stages are reduced in comparison with those calculated for the strong Y – Y interaction models. The weak model with the reduced Λ hyperon population leads to the increased value of electron and proton concentrations. Results are presented in Fig. 12.7 and Fig. 12.8 where relative concentrations of electrons and protons are depicted.

One can also compare the concentrations of neutrinos in the hot, neutrino trapped matter. In Fig. 12.9 neutrino concentrations as a function of baryon number density n_b for the two different models are shown.

The weak model leads to lower concentration of neutrinos. For comparison, results for non-strange proto-neutron star matter are included. Once the equations of state have been calculated for each evolutionary phases, for the strong and weak models the corresponding hydrostatic models of proto-neutron stars have been obtained. Solutions of the Oppenheimer–Tolman–Volkoff equation for the considered parameter sets are presented in Fig. 12.10 and Fig. 12.11. In agreement with the introduced evolutionary stages of a proto-neutron star the obtained mass-radius relations include a sequence of models constructed for the

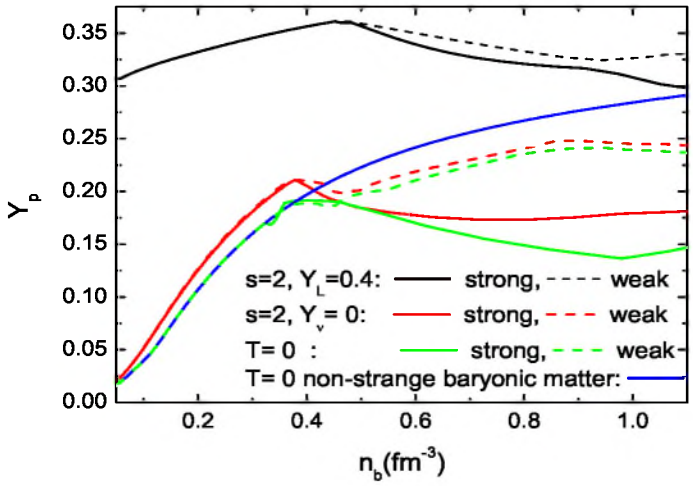

Figure 12.8: Relative concentrations of protons in hyperon star matter for the G2 parameter set

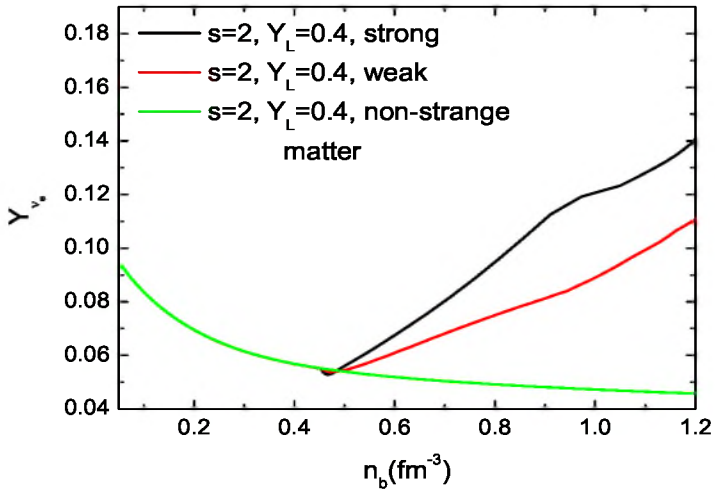

Figure 12.9: Density dependence of neutrino concentrations for the G2 parameter set

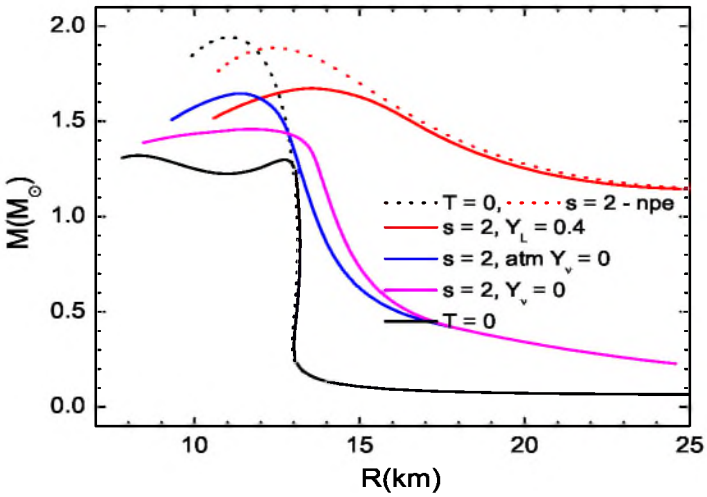

Figure 12.10: The mass-radius relations for subsequent stages of the proto-neutron star evolution for G2 parameterization with the strong $Y - Y$ coupling. Dotted lines represent solutions obtained for non-strange baryonic matter

given equation of state calculated for a specific phase of a proto-neutron star evolution. In Fig. 12.10 the results for six equations of state have been plotted. The four mass-radius relations are constructed for the strangeness-rich baryonic matter and they represent the evolution of a proto-neutron star starting from the moment when the proto-neutron star can be modelled as a low entropy core surrounded by a high entropy outer layer. Neutrinos are trapped both in the core and in the outer layer. This very initial phase of a proto-neutron star is followed by two subsequent stages connected with the process of deleptonization of a proto-neutron star. The first, is when the deleptonization of the outer layer takes place, whereas in the core neutrinos are still trapped and the second one represents a hot deleptonized object with thermally produced neutrino pairs of all flavor abundant in the core and in the outer layer. The final case is exemplified by a solution obtained for cold strangeness-rich neutron star matter. For comparison the mass-radius relations for for the nonstrange baryonic matter have been presented. A similar sequence of the mass-radius relations have been constructed for the G2 parameterization supplemented by the weak Y – Y parameter set for the strange sector. The G2-strong parameterization leads to proto-neutron neutron stars with the reduced

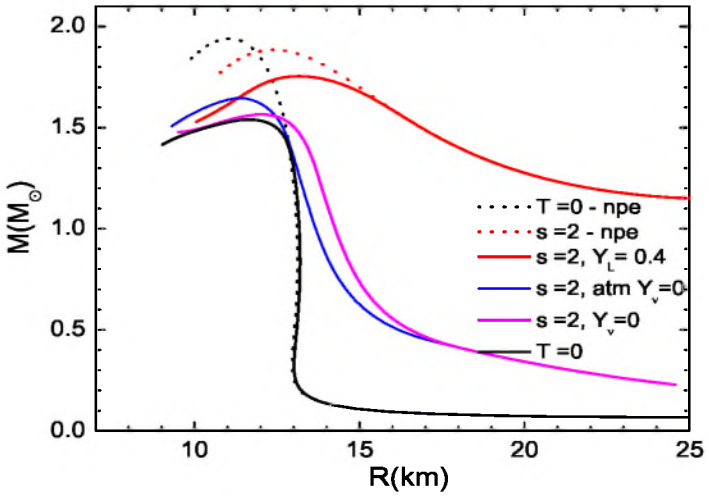

Figure 12.11: The same as in Fig. 12.10 for weak $Y-Y$ model

Table 12.1: Proto-neutron and neutron star parameters obtained for the maximum mass configurations for the G2 parameterization with the strong $Y-Y$ interactions

		ρ/ρ_0	R (km)	M $(M_\odot)$	M_B $(M_\odot)$
T=0	A	5.00	12.73	1.298	1.407
	B	21.76	8.22	1.320	1.634
s=2		8.76	13.528	1.673	1.855

Table 12.2: Proto-neutron and neutron star parameters obtained for the maximum mass configurations for the G2 parameterization with the weak $Y-Y$ interactions

	ρ/ρ_0	R (km)	M ($M_\odot$)	M_B ($M_\odot$)
T=0	8.00	11.63	1.540	2.102
s=2	9.12	13.14	1.754	1.915

values of the maximum masses. For the strong hyperon-hyperon interaction in the case of the cold neutron star model, apart from the ordinary neutron star branch, there exists an additional stable branch of solutions [198, 199, 201]. They distinguish themselves by the values of masses similar to those of ordinary neutron stars yet with radii that are significantly reduced. For the purpose of this analysis A denotes the maximum mass configuration of the ordinary neutron star branch and B the mass of the additional maximum. The additional stable solutions may be interpreted in terms of the third family of stable compact stars. Proto-neutron and neutron star parameters are summarized in Tables 12.1 and 12.2 [145]. The presented results have been obtained for maximum mass configurations. Neutron stars are purely gravitationally bound objects. The total baryon number of the star defined as

$$N_b = 4\pi \int_0^R dr r^2 \left(1 - \frac{2Gm(r)}{c^2 r}\right)^{-\frac{1}{2}} n_b(r) \tag{12.13}$$

allows one to calculate the baryon mass of the star $M_B = N_b m_B$. After obtaining the baryon mass the gravitational binding energy of a relativistic star can be calculated

$$E_{b,g} = (M_B - M_G)c^2, \tag{12.14}$$

where M_G is the gravitational mass.

A numerical solution of the above equation has been found for the selected equations of state for the strong and weak Y – Y interactions. The results are shown in Fig. 12.12 and Fig. 12.13 where the gravitational mass a function of baryon mass is presented.

In both figures for comparison the solutions for non-strange proto-neutron and neutron star models have been included.

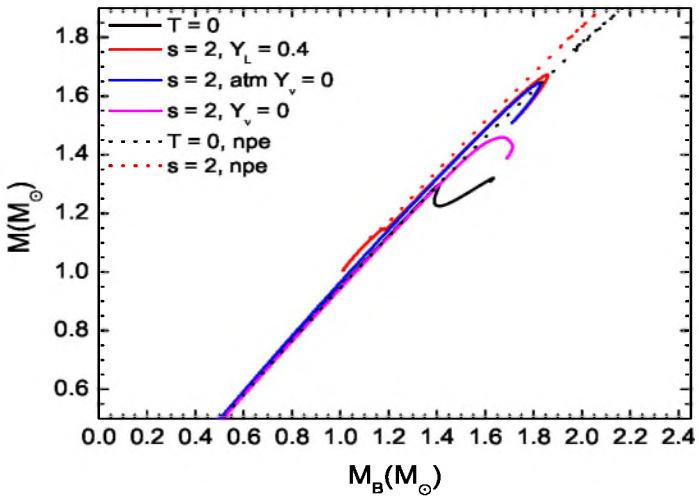

Figure 12.12: The gravitational mass versus baryon mass for the G2 parameter set for the strong $Y - Y$ interaction

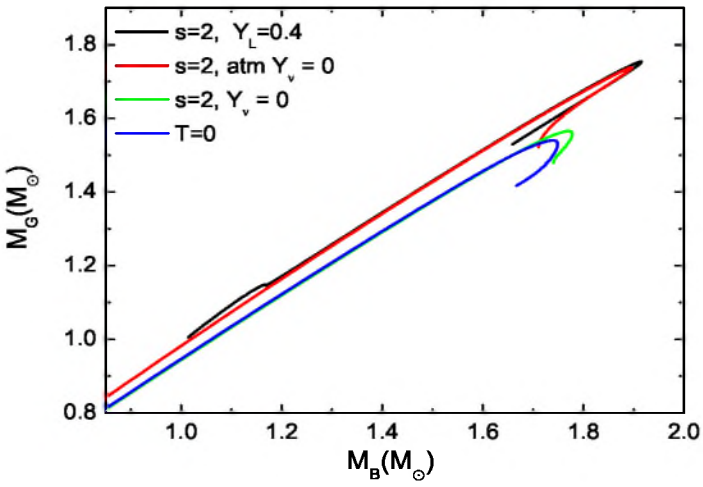

Figure 12.13: The gravitational mass versus baryon mass for the G2 parameter set for the weak $Y - Y$ interaction

Fig. 12.14 presents the possibility of the existence of the neutron star twins [193, 194, 195, 196, 199]. This is connected with the existence of stars with comparable masses but with different radii. The twin star collapse corresponds to the transition from the configuration of higher gravitational mass to that of the lower mass. This phenomenon is not possible in the case of the TM1* solution. The influence of the the potential depth $U_\Lambda^{(N)}$ in nuclear matter on neutron star parameters is presented in Fig. 10.30. This figure displays the neutron star mass as a function of the central density. The results have been obtained for different values of $U_\Lambda^{(N)}$ potential: $U_\Lambda^{(N)} = -27, -28$ and -30 MeV. The heights of the two subsequent maxima on the mass-central density relation depend on the potential $U_\Lambda^{(N)}$. The maximum mass of the ordinary neutron star sequence (A) is greater then the maximum mass of the compact star B for the minimal value of the potential $U_\Lambda^{(N)} = -27$ MeV. For $U_\Lambda^{(N)} = -28$ or -30 MeV the maximum mass configuration B exceeds the mass of the star A. The obtained mass-radius relations for the non-strange baryonic matter confirm the well-known fact that in this case the maximum mass of a proto-neutron star with trapped neutrinos is lower than that of cold deleptonized matter. This has a consequence for the possibility of a black hole formation during the relatively long lasting phase of deleptonization [151]. In the case of non-strange matter a proto-neutron star is not able to achieve the unstable configuration due to deleptonization. In general, neutrino trapping increases the value of the maximum mass for the strangeness rich baryonic matter. In all evolutionary stages there are configurations which after deleptonization go to the unstable branch of proto-neutron and neutron stars. The obtained solutions of the structure equations allow one to carry out the analysis of the onset points, abundance and distributions of the individual baryon and of lepton species but now as functions of the star radius R. The analysis includes results obtained for two extreme evolutionary phases: the very beginning hot, neutrino-trapped matter stage and for the cold, deleptonized one. Two characteristic configurations have been considered for the $T = 0$ solution. Namely, the one connected with the maximum mass configurations marked as A and the other for the B maximum mass configuration of the G2 strong parameterization. The compact hyperon core which emerges in the interior of the maximum mass configuration consists of Λ, Ξ^- and Ξ^0 hyperons. The hyperon population is reduced to Λ and Ξ^- in the case of hot neutrino trapped matter for the weak model. The

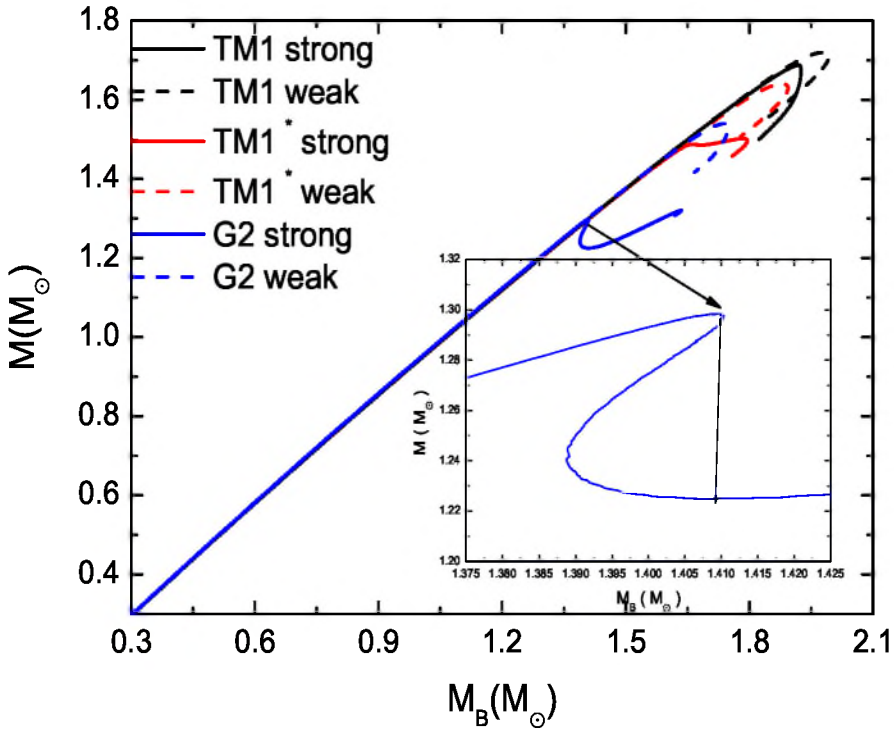

Figure 12.14: The gravitational mass versus baryon mass for the G2 parameter set for the strong $Y-Y$ interaction. The inner panel depicts the possibility of the transition from the ordinary neutron star configuration to the maximum mass configuration on the second stable sequence

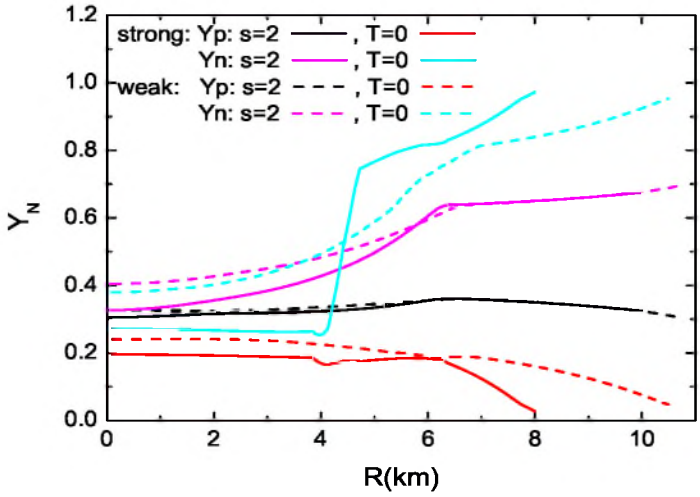

Figure 12.15: Relative concentrations nucleons in hyperon star matter as a function of stellar radius for the G2 parameter set for the strong and weak $Y-Y$ interactions. The results are presented for the maximum mass configuration

process of deleptonization and cooling diminishes the concentration of Λ hyperons and increases concentrations of Ξ^- and Ξ^0 hyperons. The reduction of Λ hyperon population in the weak model is larger then that obtained for the strong Y – Y interaction model. The relative fractions of hyperons in the core of the maximum mass configurations are presented in Fig. 12.16 and Fig. 12.17. Horizontal lines in the left panels of Fig. 12.16 and Fig. 12.17 correspond to the threshold density of individual hyperons in the considered model. The configuration marked as A does not contain hyperons. The appearance of Ξ^- hyperons through the condition of charge neutrality affects the lepton fraction and causes a drop in their contents. Charge neutrality tends to be guaranteed with the reduced lepton contribution. Results are shown in Fig.12.15 and Fig.12.18. Stars of the first stable sequence are mainly composed of nucleons with a small admixture of Λ hyperons. Whereas stars of the second stable branch have developed very compact hyperon core with approximately equal numbers of Λ, Ξ^- and Ξ^0 hyperons and nucleons. The presence of the hyperon core can be interpreted in terms of the appearance of a new phase of matter, the hyperon matter which is characterized as being composed of nearly equal concentrations of hyperons and nucleons.

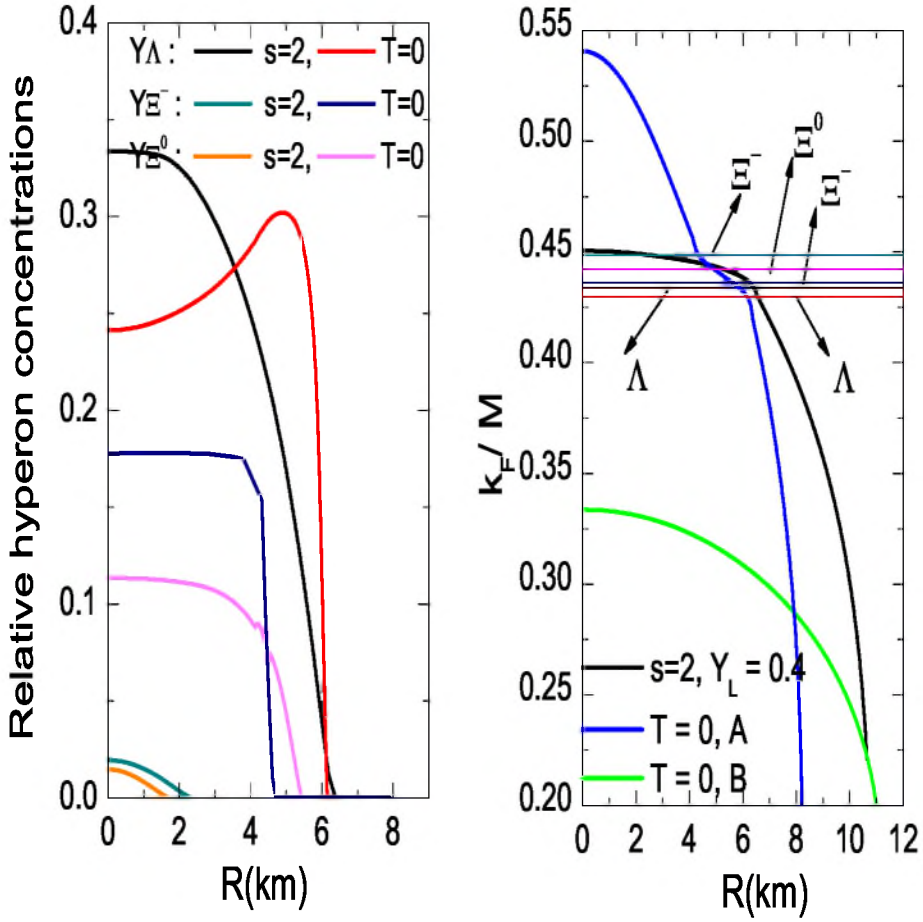

Figure 12.16: The fraction of species i, Y_i in the maximum mass configuration as a function of star radius for the G2 strong parameter set (k_F means the effective Fermi momentum which specifies the value of ν_b in equation (8.3)

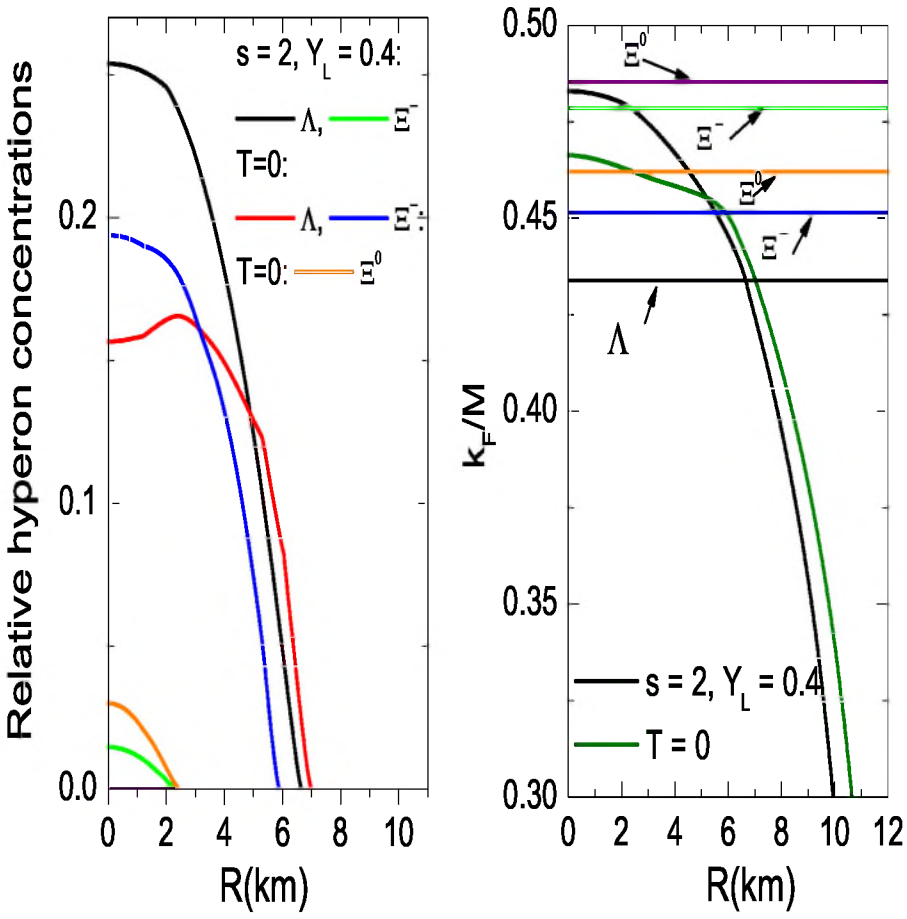

Figure 12.17: The fraction of species i, Y_i in the maximum mass configuration as a function of star radius for the G2 weak parameter set

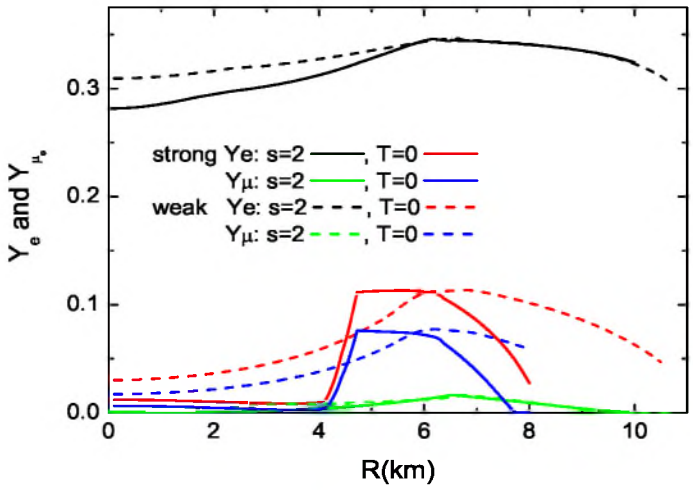

Figure 12.18: Relative concentrations of electron and muons in hyperon star matter for the G2 parameter set for the strong and weak $Y-Y$ interactions

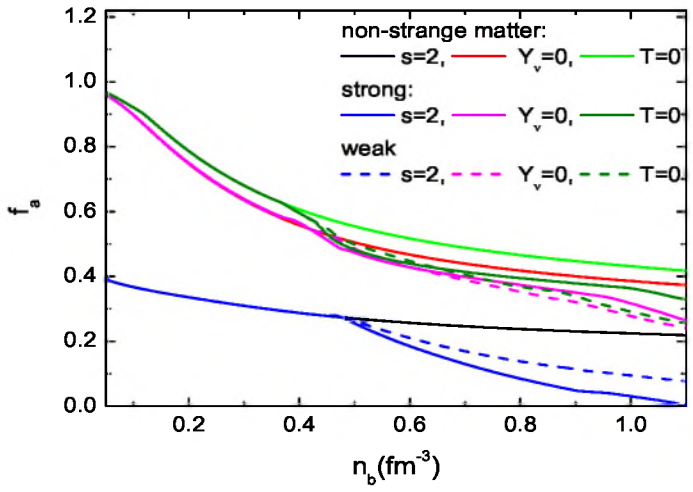

Figure 12.19: The parameter f_a as a function of baryon number density n_b for the strange and non-strange baryonic matter calculated for each specified evolutionary phases. The hot models with trapped neutrinos are marked as $s=2$, whereas hot, deleptonized models as $Y_\nu = 0$

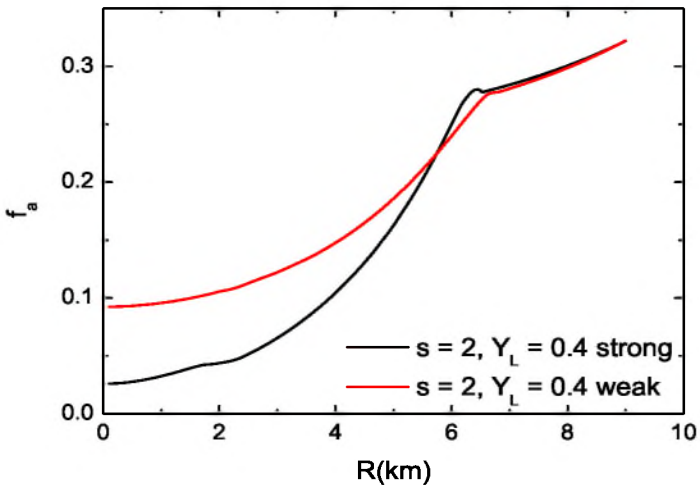

Figure 12.20: The parameter f_a as a function of the stellar radius for the weak and strong models are presented

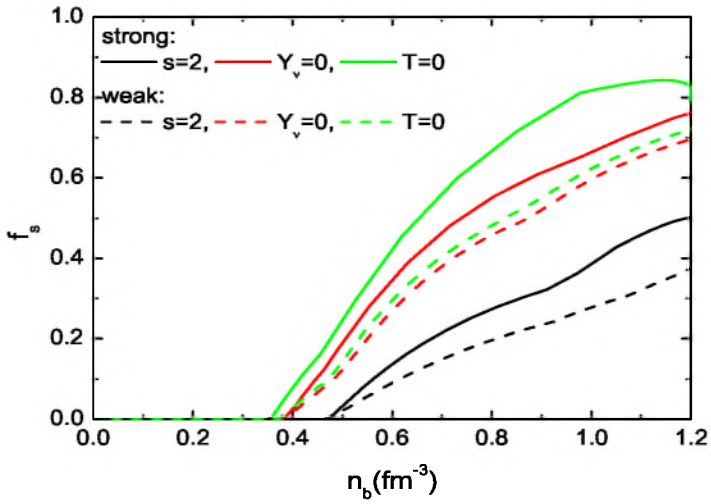

Figure 12.21: The parameter f_s as a function of the baryon number density n_b for each specified evolutionary phases. The hot models with trapped neutrinos are marked as $s = 2$, whereas hot, deleptonized models as $Y_\nu = 0$

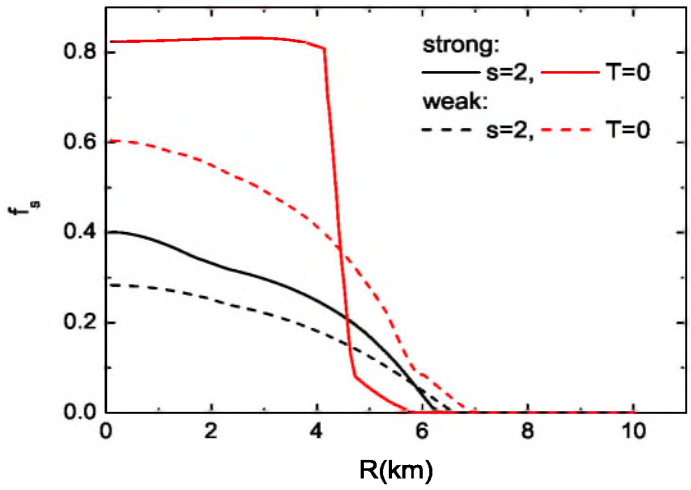

Figure 12.22: The parameter f_s as a function of the stellar radius for the weak and strong models are presented

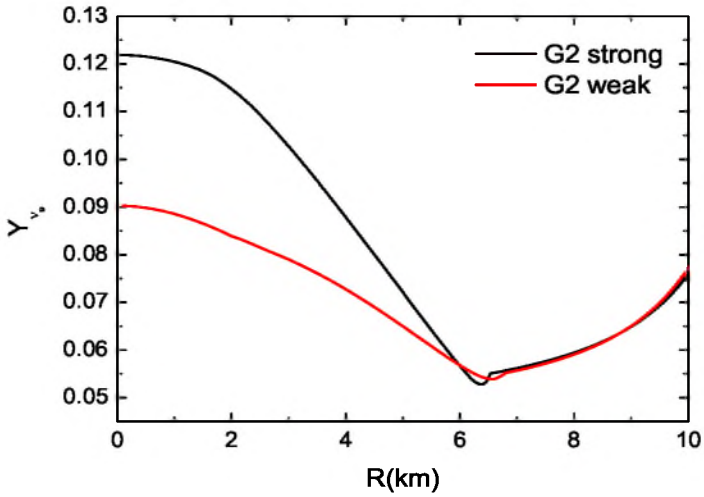

Figure 12.23: Neutrino concentrations as a function of stellar radius R for the maximum mass configuration for the G2 parameter set

Fig. 12.18 presents a new feature of the second stable configuration results (configuration B) namely almost completely lack of leptons in the innermost compact hyperon core. This core is surrounded by a lepton-rich layer. The relative hadron-lepton composition in this model can also be analyzed through the density dependence of the asymmetry parameter f_a which describes the neutron excess in the system and the parameter $f_s = (N_\Lambda + 2N_{\Xi^-} + 2N_{\Xi^0})/n_b$ which is connected with the strangeness contents. Fig.12.19 and 12.21 present both parameters as functions of baryon number density n_b whereas Fig.12.20 and 12.22 include the asymmetry of the maximum mass configuration and the the strangeness content as functions of the stellar radius R. As the density increases, the asymmetry of the matter decreases and the parameter f_s increases for all the considered cases. Deleptonization and cooling leads to stellar matter which is less asymmetric and possesses substantially enhanced strangeness content. The innermost stable core of the maximum mass configuration B contains almost symmetric strange nuclear matter with the reduced lepton content. Fig. 12.22 shows the strangeness content in the neutron star matter as a function of the stelar radius R. There is a substantially increased strangeness fraction in this core. This is mainly due to the enhanced concentration of Ξ^- and Ξ^0 hyperons. Fig. 12.23 contains the neutrino fraction Y_ν as a function of the stellar radius R. In the case of strong $Y - Y$ interaction neutrino concentration in the core of the proto-neutron star is much higher then the concentration obtained for the weak model. Fig. 12.23 presents neutrino concentrations as a function the stellar radius for the maximum mass configuration.

Chapter 13

Conclusions

Isospin asymmetric nuclear matter is of fundamental importance in understanding the structure of a neutron star whose formation is preceded by the phenomenon of supernova explosion and additionally by an intermediate stage known as a proto-neutron star. In this dissertation the properties of asymmetric nuclear matter have been studied in a systematic approach within the relativistic mean field model. Two parameter sets G2 and TM1* which stem from the effective field theory have been used to construct neutron star models. The results have been compared with those obtained with the use of the standard TM1 parameter set extended by additional nonlinear meson interaction terms and by the inclusion of the δ meson field. The performed analysis of isospin asymmetric nuclear matter has shown that the bulk properties of nuclear matter depend on the asymmetry parameter which determines the neutron excess in the nuclear systems. The systematic comparison of the properties of symmetric and asymmetric nuclear matter has been done. The asymmetric nuclear matter is less bound and less stiff at saturation than the symmetric one. There is also a strong dependence of the saturation density on the isospin asymmetry. The equilibrium density of the more asymmetric nuclear matter is shifted to lower densities. The model with the δ meson appears to give the stiffest equation of state, whereas inclusion of the ω-ρ and σ-ρ meson interaction terms results in softer equations of state. The softening of the equation of state due to the isospin asymmetry is of particular importance for the models of supernova explosion and for the proto-neutron and neutron star structures [200, 202]. Similar conclusions can be drawn considering the density dependence of the symmetry energy. The inclusion of δ meson increases the stiffness of the symmetry en-

ergy at high densities, whereas the nonlinear meson terms make the symmetry energy softer.

Neutron star properties are significantly affected by the presence of hyperons. Thus the influence of the strength of hyperon-nucleon and hyperon-hyperon interactions on the properties of the neutron star matter and on a neutron star structure has been studied. The models considered do not include Σ hyperons due to the remaining uncertainty of the form of their potential in the nuclear matter at saturation density. In the scalar sector the scalar coupling of the Λ and Ξ hyperons requires constraining in order to reproduce the estimated values of the potential felt by a single Λ and a single Ξ in the saturated nuclear matter. The coupling of hyperons to the strange meson σ^* has been limited by the estimated value of hyperon potential depths in hyperon matter. Recent experimental data indicate a much weaker strength of hyperon-hyperon interaction. The currently obtained value of the $U_\Lambda^{(\Lambda)}$ potential at the level of 5 MeV permits the existence of the additional parameter set which reproduces this weaker $\Lambda\Lambda$ interaction. The analysis has been done for different strength of the hyperon-hyperon interaction.

Very important properties of the strangeness-rich nuclear matter are connected with the fact that for the symmetric nuclear matter and nuclear matter with low isospin asymmetry in the case of strong hyperon-hyperon interaction the increasing value of the strangeness content leads to more bound system with the minimum shifted towards higher densities. Contrary to this situation the increasing value of the strangeness content in hyperon matter characterized by the weak hyperon-hyperon interaction gives shallower minima in the result.

The presence of hyperons in general leads to the softening of the equation of state. The behavior of the equation of state corresponds directly to the value of the maximum neutron star mass.

In order to analyze the structure of a proto-neutron and neutron star the complete form of the equations of state of strangeness rich proto-neutron and neutron star matter had to be obtained. In the case of a proto-neutron star the models considered based on the assumption that this star consists of two main parts: the core and the outer layer. The pressure in the outer envelope is determined by free nucleons, electrons and neutrinos in β equilibrium. The influence of the strength of hyperon-hyperon interactions on the properties of the proto-neutron star matter and through this on a proto-neutron star

structure during selected phases of its evolution has been studied. It has been shown that replacing the strong hyperon-hyperon interaction model by the weak one introduces large differences in the composition of the proto-neutron star matter both in the strange and non-strange sectors. There is a considerable reduction of the Λ hyperon concentration whereas the concentrations of Ξ^- and Ξ^0 hyperons are enhanced during the deleptonization. In addition, the population of Λ hyperons obtained in the weak models in the considered evolutionary stages is lower in comparison with those calculated for the strong hyperon-hyperon interaction models. Thus the weak models with the reduced Λ hyperon population permit larger fractions of protons and electrons and lead to lower concentrations of neutrinos. The G2 and TM1*-strong parameterizations lead to proto-neutron neutron stars with the reduced value of the maximum masses.

The composition of strangeness-rich cold neutron star matter and the threshold density for hyperons have been also altered when the strength of the hyperon-hyperon interaction is changed and when the nonlinear meson interactions are included.

The equations of state obtained for the strong hyperon-hyperon interaction for the G2 and TM1* parameterizations indicate the presence of two kinks. These kinks mark the existence of a phase of matter where hyperons, nucleons and leptons are in the thermodynamic equilibrium. This mixed phase is connected with the substantial softening of the equation of state. The second kink indicate the appearance of deeply bound, almost symmetric hyperon matter with significantly reduced lepton content. These properties of matter change the high-density behavior of the equation of state. The equation of state becomes stiffer. This very particular form of the equation of state generate different solutions of the Oppenheimer–Tolman–Volkoff equations. In the case of the cold neutron star model, apart from the ordinary neutron star branch, there exists an additional stable branch of solutions. They distinguish themselves by the values of masses similar to those of ordinary neutron stars yet with radii that are significantly reduced. These additional stable solutions may be interpreted in terms of the third family of stable compact stars. The value of masses of the two subsequent maxima on the mass-radius diagram depends on the potential depth $U_\Lambda^{(N)}$ in saturated nuclear matter. The analysis has been done for three values of the potential $U_\Lambda^{(N)}$: -27 MeV, -28 MeV and -30 MeV. The maximum mass of the ordinary neutron star sequence is

greater then the maximum mass of the very compact hyperon star for the minimal value of the potential $U_{\Lambda}^{(N)} = -27$ MeV. Higher values of this potential give in the result higher mass of the hyperon star. Stars of the first stable sequence are mainly composed of nucleons with a small admixture of Λ hyperons. Whereas stars of the second stable branch have developed very compact hyperon core with almost symmetric strangeness-rich nuclear matter and with the reduced lepton content. The comparison of the mass-radius diagrams obtained for different equations of state leads to the conclusion that the additional stable sequence on the mass-radius relation appear only in exceptional circumstances. The analysis of the stability of asymmetric strangeness-rich nuclear matter indicates that at sufficiently low asymmetry and high strangeness content deeply bound nuclear matter leads to the existence of additional stable compact stars bound not only by gravity but also by the interaction. The third family branches have been obtained for the G2 and TM1* parameterizations. These two models which have been constructed on the basis of the effective field theory include different nonlinear meson interaction terms which modify the behavior of the meson fields. Of special interest is the behavior of the scalar meson field which determines the effective baryon masses. The conditions under which the quark matter occurs in neutron star interiors thus permitting the formation of stable hybrid stars have been established in order to make the analysis more complete. Two phases of matter have been compared: the strange hadronic matter and quark matter. The phase with the highest pressure (lowest free energy) is favored. The performed analysis of the possible existence of the mixed quark-hadron phase inside a neutron star shows that due to remaining uncertainties about the parameters of the quark star model especially the bag constant the construction of the equation of state of the quark phase introduces some freedom in interpreting the results.

Bibliography

[1] F. Weber: *Pulsars as Astrophysical Laboratories for Nuclear and Particle Physics.* Philadelphia: IOP Publishing 1999.

[2] N. K. Glendenning: *Compact Stars, Nuclear Physics, Particle Physics and General Relativity.* New York: Sringer-Verlag 2000.

[3] H. Heiselberg: Phys. Rept., **328**, 237 (2000).

[4] H. Heiselberg: Ann. Rev. Nucl. Part. Sci., **50**, 481 (2000).

[5] J. M. Lattimer, M. Prakash: Astrophys. J., **550**, 426 (2001).

[6] D. Arnett: *Supernova and Nucleosynthesis.* Princeton: Princeton University Press 1996.

[7] D. D. Clayton: 1968, *Principles of Stellar Evolution and Nucleosythesis.* New York: McGraw-Hill Book Company 1968.

[8] G. S. Bisnovatyi-Kogan: *Stellar Physics.* New York: Sringer-Verlag 2001.

[9] S. L. Shapiro, S. A. Teukolsky: *Black Holes, White Dwarfs and Neutron Stars: The Physics of Compact Objects.* New York: John Wiley and Sons 1983.

[10] P. Haensel, A. Y. Potekhin, D. G. Yakovlev: *Neutron Stars 1. Equation of State and Structure.* New York: Springer-Verlag 2007.

[11] C. J. Pethick, D. G. Ravenhall: Annu. Rev. Nucl. Part. Phys., **45**, 429 (1995).

[12] I. E. Legaris, V. R. Pandharipande: Nucl. Phys., **A369**, 470 (1981).

[13] R. B. Wiringa, V. Fiks, A. Fabrocini: Phys. Rev., **C38**, 1010 (1988).

[14] W. Zuo, A. Lejeune, U. Lombardo, J. F. Mathiot: Nucl. Phys., **A706**, 418 (2002).

[15] W. Zuo, A. Lejeune, U. Lombardo, J. F. Mathiot: Eur. Phys. J., **A14**, 496 (2002).

[16] I. Bombaci, U. Lombardo: Phys. Rev., **C44**, 1892 (1991).

[17] H. Q. Song, Z. X. Wang, T. T. S. Kuo: Phys. Rev., **C46**, 1788 (1992).

[18] M. R. Anastasio, L. S. Celenza, W. S. Pong, C. M. Shakin: Phys. Rep., **100**, 327 (1983).

[19] B. ter Haar, R. Malfliet: Phys. Rep., **149**, 207 (1987).

[20] R. Machleidt: Adv. Nucl. Phys., **19**, 189 (1989).

[21] G. Q. Li, R. Machleidt, R. Brockmann: Phys. Rev., **45**, 2782, (1992).

[22] M. Farine, J. M. Person, B. Rouben: Nucl. Phys., **A304**, 317 (1978).

[23] J. M. Pearson, Y. Aboussir, A. K. Dutta, R. C. Nayak, M. Farine, F. Tondeur: Nucl. Phys. **A528**, 1 (1991).

[24] B. D. Serot, J. D. Walecka: Adv. Nucl. Phys., **16**, 1 (1986).

[25] B. D. Serot, J. D. Walecka: Int. J. Mod. Phys., **E6**, 515 (1997).

[26] A. R. Bodmer: Nucl. Phys., **A526**, 703 (1991).

[27] L. S. Celenza, C. M. Shakin: *Relativistic Nuclear Physics: Theories of Structure and Scattering.* Singapore: World Scientific 1986.

[28] P. G. Reinhard, M. Rufa, J. Maruhn, W. Greiner, J. Friedrich: Z. Phys., **A323**, 13 (1986).

[29] P. G. Reinhard: Rep. Prog. Phys. **52**, 439 (1989).

[30] B. D. Serot: Prog. Phys., **55**, 1855 (1992).

[31] K. Sumiyoshi, H. Toki: Astrophys. J., **422**, 700 (1994).

[32] J. Boguta, A. R. Bodmer: Nucl. Phys., **A292**, 413 (1977).

[33] J. Boguta, A. R. Bodmer: Int. J. Mod. Phys., **E6**, 515 (1977).

[34] A. R. Bodmer, C. E. Price: Nucl. Phys., **A505**, 123 (1989).

[35] S. J. Gmuca: J. Phys., **G17**, 1115 (1991).

[36] R. J. Furnstahl, B. D. Serot, H. B. Tang: Nucl. Phys., **A598**, 539 (1996).

[37] R. J. Furnstahl, B. D. Serot, H. B. Tang: Nucl. Phys., **A615**, 441 (1997).

[38] H. Georgi, A. Manohar: Nucl. Phys., **B234**, 189 (1984).

[39] H. Georgi: Phys. Lett., **B298**, 187 (1993).

[40] B. D. Serot: Lect. Note Phys., **641**, 31 (2004).

[41] G. A. Lalazissis, J. König, P. Ring: Phys. Rev., **C55**, 540 (1997).

[42] C. J. Horowitz, B. D. Serot: Phys. Lett., **B137**, 283 (1984).

[43] A. Amorin, J. A. Tjon: Phys. Rev. Lett., **68**, 772 (1992).

[44] T. Sil, S. K. Patra, B. K. Sharma, M. Centelles, X. Vinas: Contribution to *Focus on Quantum Field Theory.* New York: Nova Science Publishers 2005.

[45] M. Del Estal: Nucl. Phys., **A650**, 443 (1990).

[46] C. J. Horowitz, J. Piekarewicz: Phys. Rev., **C63**, 011303 (2001).

[47] I. Bednarek, R. Manka: Int. J. Mod. Phys., **D10**, 607 (2001).

[48] G. Baym, H. Bethe, C. J. Pethick: Astrophys. J., **175**, 225 (1991).

[49] R. Machleidt, K. Holinde, Ch. Elster: Phys. Rept., **149**, 1 (1987).

[50] J.W. Negele, D. Vautherin: Nucl. Phys., **A207**, 298 (1973).

[51] A. W. Steiner, M. Prakash, J. M. Lattimer, P. J. Ellis: Phys. Rept., **411**, 325 (2005).

[52] M. Schwarzschild: *Structure and Evolution of the Stars.* Princeton: Princeton University Press 1958.

[53] I. Iben: Astrophys. J. Suppl., **76**, 55 (1991).

[54] G. Imbriani, M. Limongi, L. Gialanella, F. Terrasi, O. Straniero, A. Chieffi: Astrophys. J., **558**, 903 (2001).

[55] O. Straniero, I. Dominguez, G. Imbriani, L. Piersanti: Astrophys. J., **583**, 878 (2003).

[56] R. Kunz, M. Fey, M. Jaeger, A. Mayer, J. W. Hammer: Astrophys. J., **567**, 643 (2002).

[57] R. C. Tolman: 1939, Phys. Rev., **55**, 364 (1939).

[58] J. R. Oppenheimer, G. M. Volkoff: Phys. Rev., **55**, 374 (1939).

[59] L. D. Landau, E. M. Lifshitz: *Statistical Physics.* New York: Addison-Wesley 1969.

[60] S. Chandrasekhar: *An Introduction to the study of Stellar Structure.* Chicago: University of Chicago Press 1939.

[61] S. Bludman, K. A. van Riper: Astrophys. J. **212**, 859 (1977).

[62] M. Fukugita, H. Suzuki: *Physics and Astrophysics of Neutrinos.* New York: Springer-Verlag 1994.

[63] P. Goldreich, S.V. Weber: Astrophys. J., **238**, 991 (1980).

[64] A. Yahil, J. M. Lattimer: in *Supernovae: A Survey of Current Research.* edited by M. J. Rees, R. J. Stoneham, D. Reidel, Dordrecht: Publishing Company: 1982.

[65] A. Yahil: Astrophys. J., **265**, 1047 (1983).

[66] P. Haensel, J. L. Zdunik: Astron. Astrophys., **227**, 431 (1990).

[67] P. Haensel, J. L. Zdunik: Astron. Astrophys., **404**, L33 (2003).

[68] F. Douchin, P. Haensel: Phys. Lett., **B485**, 107 (2000).

[69] G. Baym, H. A. Bethe, C. J. Pethick: Nucl. Phys., **A175**, 225 (1971).

[70] P. Haensel: Neutron star crust. in *Physics of Neutron Star Interiors.* Berlin-New York: edited by D. Blaschke, N. K. Glendenning, A. Sedrakin, Springer – Lecture Notes in Physics 2001.

[71] V. R. Pandharipande, D. G. Ravenhall: Proc. NATO Advanced Research Workshop on Nuclear Matter and Heavy Ion Collisions. Les Houches: edited by M. Soyeuret et al. 1989.

[72] C. P. Lorenz, D. G. Ravenhall, C. J. Pethick: Phys. Rev. Lett., **70**, 379 (1993).

[73] W. D. Meyers, W. J. Swiatecki: Ann. Phys., **55**, 395 (1969).

[74] M. Prakash, T. L. Ainsworth, J. M. Lattimer: Phys. Rev. Lett., **61**, 2518 (1988).

[75] K. C. Chung, C. S. Wang, A. J. Santiago, J. W. Zhang: Phys. Rev., **C61**, 047303 (2000).

[76] J. M. Lattimer, C. J. Pethick, M. Prakash, P. Haensel: Phys. Rev. Lett., **66**, 2701 (1991).

[77] P. J. Siemens: Nucl. Phys., **A141**, 225 (1970).

[78] V. Thorson, M. Prakash, J. M. Lattimer: Nucl. Phys., **A572**, 693 (1994).

[79] H. Huber, F. Weber, M. K. Weigel: Phys. Lett., **B317**, 485 (1993).

[80] J. P. Blaizot: Phys. Rep., **64**, 171 (1980).

[81] H. M. Müller, B. D. Serot: Nucl. Phys., **A606**, 508 (1996).

[82] D. H. Youngblood, C. M. Rozsa, J. M. Moss, D. R. Brown, J. D. Bronson: Phys. Rev. Lett., **39**, 1188 (1977).

[83] D. H. Youngblood, P. Bogucki, J. D. Bronson, U. Garg, Y. W. Lui, C. M. Rozsa: Phys. Rev., **C23**, 1997 (1981).

[84] D. H. Youngblood, H. L. Clark, Y. W. Lui: Nucl. Phys., **A649**, 49c (1999).

[85] G. Colo, N. Van Giai, J. Meyer, K. Bennaceur, P. Bonche: Phys. Rev. **C70**, 024307 (2004).

[86] D. H. Youngblood, H. L. Clark, Y. W. Lui: Pys. Rev. Lett., **82**, 691 (1999).

[87] B. K. Agrawal, S. Shlomo, V. Kim Au: Phys. Rev., **C68**, 031304 (2003).

[88] J. P. Blaizot, J. F. Berger, J. Dechage, M. Girod: Nucl. Phys., **A591**, 435 (1995).

[89] D. Vretenar, A. Wandelt, P. Ring: Phys. Lett., **B487**, 334 (2000).

[90] J. Piekarewicz: Phys. Rev., **C66**, 034305 (2002).

[91] E. D. Baron, J. Cooperstein, S Kahana: Phys. Rev. Lett., **55**, 12 (1985).

[92] Dao T. Khoa, W. Von Oertzen, A. A. Ogloblin: Nucl. Phys., **A602**, 98 (1996).

[93] K. Kolehmainen, M. Prakash, J. Lattimer, J. Treiner: Nucl. Phys., **A439**, 535 (1985).

[94] R. Brockmann, R. Machleidt: Phys. Rev., **C42**, 1965 (1990).

[95] P.E. Haustein: at *Data Nucl. Data Tables*, **88**, 185 1988.

[96] B. L. Friman, O. V. Maxwell: Astrophys. J., **232**, 541 (1979).

[97] M. Prakash: Phys. Rep., **242**, 191 (1994).

[98] A. Akmal, V. R. Pandharipande, D. G. Ravenhall: Phys. Rev. **C58**, 1804 (1998).

[99] S. A. Chin: Ann. Phys., **108**, 301 (1977).

[100] Y. Sugahara, H. Toki: Nucl. Phys., **A579**, 557 (1994).

[101] R. Manka, I. Bednarek, G. Przybyla: Phys. Rev., **C62**, 105802 (2000).

[102] P. G. Reinhard: Z. Phys., **A329**, 257 (1988).

[103] M. Rufa, P. G. Reinhard, J. Maruhn, W. Greiner, M. R. Strayer: Phys. Rev., **C38**, 390 (1988).

[104] M. M. Sharma, M. A. Nagarajan, P. Ring: Phys. Lett., **B312**, 377 (1993).

[105] L. Engvik, M. Hjorth-Jensen, R. Machleidt, H. Müther, A. Polls: Nucl.Phys., **A627**, 85 (1997).

[106] R. B. Wiringa, R. A. Smith, T. L. Ainsworth: Phys. Rev., **C29**, 1207 (1984).

[107] R. V. Reid: Ann. Phys., **50**, 411 (1968).

[108] M. Lacombe et al.: Phys. Rev., **C21**, 861 (1980).

[109] R. Machleidt, F. Sammaruca, Y. Song: Phys. Rev., **C53**, R1483 (1996).

[110] R. B. Wiringa, V.G. J. Stoks, R. Schiavilla, Phys. Rev., **C51**, 38 (1995).

[111] V.G. J. Stoks, R. A. M Klomp, C. P. F. Terheggen, J. J. de Swart: Phys. Rev., **C49**, 2950 (1994).

[112] J. D. Walecka: *Theoretical Nuclear and Subnuclear Physics.* Singapore: World Scientific, Singapore 2004.

[113] S. Gmuca: Z. Phys., **A342**, 387 (1992); Nucl. Phys., **A547**, 447 (1992).

[114] P. Haensel, B. Pichon: Astron. Astrophys., **283**, 313 (1994).

[115] C.J. Horowitz, J. Piekarewicz: Phys. Rev., **C64**, 064616 (2001).

[116] C.J. Horowitz, J. Piekarewicz: Phys. Rev. Lett., **86**, 5647 (2001).

[117] R. Manka, I. Bednarek: J. Phys., **G27** (2001).

[118] S. Kubis, M. Kutschera: Phys. Lett., **B399**, 191 (1997).

[119] I. Bednarek, M. Kęska, R. Manka: Int. J. Mod. Phys., **D12**, 1 (2003).

[120] S. Kubis, M. Kutschera, S. Stachniewicz: Acta Phys. Polon., **B29**, 809 (1998).

[121] I. Bednarek, R. Manka: Physica Scripta, **61**, 544 (2000).

[122] D. J. Millner, A. Gal, C. B. Dover, R. H. Dalitz: Phys. Rev., **C31**, 499 (1985).

[123] A. Bouyssy: Nucl. Phys., **A290**, 159 (1977).

[124] R. Brockmann, W. Weise: Nucl. Phys., **A355**, 364 (1981).

[125] J. Boguta, S. Bohrmann: Phys. Lett., **B102**, 93 (1981).

[126] M. Rufa, H. Stöcker, P. G. Reinhard, J. Maruhn, W. Greiner: J. Phys., **G13**, L143 (1987).

[127] J. Mareŝ, J. Žofka: Z. Phys., **A333**, 209 (1989).

[128] M. Rufa, J. Schaffner, J. Maruhn, H. Stöcker, W. Greiner, P. G. Reinhard: Phys. Rev., **C42**, 2469 (1990).

[129] C. Greiner, J. Schaffner-Bielich: in *Heavy Elements and Related new Phenomena.*, edited by R. K. Gupta, W. Greiner, World Scientific Publications 1998.

[130] C. J. Batty, E. Friedman, A. Gal, B. K. Jennings: Phys. Lett., **335**, 273 (1994).

[131] C. J. Batty, E. Friedman, A. Gal, B. K. Jennings: Prog. Theor. Phys. Suppl., **117**, 145 (1994).

[132] S. Balberg, A. Gal., J. Schaffner: Prog. Theor. Phys. Suppl., **117**, 325 (1994).

[133] V. G. J. Stoks, T. S. H. Lee: Phys. Rev., **C60**, 024006 (1999).

[134] J. Schaffner, C. B. Dover, A. Gal, C. Greiner, D. J. Millner, H. Stocker: Ann. Phys., **235**, 35 (1994).

[135] Takahashi et al.: Phys. Rev. Let., **87**, 212502 (2001).

[136] R. H. Dalitz, D. H. Davis, P. H. Fowler, A. Motwill, J. Pniewski, J. A. Zakrzewski: Proc. R. Soc. London, **A426**, 1 (1989).

[137] S. Aoki S. et al.: Prog. Theor. Phys., **85**, 1287 (1991).

[138] M. Danysz et al.: Nucl. Phys., **49**, 121 (1963).

[139] D. J. Prowse: Phys. Rev. Lett., **17**, 782 (1966); S. Schramm, H. Stcker, W. Greiner: Astrophys. J., **573**, 958 (2000).

[140] J. Schaffner-Bielich, A. Gal: Phys. Rev., **C62**, 034311 (1999).

[141] I. Bednarek, R. Manka: J. Phys., **G31**, 1009 (2005).

[142] B. C. Clark, R. J. Furnstahl, L. K. Kerr, J. Rusnak, S. Hama: Phys. Lett., **B427** (1988).

[143] M. Del Estal, M. Centelles, X. Viñas: Nucl. Phys., **A650**, 443 (1999).

[144] P. Wang: Phys. Rev., **C61**, 054904 (2000).

[145] I. Bednarek, R. Manka: Phys. Rev., **C73**, 045804 (2006).

[146] T. Gross-Boelting, C. Fuchs, A. Faessler: Nucl. Phys., **A648**, 207 (1999).

[147] B. Liu, H. Guo, M. Di Toro, V. Greco: Eur. Phys. J., **A25**, 293 (2005).

[148] C. Greiner, J. Schaffner: Int. J. Mod. Phys., **E5**, 239 (1996).

[149] H. Müller: Phys. Rev., **C59**, 1405 (1999).

[150] H. Huber, F. Weber, M. K. Weigel, Ch. Schaab: Int. J. Mod. Phys., **E7**, 301 (1998).

[151] M. Prakash, I. Bombaci, M. Prakash, P. J. Ellis, J. M. Lattimer, R. Knorren: Pyhs. Rep., **280**, 1 (1997).

[152] T. Klähn et al.: Phys. Rev., **C74**, 035802 (2006).

[153] C. J. Horowitz, J. Piekarewicz: Phys. Rev. **C66**, 055803 (2002).

[154] C. J. Pethick: Rev. Mod. Phys. **64**, 1133 (1992).

[155] P. Slane, D. J. Helfand, S. S. Murray: astro-ph/0204151 (2002).

[156] G. G. Pavlov, O. Y. Kargaltsev, D. Sanwal, G. P. Garmire: Astrophys. J. **554**, L189 (2001).

[157] J. P. Halpern, F. Y. H. Wang: Astrophys. J. **477**, 905 (1997).

[158] R. Wijnands, M. Guainazzi, M. van der Kils, M. Mendez: Astrophys. J. **573**, L45 (2002).

[159] M. Colpi, U. Geppert, D. Page, A. Possenti: Astrophys. J. **L175** (2001).

[160] B. Friedman, V. R. Pandharipande: Nucl. Phys. **A361**, 502 (1981).

[161] R. Manka, I. Bednarek, S. Przybyla: New J. Phys. **4**, 14 (2002).

[162] C. E. Rhoades, R. Ruffini: Phys. Rev. Lett.**32**, 324 (1974).

[163] H. A. Buchdahl: Phys. Rev., **116**, 1027 (1966).

[164] H. A. Buchdahl: Astrophys. J., **146**, 303 (1966).

[165] T. E. Strohmayer, C. B. Markwardt: Astrophys. J. **577**, 337 (2002).

[166] M. C. Miller: in Proceedings of the NATO Advanced Workshop *Superdence QCD Matter and Compact Stars*, Yerevan: edited by D. Blaschke 2003.

[167] J. Lattimer, M. Prakash, 2004, *Science*, **304**, 536

[168] D. J. Nice, E. M. Splaver, I. H. Stairs, O. Löhmer, A. Jessner, M. Kramer, J. M. Cordes: Astrophys. J., **634**, 1242 (2005).

[169] P. A. Charles, M. J. Coe: in Compact Stellar X-ray Sources. edited by W. H. G. Lewin, M. van der Klis, Cambridge: Cambridge University Press 2005.

[170] J. Frank, A. R. King, D. J. Raine: *Accretion Power in Astrophysics.* Cambridge: Cambridge University Press 2002.

[171] H. A. Bethe, G. E. Brown: Astrophys. J., **445**, L129 (1995).

[172] O. Barziv, L. Kaper, M. H. van Kerwijk, J. H. Telting, J. van Paradijs: Astron. Astrophys. **377**, 925 (2001).

[173] H. Quaintrell et al.: Astron. Astrophys., **401**, 313 (2003).

[174] J. A. Orosz, E. Kuulkers: Mon. Not. Roy. Ast. Soc., **305**, 132 (1999).

[175] M. C. Miller, F. K. Lamb: Astrophys. J., **499**, L37 (1998).

[176] J. Cottam, F. Paerels, M. Méndez: Nature, **420**, 51 (2002).

[177] F. Özel, D. Psaltis: Astrophys. J., **582**, L31 (2003).

[178] S. Bhattacharyya, T. E. Strohmayer, M. C. Miller, C. B. Markwardt: Astrophys. J., **619**, 483 (2005).

[179] M. P. Muno, F. Özel, D. Chakrabarty: Astrophys. J., **581**, 550 (2002).

[180] S. E. Thorsett, D. Chakrabarty: Astrophys. J., **512**, 288 (1999).

[181] D. J. Nice, E. M. Splaver, I. H. Stairs: in *Radio Pulsars*, edited by M. Bailes, D. J. Nice, S. E. Thorestt, *Astron. Soc. Pac. Conf. Ser 303*, San Francisco 2003.

[182] D. J. Nice, E. M. Splaver, I. H. Stairs: *IAU Symp. 218, ASP Conference Proceedings*, edited by F. Camillo, B. M. Gaensler 2003.

[183] D. Psaltis, F. Özel, S. DeDeo: Astrophys. J., **544**, 390 (2000).

[184] S. van Straten, E. C. van der Klis, M. Méndez, P. Kaaret: Astrophys. J., **540**, 1049 (2000).

[185] X. D. Li, I. Bombaci, M. Dey, J. Dey, E. P. J. van den Heuvel: Phys. Rev. Lett., **83**, 3776 (1999).

[186] M. Prakash, J. M. Lattimer, J. A. Pons, A. W. Steiner: Lect. Notes Phys., **578**, 364 (2001).

[187] M. Prakash, J. M. Lattimer, R. F. Sawyer, R. R. Volkas: Ann. Rev. Nucl. Part. Sci., **51**, 295 (2001).

[188] S. Reddy, M. Prakash, J. M. Lattimer: Phys. Rev., **D58**, 013009 (1998).

[189] M. Th. Keil: astro-ph 0308228 (2003).

[190] H.-Th. Janka: Astropart. Phys., **3**, 377 (1995).

[191] H. T. Janka, G. G. Raffelt: Phys. Rev., **D59**, 023005 (1999).

[192] H. T. Janka, K. Kifonnidis, M. Rampp: Lect. Notes Phys., **578**, 333 (2001).

[193] S. Banik, D. Bandyopadhyay: Phys. Rev., **C64**, 055805 (2001).

[194] N. K. Glendenning, C. Kettner: Astron. Astrophys., **353**, L9 (2000).

[195] I. N. Mishustin, M. Hanauske, A. Bhattacharyya, L. M. Satarov, H. Stöcker, W. Greiner: Phys. Lett. **B552**, 1 (2002).

[196] P. Haensel, J. L. Zdunik, R. Schaeffer: Astron. Astrophys., **217**, 137 (1989).

[197] Y. Sugahara, H. Toki: Prog. Theor. Phys., **92**, 803 (1994).

[198] J. Schaffner, I. N. Mishustin: Phys. Rev., **C53**, 1416 (1996).

[199] N. K. Glendenning, S. A. Moszkowski: Phys. Rev. Lett., **67**, 2414 (1991).

[200] F. Weber: *Nuclear and high-energy astrophysics* in Proceedings of the VIII International Workshop on Hadron Physics, Brazil 2002.

[201] E. M. Butterworth, J. R. Ipser: Astrophys. J., **204**, 200 (1976).

[202] P. Haensel, J. L. Zdunik: Nature, **340**, 617 (1989).

Ilona Bednarek

Modele gwiazd neutronowych w ujęciu relatywistycznej teorii pola średniego

Streszczenie

Celem pracy było zbadanie własności asymetrycznej materii jądrowej, ze szczególnym uwzględnieniem obszaru wysokich gęstości charakterystycznych dla rdzeni gwiazd neutronowych. Przeprowadzona analiza obejmowała nieliniowe modele Walecki, z dodatkowymi członami nieliniowymi uwzględniającymi oddziaływanie mezonu skalarnego σ i mezonu wektorowego ρ oraz mezonów wektorowych ω i ρ, jak również modele skonstruowane na podstawie efektywnej teorii pola – model Furnstahla, Serota i Tanga (FST). Obliczenia zostały wykonane w przybliżeniu relatywistycznej teorii pola średniego. Dodatkowe rozszerzenie sektora izoskalarnego obejmowało wprowadzenie mezonu izowektorowego δ. W obszarze bardzo wysokich gęstości energie Fermiego neutronów przyjmują tak duże wartości, że korzystna energetycznie staje się ich konwersja na hiperony. Uwzględnienie dziwności w rozpatrywanych modelach materii jądrowej pozwoliło na szerszą analizę dodatkowych klas modeli, w których został zbadany wpływ oddziaływania nukleon–hiperon i hiperon–hiperon na postać równania stanu materii gwiazdy neutronowej.

Równanie stanu jest najważniejszym czynnikiem decydującym zarówno o strukturze, jak i o parametrach gwiazdy neutronowej.

Szczególnie interesujące są wartości mas maksymalnych obliczone dla poszczególnych modeli. W przypadku modeli uzyskanych na gruncie efektywnej teorii pola i następnie rozszerzonych przez uwzględnienie niezerowej dziwności rozwiązania równania Oppenheimera–Volkoffa–Tolmana wskazują na istnienie trzeciej rodziny stabilnych, zwartych gwiazd o gęstościach przekraczających gęstości występujące w rdzeniach gwiazd neutronowych.

Ilona Bednarek

Relativistische Mittelfeld-Modelle von Neutronensterne

Zusammenfassung

Ziel der Arbeit war, die assymetrische Eigenschaft der Kernmaterie unter besonderer Berücksichtigung des Bereichs hoher Dichten, die für Kerne der Neutronensternen charakteristisch sind, zu erforschen. Die durchgeführte Analyse umfasste nicht lineare Walecki-Modelle mit zusätzlichen, nicht linearen Segmenten, welche die Wechselwirkung des Skala-Mesons σ und des Vektor-Mesons ρ, der Vektor-Mesonen ω und ρ, sowie Modelle, die in Anlehnung und die effektive Feldtheorie – das Modell von Furnstahl, Serot und Tang (FST) konstruiert wurden, berücksichtigen. Die Berechnungen wurden in Annäherung an die relativistische Mittelfeldtheorie durchgeführt. Zusätzliche Erweiterung des isoskalaren Sektors umfasste die Einführung des Isovektores δ. Im Bereich sehr hoher Dichten nehmen die Fermie – Energieen von Neutronen so grosse Werte ein, dass energetisch günstig ihre konversion in Hyperonen wird. Die Berücksichtigung der Strangeness in den untersuchten Modellen der Kernmaterie liess eine breitere Analyse zusätzlicher Modellklassen vornehmen, bei denen der Einfluss der Wechselwirkungen Nukleon – Hyperon und Hyperon – Hyperon auf die Form der Zustandsgleichung der Materie eines Neutronensternes untersucht wurde. Die Zustandsgleichung der Materie eines Neutronensternes untersucht wurde.

Die Zustandsgleichung ist der wichtigste Faktor, der sowohl über die Parameter eines Neutronensternes entscheidet.

Besonders interessant sind die maximalen Massenwerte für die einzelne Modelle berechnet. Im Fall von Modellen, die aufgrund der Effektiven Feldtheorie erreicht und anschliessend durch Berücksichtigung der Nichtnull – Strangeness erweitert wurden deutet die Lösung der Oppenheimer – Volkoff – Tolman Gleichung auf die Existenz einer dritten Familie stabiler, einheitlichen Sterne hin, deren Dichten die in den Kernen von Neutronensternen auftretenden Dichten beschreiten.